INTEGRATED COMPUTATIONAL AND EXPERIMENTAL APPROACH TO CONTROL PHYSICAL TEXTURE DURING LASER MACHINING OF STRUCTURAL CERAMICS

Hitesh D. Vora

Dissertation Prepared for the Degree of

DOCTOR OF PHILOSOPHY

UNIVERSITY OF NORTH TEXAS

December 2013

APPROVED:

Narendra B. Dahotre, Major Professor and
Chair of the Department of Materials
Science and Engineering
Jincheng Du, Committee Member
Rajarshi Banerjee, Committee Member
Zhenhai Xia, Committee Member
Sundeep Mukherjee, Committee Member
Costas Tsatsoulis, Dean of the College of
Engineering
Mark Wardell, Dean of the Toulouse Graduate
School

Vora, Hitesh D. *Integrated Computational and Experimental Approach to Control Physical Texture during Laser Machining of Structural Ceramics*. Doctor of Philosophy (Materials Science and Engineering), December 2013, 99 pp., 10 tables, 49 figures, references, 61 titles.

The high energy lasers are emerging as an innovative material processing tool to effectively fabricate complex shapes on the hard and brittle structural ceramics, which previously had been near impossible to be machined effectively using various conventional machining techniques. In addition, the in-situ measurement of the thermo-physical properties in the severe laser machining conditions (high temperature, short time duration, and small interaction volume) is an extremely difficult task. As a consequence, it is extremely challenging to investigate the evolution of surface topography through experimental analyses. To address this issue, an integrated experimental and computational (multistep and multiphysics based finite-element modeling) approach was employed to understand the influence of laser processing parameters to effectively control the various thermo-physical effects (recoil pressure, Marangoni convection, and surface tension) during transient physical processes (melting, vaporization) for controlled surface topography (surface finish). The results indicated that the material lost due to evaporation causes an increase in crater depth of machined cavity, whereas liquid expulsion created by the recoil pressure increases the material pileup height around the lip of machined cavity, the major attributes of surface topography (roughness). Also, it was found that the surface roughness increased with increase in laser energy density and pulse rate (from 10 to 50Hz), and with the decrease in distance between two pulses (from 0.6 to 0.1mm) or the increase in lateral and transverse overlap (0, 17, 33, 50, 67, and 83%). The results of the computational model are also validated by experimental observations with reasonably close agreement.

ACKNOWLEDGEMENT

This dissertation could not have been written without the true mentorship of Prof. Narendra B. Dahotre. His dedication, determination, disciplines, and desire towards fundamental scientific research is truly remarkable and always is my source of inspiration throughout my life. I am truly thankful to Prof. Dahotre for providing me this valuable learning opportunity and financial support during my doctoral degree. Secondly, I would like to express gratitude to my professors and committee members Dr. Jincheng Du, Dr. Rajarshi Banerjee, Dr. Zhenhai Xia, and Dr. Sundeep Mukherjee for their assistance in completing this dissertation. I would like to acknowledge the financial support from the National Science Foundation (NSF-CMMI 1010494) and the Department of Materials Science and Engineering at the University of North Texas (UNT) in various stages of my doctoral program. I would like to acknowledge Center for Advanced Research Technology (CART) at UNT and Prof. Radovan Kovacevic at Southern Methodist University for providing the research and characterization facilities. It is a pleasure for me to thanks Dr. S. G. Srivilliputhur, Dr. Sandra K. S. Boetcher, and Dr. Sandip Harimkar for being there for me throughout my PhD. I would also like to thank all of my lab mates, especially Ravi Shanker Rajamure and Yee-Hsien Ho (Thomas); and Dr. S. Soundarapandian for their help and support. The assistance of Bobby Grimes, Craig R. Collins, and David C. Garrett in setting up the laser material processing and synthesis lab (E-139) has been invaluable. Last but not least, I would like to give special thanks to my wife Komal for her support, patience, and unwavering love were definitely the backbone of my doctoral degree. I acknowledge my parents and elder brother (Ashwin) for their faith in me and allowing me to be as ambitious as I wanted. Last of all, I would like to dedicate this dissertation to my wonderful daughter Harini and wife Komal for being there for me in my ups-n-downs throughout the doctorate program.

TABLE OF CONTENTS

Page

LIST OF TABLES

Page

LIST OF FIGURES

Page

LIST OF ABBREVIATIONS

Al_2O_3	Alumina or aluminum oxide
ZrO_2	Zirconia or zirconium oxide
MgO	Magnesia or magnesium oxide
SiC	Silicon carbide
Si_3N_4	Silicon nitride
Nd:YAG	Neodymium-doped yttrium aluminum garnet
ρ	Density (kg/m^3)
C_p	Specific heat at constant pressure (J/kg.K)
k	Thermal conductivity (W/m.K)
T	Temperature (K)
t	Time (s)
x	x-coordinate (m)
y	y-coordinate (m)
z	y-coordinate (m)
C_p1	Modified specific heat at constant pressure (J/kg.K)
δ_m	Normalization function around the melting temperature (K^{-1})
δ_v	Normalization function around the vaporization temperature (K^{-1})
H’	Smooth heaviside function
L_m	Latent heat of melting (J/g)
T_m	Melting temperature (K)
ΔT	Half-width of the curve (K)

L_v	Latent heat of evaporation (J/g)
T_v	Vaporization temperature (K)
B	Fraction of a particular phase (solid, liquid or vapor)
T_x	Transition temperature between two distinct phases, solid-liquid or vapor-liquid (K)
φ	Laser on/off function
P_g	Average laser power density (W/m^2)
h	Heat transfer coefficient ($W/m^2.K$)
T_0	Ambient temperature (K)
T_i	Initial temperature (K)
ε	Emissivity
σ	Stefan-Boltzmann constant ($W/m^2.K^4$)
A	Absorptivity of laser beam
E_p	Energy per pulse (J)
P_w	Pulse width (s)
D	Diameter of laser beam (m)
x_r	Reference point to represents the center of the laser beam in the geometry along x-axis (m)
ϕ	Standard deviation of the Gaussian laser beam (m)
u	Velocity in the x-direction (m/s)
v	Velocity in the y-direction (m/s)
p	Pressure (N/m^2)
g	Gravitational constant (m/s^2)
α	Thermal expansion coefficient (K^{-1})

P_r	Recoil pressure (N/m^2)
T_s	Instantaneous surface temperature (K)
M_v	Mass of vapor molecule (kg/atm)
γ	Surface tension (N/m.K)
μ	Dynamic viscosity (Pa.s)
R	Universal gas constant (J/mol.K)
SiO_2	Silicon dioxide
Fe_2O_3	Iron oxide
R_2O	Base or fluxing oxides
R_p	Maximum peak height of the line profile (μm)
R_v	Maximum valley depth of the line profile (μm)
R_t	Maximum height of the line profile (μm) = $R_p + R_v$
Sp	Highest peak height of the surface profile (μm)
Sv	Highest valley depth of the surface profile (μm)
Sz	Maximum height of the surface profile (μm) = Sp+Sv
Dist	Distance between two laser pulses or lateral overlap
O_T	Transverse overlap

CHAPTER 1

MACHINING OF STRUCTURAL CERAMICS[1]

1.1 Unique Properties of Structural Ceramics

Structural materials are the materials generally used to build the structural components, which are specifically designed and developed to resist deformation under the applied load. Based on the requirements, the structural materials can be categorized into metal, polymer, ceramic, or combination of these materials. The classifications of structural materials with their special characteristics are summarized in the Figure 1.1 [1-5].

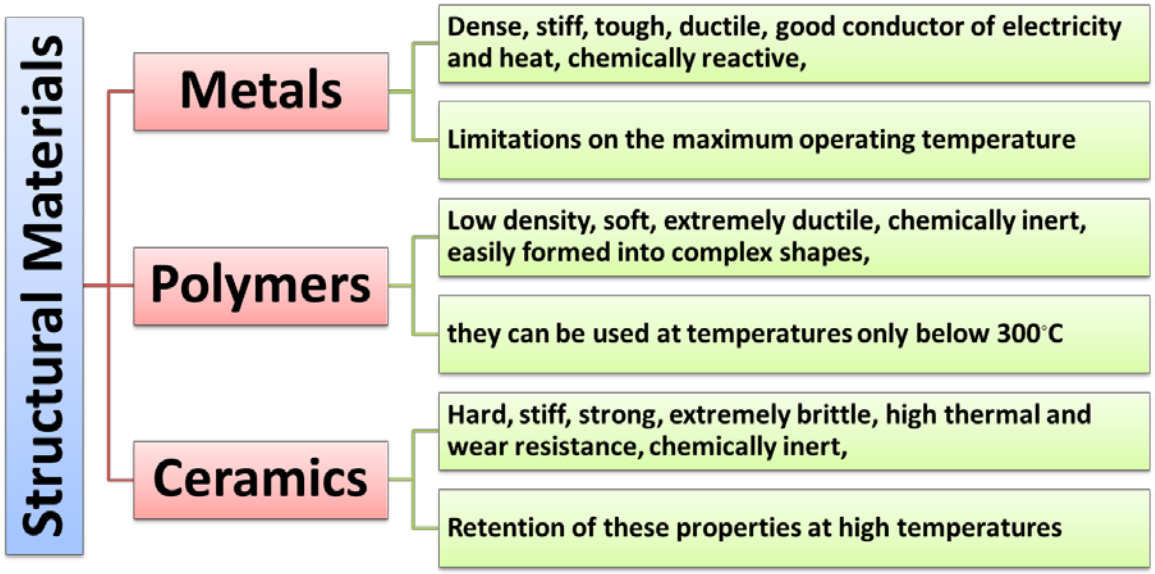

Figure 1.1 Classifications of structural materials

Based on the above classification and their distinctive physical and mechanical properties, these structural materials are have specific merits and demerits and therefore cannot be solely serve entire engineering field. Among all structural materials, the majority (>50%) of

[1] Parts of this chapter have been previously published, either in part or in full, from (1) Hitesh D. Vora, Soundarapandian Santhanakrishnan, Sandip P. Harimkar, Sandra K.S. Boetcher, Narendra B. Dahotre, *Journal of European Ceramic Society* 2012, 32 (16), 4205–4218 with permission from Elsevier, and (2) Hitesh D. Vora, Soundarapandian Santhanakrishnan, Sandip P. Harimkar, Sandra K.S. Boetcher, Narendra B. Dahotre, *International Journal of Advanced Manufacturing Technology* 2013, 68(1), 69-83 with permission from Springer

structural components are made out from metals, while, steel (iron alloys) and aluminum (and its alloys) are the two most commonly used structural metals. The main reason for its popularity is their unique material properties such as high structural strength, toughness, stiffness, ductility, and easy to fabricate that in combination metals can be machined into any complex shape and capable enough to bare heavy load and resist deformation. In addition, metals are alloys with alloying elements to further enhance its existing mechanical properties. However, metals and its alloys are susceptible to corrosion and fatigue under sever environmental and cyclic loading conditions, respectively. The metals are also loses its strength at higher temperatures and therefore halts its usage in some high temperature applications. On the other hand, polymers are chemically inert and easily formed into complex shapes but they can be used at temperature only below 300°C (573K).

In light of this, structural ceramics can be considered as an effective solution. Alumina (Al_2O_3), zirconia (ZrO_2), magnesia (MgO), silicon carbide (SiC), and silicon nitride (Si_3N_4) are grouped as structural ceramics to be considered as one of the most versatile groups of materials because of its high temperature stability, ability to resist deformation at elevated temperature, excellent wear and thermal shock resistance, chemical inertness, superior electrical properties, and lower density [1-5]. As a result, structural ceramics have found applications in a variety of industries including automobile, aerospace, medical, printing, textile, and electronic [1-5]. Despite having these superior properties, structural ceramics are hindered from several applications because of its hard and brittle nature that causes limitations towards machining into desirable components.

1.2 Common Fabrication Techniques for Structural Ceramics

The advancement of modern technology constantly drives the researchers in constant search not only for the smarter and innovative structural materials but also for efficient materials processing techniques to enhance their performance [5]. These demanding requirements stimulate the inventions and development of newer non-traditional fabrication/ processing/ manufacturing techniques [5]. Figure 1.2 shows the various conventional and non-conventional fabrication techniques generally used to shape the structural ceramics.

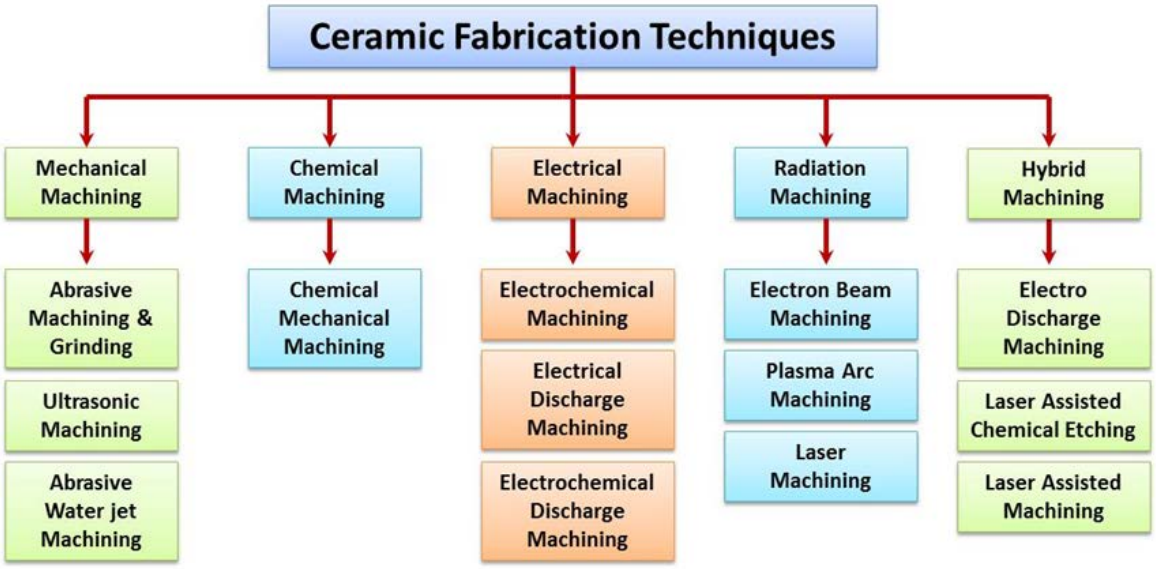

Figure 1.2 Common fabrication techniques for structural ceramics

Structural ceramics, due to their low fracture toughness (~3-5 MPa-m½) and high hardness (~1200-2200 Knoop hardness), are difficult to machine using conventional machining techniques such as grinding, cutting, polishing, and their derivative processes [5-11]. In the past, numerous investigations on precision machining of ceramic components have been conducted primarily for the cutting, grinding and polishing and their derivative processes [5-11]. Moreover, these studies reported that these machining techniques are moreover associated with several drawbacks such as unacceptable tool wear, insufficient dimensional accuracy, mechanical or

thermal damage to workpieces, lower material removal rates, and surface and subsurface cracks [5,12-16]. Among them, grinding is still considered to be the most desirable technique to machine ceramic components with good dimensional accuracy as well as surface finish [6]. However, longer machining time and higher operating costs pose a major drawback for the grinding process [7,8,17]. Furthermore, the finish products often demonstrate surface and subsurface cracks [12-14], some amount of plastic deformation [18], pulverization layers [19,20], and significant surface residual stresses [21]. Hence, a cost effective ceramic machining technique is an immediate need for several industrial applications. In this regards, laser machining is a non-contact technique that overcomes many of the drawbacks associated with conventional machining techniques. Recently, it has emerged as an innovative and potential tool for bulk material removal and fabricates complex structures of ceramics [1,2,5,17,22-25].

1.3 Laser Machining of Structural Ceramics

Many researchers [17,22-25] have demonstrated that recent development of lasers have driven the machining of advanced structural ceramics, which previously were nearly impossible to machine effectively using various conventional machining techniques. The large amount of experimental and computational works were conducted using laser-machining techniques [1,2,5,8,10,15,17,22-24,26-30], laser-assisted chemical etching [31], and laser-assisted machining [32-37] for fabricating complex-shaped structural ceramics. Laser-machining technique (both the workpiece and the laser beam are stationary), has been successfully implemented in many industrial applications [25,38-40] such as aerospace (cooling holes in nozzle guide veins and gas turbines), automotive (fuel injection nozzles), and electronic (circuit boards). However, laser machining (both the workpiece and the laser beam are stationary) is inherently associated with

several defects and many dimension-related issues. Some of the prominent issues reported are the formation of the recast layer on the walls of machined surface, spatter formation on top surface, non-parallel machined walls, lack in dimensional accuracy, larger heat affected zones, and micro-crack formation [25,41,42]. In addition, considerable amount of experimental and computational works [1,2,5,15,26,30,43,44] have been published in the past to improve the quality of laser machining by employing various types of lasers: CO_2, excimer, and Nd:YAG. These lasers can be operated either by continuous wave (CW), or pulse mode (PM), (mili-, nano, pico- and femto-second lasers). In CW, the output energy of the laser beam is constantly ON for a specific amount of time; whereas in PM, the lasers concentrate their output energy into shorter time high-power bursts. The PM lasers can either fire single pulse or a series of pulses (multiple) at regular intervals. In both cases, the instantaneous power densities can be extremely high (~10^7 J/m^2), and as a result, a larger volume of material is removed [1,2].

In the past, Samant et al. [1,2,5,26,30] used the experimental and computational approaches to understand the mechanisms of material removal during laser machining (stationary laser beam) for various structural ceramics (alumina, zirconia, magnesia, silicon nitride, and silicon carbide). Their studies show that the higher material removal rate can be achieved by using PM lasers (with applying multiple laser pulses) and considered as a preferable machining technique for structural ceramics [1,2,9,42,45]. However, the main focus of their works was to increase the material removal rates by selecting the optimal laser processing parameters, and disregard the issues related to surface finish. Hence, the undesirable surface finish produced during PM laser machining is still one of the critical issues to be resolved.

1.4 Laser-Material Interactions

During laser-material interactions, the temperature rise and fall due to heating (absorption of the laser beam) and cooling (self-quenching by bulk material; and heat losses due to external natural convective cooling and radiation) control different physical phenomena in the material during. Particularly, during laser-material interactions, when the laser beam strikes the surface of material, some part of the laser energy is lost due to the reflection and the remaining part of the energy is absorbed by the material. The absorbed laser energy, in turn, causes several phenomena (Figure 1.3), such as heating, melting, vaporization, and plume formation on the surface of material [1,2,5,15]. The effects of these phenomena predominantly depend on the laser process parameters and the material properties. The various laser processing parameters include, wavelength, energy densities of the laser beam, mode of operation (continuous or pulse), angle of incidence, scan speed, laser beam spot size, and energy distribution [1,2,5,15]. The material properties include, but are not limited to, absorptivity, thermal conductivity, specific heat, density, and latent heat. When high laser intensity ($\sim 10^6$ J/m^2) is applied to the material, localized surface melting and rapid evaporation occur. The evaporation at the melt surface is associated with the emission of neutral atoms or molecules into the gas that shield the laser-material interaction zone [43,46-48]. The evolving vapor particle from the melt pool is significantly cooler and denser than the vapor-surrounded laser-material interaction zone. Hence, the vapor particles evaporated from the melt pool in turn condensed back to the surface causing a recoil pressure on the liquid melt pool [1,2,5,15,46].

For laser beams of much greater intensity and shorter pulse duration, the resulting recoil pressure may be very high and induce the shock waves; in turn, it generates a hydrodynamic melt motion on the liquid melt pool underneath [43,46-48]. The consequence of the above effect is the

ejection of the liquid metal towards the edges which in turn forms a liquid crown or liquid pile-up as shown in Figure 1.3b.

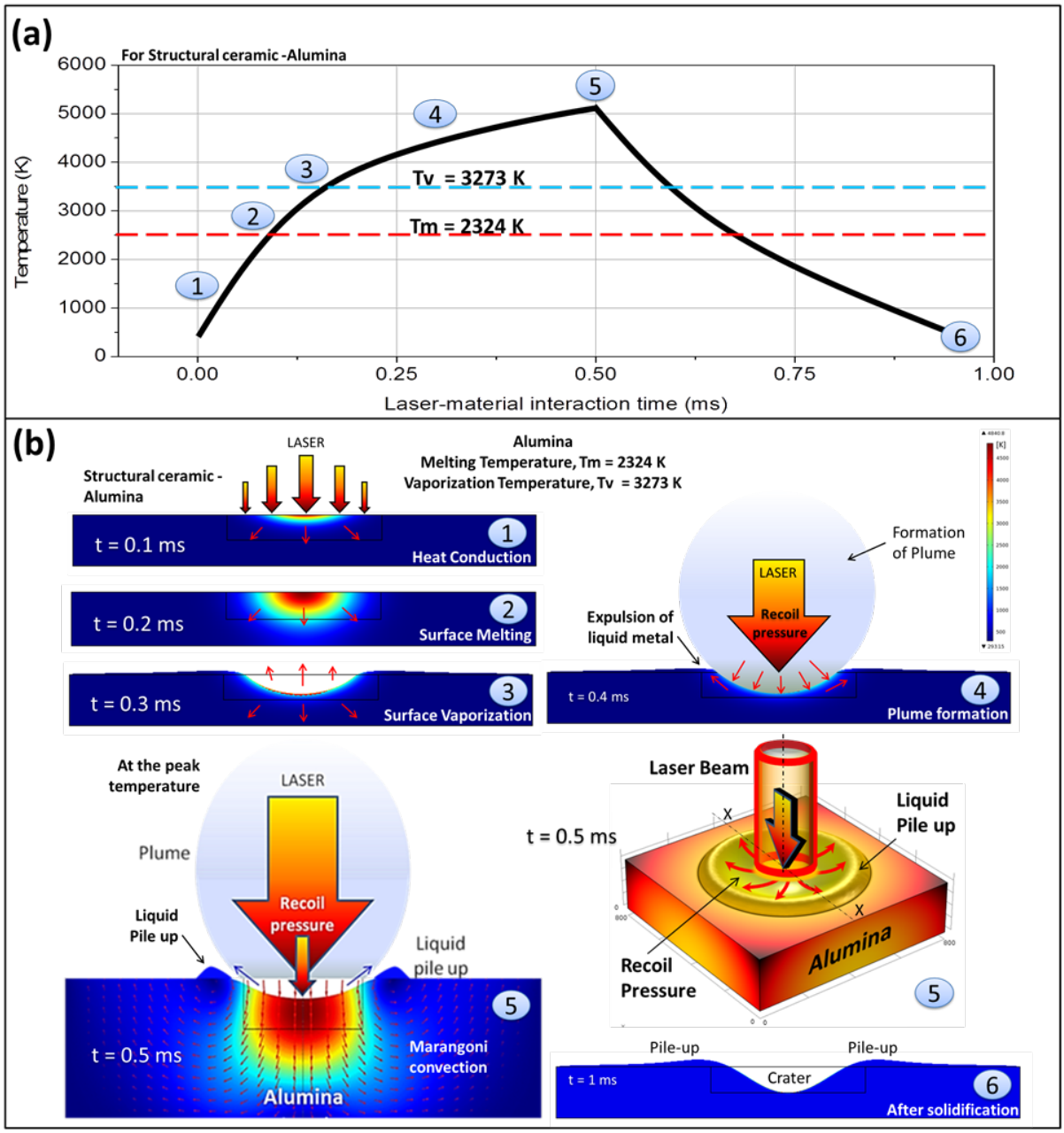

Figure 1.3 Schematic of laser-material interaction (a) Temperature versus time plot and (b) associated surface effects during laser-material interaction

At the end of the laser-material interaction, the liquid metal tends to return to its place due to gravitational force. However, due to self-quenching effects and higher cooling rates (~10^5

K/s) the liquid material solidifies instantaneously [1,2,5,15]. Further, the tangential stress exerted due to surface tension of the material gives shape to the solidified material. Thus, a pronounced surface topography is generated on the laser machined surface (Figure 1.3b).

1.5 Objective

In the laser machining process, all the physical phenomena (or dynamics) happened in small confined volume (~10^{-10} m^3) for very short time duration (< 10^{-3} s). Furthermore, due to the localized nature of laser beam the surface reaches to the extremely high temperature (> 5000 K) with in very short time (< 0.5×10^{-3} s). In addition, the in-situ measurement of the thermo-physical properties in these severe conditions such as high temperature, short time duration, and small interaction volume is an extremely difficult task. In consequence, it is extremely challenging to investigate the evolution of surface topography through experimental analyses. Hence, computational modeling approach (via finite element method-FEM/FEA) can be considered as an effective solution.

In light of this, an integrated computational and experimental approach was employed in the present efforts to investigate the evolution of surface topography/profile/roughness or physical texture during laser machining of structural ceramic alumina (Al_2O_3). The integrated computational and experimental approach overcomes the difficulties associated with the in-situ measurements of thermo-physical properties, which can provide more insight to understand the laser-material interaction and its consequent effects on the evolving surface topography /profile/ roughness/ physical texture. The computational model was designed, developed, and validated with the experimental observation for better accuracy.

CHAPTER 2

COMPUTATIONAL MODEL[2]

2.1 Classification of Laser Machining

PM laser machining can be classified as one-, two-, or three-dimensional machining to replicate generic drilling, cutting, and milling processes, respectively (Figure 1.4). Though, this classification is just for simplicity and therefore the applications of laser machining are not kept limited to these processes only.

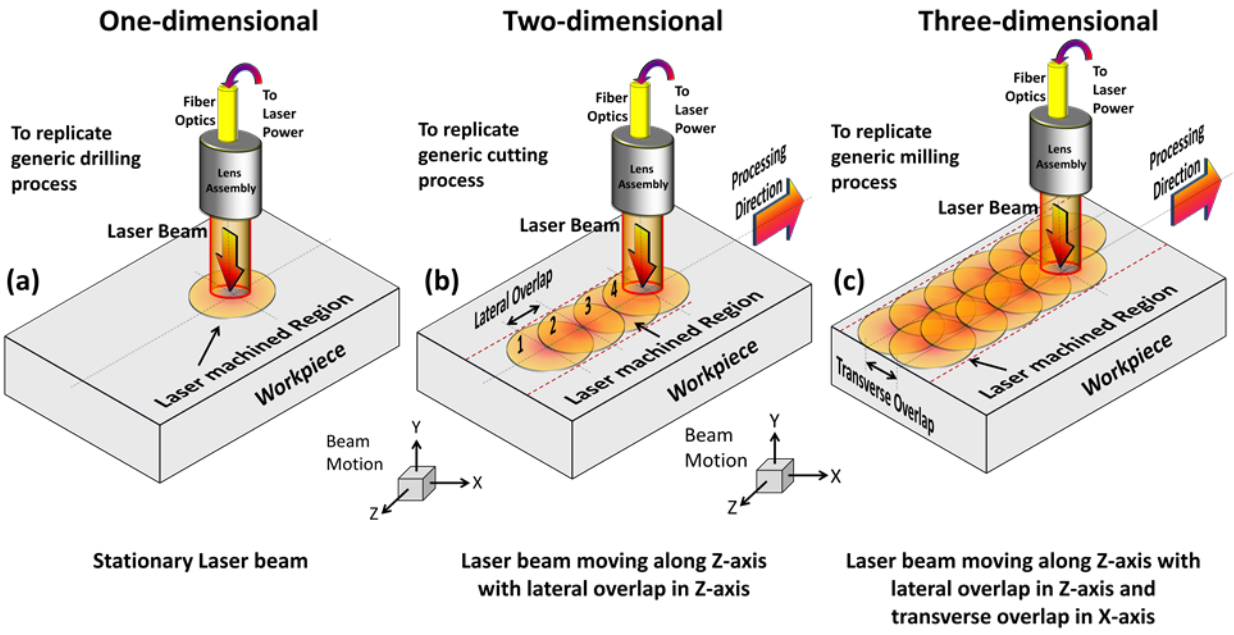

Figure 2.1 Classification of pulsed mode (PM) laser machining

One-dimensional (1D) laser machining can be achieved by keeping both the workpiece and the laser beam stationary (Figure 1.4a). While the linear motion of the laser beam or the workpiece leads to two-dimensional (2D) laser machining by moving the laser beam along Z-

[2] Parts of this chapter have been previously published, either in part or in full, from (1) Hitesh D. Vora, Soundarapandian Santhanakrishnan, Sandip P. Harimkar, Sandra K.S. Boetcher, Narendra B. Dahotre, *Journal of European Ceramic Society* 2012, 32 (16), 4205–4218 with permission from Elsevier, and (2) Hitesh D. Vora, Soundarapandian Santhanakrishnan, Sandip P. Harimkar, Sandra K.S. Boetcher, Narendra B. Dahotre, *International Journal of Advanced Manufacturing Technology* 2013, 68(1), 69-83 with permission from Springer

axis with lateral overlap in Z-axis (Figure 1.4b) and keeping workpiece stationary, or vice versa. The lateral overlap or distance between two laser pulses can be estimated by scanning speed of laser beam (Vin) divided by pulse rate (f). However, in three-dimensional (3D) machining, the laser beam is moving along Z-axis with lateral overlap in Z-axis and transverse overlap in X-axis by keeping workpiece stationary, or vice versa (Figure 1.4c). The transverse overlap or distance between two laser tracks can be provided by indexing the laser beam or workpiece in preset distance and direction, which is independent of scanning speed of laser beam (Vin) divided by pulse rate (f) values.

One-dimensional laser machining can be carried out by either a single laser pulse or multiple laser pulses. While, two- and three-dimensional laser machining only be carried out by using moving laser beam with applying multiple laser pulses in a repeated manner. Because of this distinct variation in pulse delivery (single or multiple), laser beam movement (scanning speed), and in lateral and/or transverse overlap can dramatically vary the evolving surface topography on the machined surface. This is truly a footprint of selected laser machining parameters such as scanning speed of laser beam (Vin), application of laser pulses at predefined pule rates (f), lateral overlap or distance between two laser pulses, and transverse overlap or distance between two laser tracks.

Although, the nature of surface topography may vary, principally the various physical phenomena behind formation of the surface topography remain same for 1-, 2-, or 3D laser machining. Hence, the prime objective of the present study is to systematically understand the mechanism of evolution of surface topography during the impact of a single laser pulse under one-dimensional machining. Subsequently, this understanding will be extended to predict the surface topography during multi-dimensional laser machining processes.

2.2 One-dimensional (1D) Laser Machining - Single Laser Pulse

In the present efforts, the multiphysics computational model was designed and developed to simulate the effects of single laser pulse on the evolving surface topography (Figure 2.2).

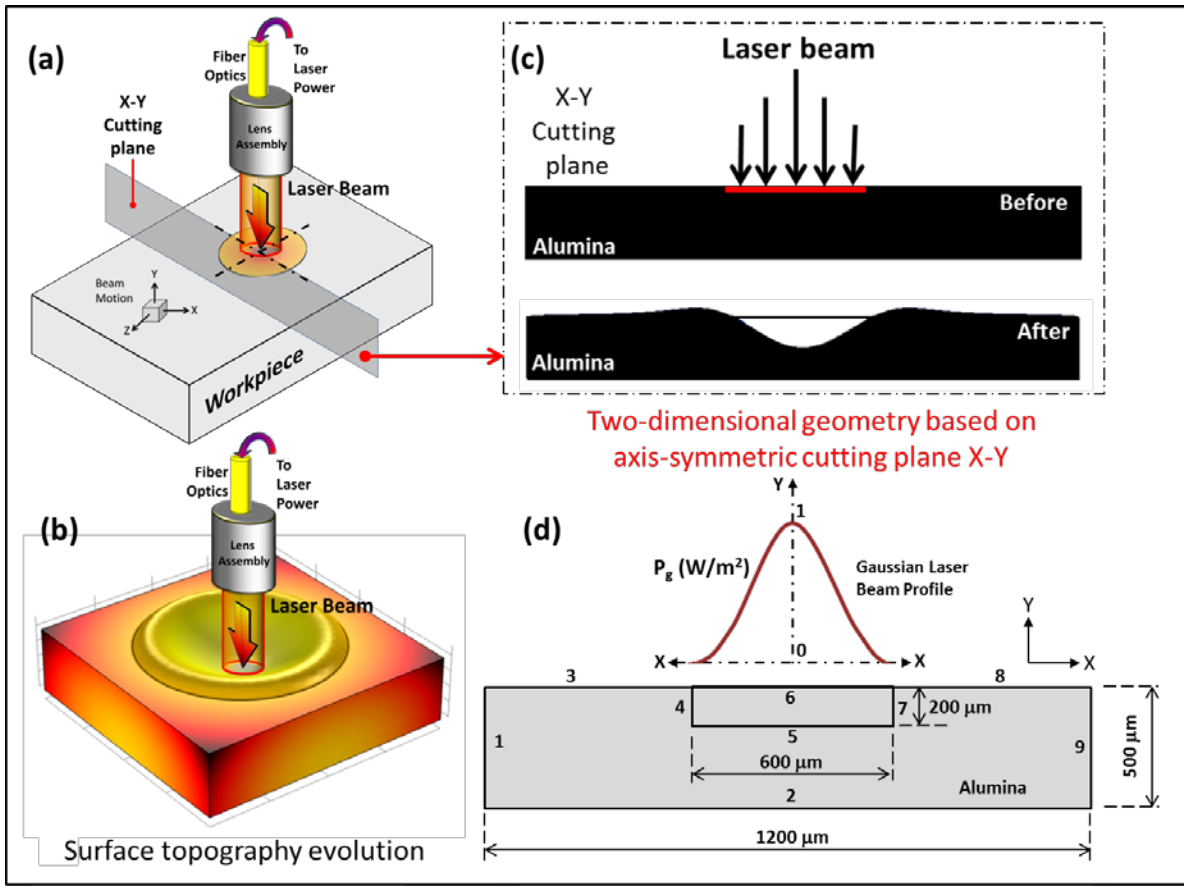

Figure 2.2 Schematic of 1D laser machining processes (a) single pulse laser machining, (b) evolution of surface topography, (c) evolution of surface topography on the axis-symmetric cutting plane X-Y, and (d) geometry for computational model

The computational model incorporating the multiphysics effects (heat transfer and computational fluid dynamics) was developed to predict the temperature history, cooling rates, and fluid velocity that influence the surface topography of alumina subjected to various laser machining conditions. In order to effectively utilize the computation time and the cost, a geometry based on X-Y symmetric cutting plane was designed for the computational modeling

(Figure 2.2d). The material properties of alumina and the laser machining parameters used in the computational model are summarized in Table 1.

Table 1 Material properties of alumina (99.6%) and laser machining parameters

Material properties of alumina (99.6%)			
Property	**Nomenclature**	**Value (units)**	**References**
Density	ρ	3800 (kg/m^3)	[49]
Specific heat at constant pressure	C_p	880 (J/kg.K) for $T < T_m$	[49]
Thermal conductivity	k	35 (W/m.K)	[49]
Melting temperature	T_m	2324 (K)	[49]
Vaporization temperature	T_v	3273.15 (K)	[49]
Latent heat of melting	L_m	1067.43 (J/g)	[49]
Latent heat of evaporation	L_v	1066.5 (J/g)	[49]
Mass of vapor molecule	M_v	1.693e-25 (kg/atm)	[49]
Temperature derivative of the surface tension	γ	-8e-5 (N/(m.K))	[50]
Thermal expansion coefficient	α	8.4e-6 (1/K)	[49]
Dynamic Viscosity	μ	1(Pa.s for T < 2190 K) and 0.001 (Pa.s for T > 2500K)	[50]
Laser machining parameters			
Parameter	**Nomenclature**	**Value (units)**	**References**
Pulse energy and corresponding average laser energy density	E_p E_d	1, 1.5, 2, 2.5, 3 (J) 3.5, 5.3, 7.1, 8.8, 10.6 ($\times 10^6$ J/m^2) respectively	-
Pulse width	P_w	0.5×10^{-3} (s)	-
Beam diameter	D	0.6×10^{-3} (m)	-
Absorptivity	A	0.25	[27]
Heat transfer coefficient	h	10 ($W/m^2.K$)	[16]
Emissivity	ε	0.7	[1,2]
Half-width of the curve	ΔT	30 (K)	-
Reference point to represents the center of the laser beam in the geometry along x-axis	x_r	0.6×10^{-3} (m)	-
Standard deviation of the Gaussian laser beam	ϕ	0.1×10^{-3} (m)	-
Ambient temperature	T_0	293.15 (K)	-
Initial temperature	T_i	293.15 (K)	-
Stefan-Boltzmann constant	σ	5.67×10^{-8} ($W/m^2.K^4$)	[49]
Universal gas constant	R	8.314 (J/mol.K)	[49]
Gravitational constant	g	9.81 (m/s^2)	[49]

The laser machining involves change in phases and associated effects on the surface topography. During heating, as the temperature increases, material changes its phase from solid

to liquid and liquid to vapor phase. The portion of material that attains the temperature above vaporization temperature is consequently removed due to evaporation. Similarly, molten material changes its phase from liquid to solid during cooling cycle. In order to simulate the phase change effects and predict the instantaneous surface deformation, the present computation model was designed into two steps as presented in the flow diagram (Figure 2.3).

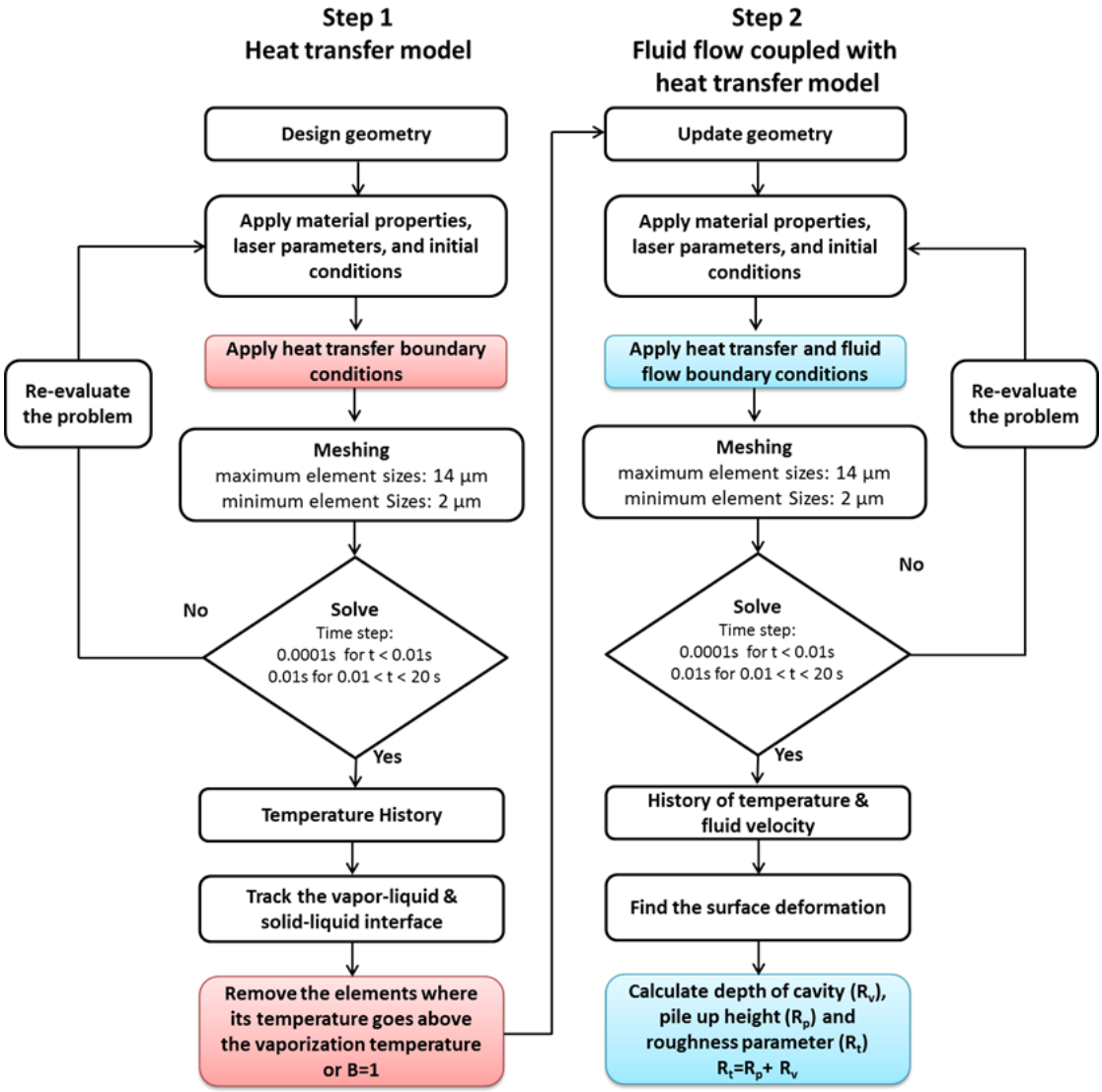

Figure 2.3 Flow chart for computational model - 1D laser machining

In the present efforts, the integrated computational approach involving various physical phenomena for predicting surface profile during single pulse laser machining of alumina is schematically presented in Figure 2.4.

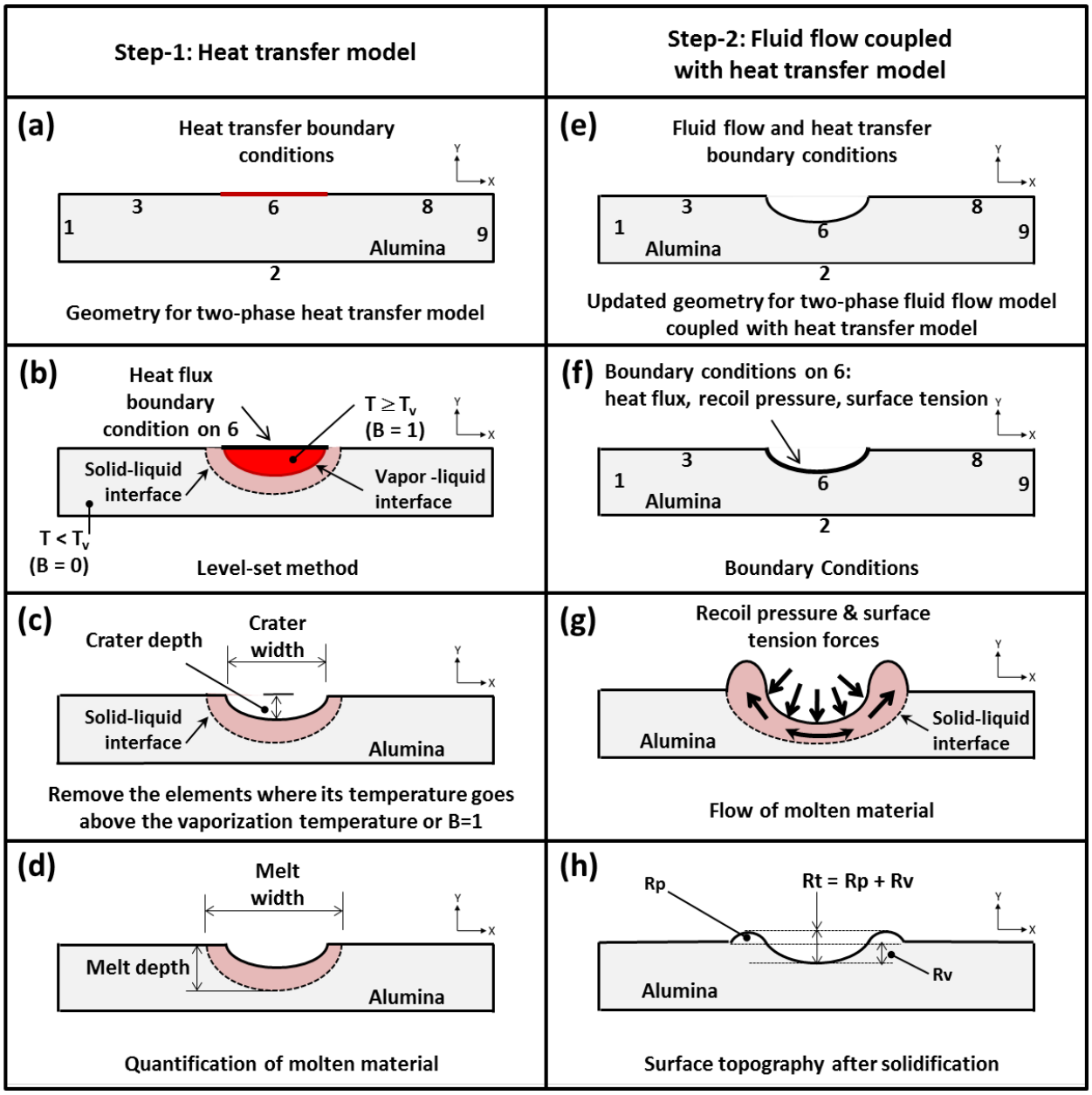

Figure 2.4 Schematic of a physical model in two-step computational modeling approach to predict the surface topography

The computational model in Step-1 considered the material loss due to evaporation via multi-phase (solid-liquid-vapor) heat transfer. The main objective of Step-1 model is to predict the geometry of a crater produced via evaporation losses of the material. In Step-1, the level-set method was employed to trace the interfaces between liquid-solid and vapor-liquid phases. In Step-1, the elements whose temperature reached above the vaporization temperature were excluded from the geometry. The dimensions of crater (depth and width) play a significant role in predicting the final surface profile. Therefore, in Step-2 model the crater geometry predicted from Step-1 was considered as a starting surface profile. Same as in Step-1, the multi-phase fluid flow model coupled with the heat transfer and phase change kinetics was employed in Step-2 model. As a prime objective of Step-2, the contribution of deformation of liquid material pool in the crater under various forces (recoil pressure, surface tensions, and gravitational forces) to generation of final solidified surface profile was predicted (Figure 2.3 and 2.4).

2.2.1 Heat Transfer Model

In Step-1, the two-dimensional axis-symmetric computational model using COMSOL™ Multiphysics that incorporated the multi-phase (solid-liquid-vapor) heat transfer and phase change kinetics [51]. The governing equation for transient two-dimensional heat transfer in Cartesian coordinates is given by Eq. (1).

$$\rho c_p \left[\frac{\partial T}{\partial t}\right] = k\left[\left(\frac{\partial^2 T}{\partial x^2}\right) + \left(\frac{\partial^2 T}{\partial y^2}\right)\right] \quad (1)$$

When a material changes phase, for instance from solid to liquid, energy is added to the solid. Instead of creating a temperature rise, the energy alters the material's molecular structure. Equations for the latent heat of phase changes appear in many texts but their implementation is nonstandard. Heat consumed or released by a phase change affects temperature profile, depth of

surface melting, and fluid flow. In this case, the constant Cp value (880 J/kg.K) was chosen for the temperature less than melting temperature. However, the specific heat ($C_{p)}$ related to the phase transition was chosen for the temperature above the melting temperature from expressed as C_p1 in the Eq. (1) [52] .

$$\mathrm{Cp1} = \mathrm{Cp} + \delta_m(L_m) + \left(\frac{L_m}{T_m}\right) \cdot H'\big((T - T_m), \Delta T\big) + \delta_v(L_v) + \left(\frac{L_v}{T_v}\right) \cdot H'\big((T - T_v), \Delta T\big) \qquad (2)$$

$$\text{where,} \qquad \delta_m = \frac{\exp\left[-\left(\frac{(T - T_m)^2}{\Delta T^2}\right)\right]}{\Delta T\sqrt{\pi}} \text{ and } \delta_v = \frac{\exp\left[-\left(\frac{(T - T_v)^2}{\Delta T^2}\right)\right]}{\Delta T\sqrt{\pi}}$$

Here, smoothing of thermal property is carried out by using COMSOL's built in function called as smooth Heaviside function, H' (or flc2hs). T_m is the melting point and ΔT denotes the half-width of the curve, in this case set to 30 K, representing half the transition temperature span. Also, Latent heat as a normalized Gaussian pulse around the melting and vaporization temperature was denoted by the δm and δv in (1/K), respectively.

The level-set method, developed by Sussman at el. [53] was incorporated into the model to track the interfaces between liquid-solid and vapor-liquid phases [52].

$$B = 1 \qquad \text{for } (T > T_x + \Delta T) \qquad (3)$$

$$B = \frac{(T - T_x + \Delta T)}{2\Delta T} \qquad \text{for } (T_x - \Delta T) \le T \le (T_x + \Delta T) \qquad (4)$$

$$B = 0 \qquad \text{for } (T < T_x - \Delta T) \qquad (5)$$

For alumina, T_x can be T_v to distinguish vapor phase from liquid phase; and T_m for liquid phase from solid phase. The B ranges from 0 to 1. For $T_x = T_v$, B=1 indicates 100% vapor phase, and B=0 designates 0% vapor phase. Similarly, for $T_x = T_m$, B=1 indicates 100% liquid phase, and B=0 designates 0% liquid phase. The interphases can be tracked between B= 0 and 1. The

tracking of the phases facilitates the quantification of the material lost due to vaporization as well as the prediction of crater and melt pool dimensions.

2.2.2 Initial and Boundary Conditions

In the present computational model, the axis-symmetric geometry (Figure 2.2d) is assigned with the various boundary conditions, which are summarized in the Table 2.

Table 2 Boundary conditions

Physics	Physical condition	Boundary#	Boundary condition	Variable
Heat transfer	Laser beam	6	Heat flux	P_g
	Natural convection cooling	1,3,8,9	Convective cooling	h
	Radiation	1,3,8,9	Surface-to-ambient radiation	μ
	Insulation	2	Insulation	-
	Neutral	4,5,7	Neutral	-
Fluid flow	Recoil pressure	6	Normal boundary stress	P_r
	Surface tension	3,6,8	Boundary stress	γ
	Free face	3,6,8	Open boundary	-

Boundary 6 shown in Figure 2.2d is exposed to the boundary conditions of heat flux, natural convective cooling, and surface-to-ambient radiation which are presented in Eq. (6).

$$-k\frac{\partial T}{\partial y} = -\varphi P_g + h[T - T_0] + \varepsilon\sigma[T^4 - T_0^4] \quad (6)$$

$$\text{where, } \varphi = 1 \text{ for } 0 \le t \le P_w, \text{ and } \varphi = 0 \text{ for } t \ge P_w$$

The laser-power distribution used in the model is Gaussian as expressed in Eq. (7).

$$P_g = A\left[\frac{E_p}{P_w\left(\frac{\pi}{4}D^2\right)}\right]\exp\left[-\left(\frac{(x - x_r)^2}{2\emptyset^2}\right)\right] \quad (7)$$

Boundaries 1, 3, 6, 8 and 9 shown in Figure 2.2d are subjected to natural convective cooling and surface-to-ambient conditions. Eq. (8) and (9) are used to represent the boundary conditions for the boundaries 3 and 8, and 1 and 9 respectively.

$$-k\frac{\partial T}{\partial y} = h[T - T_0] + \varepsilon\sigma[T^4 - T_0^4] \quad (8)$$

$$-k\frac{\partial T}{\partial x} = h[T - T_0] + \varepsilon\sigma[T^4 - T_0^4] \quad (9)$$

Boundary 2 is subjected to an insulated boundary.

$$\frac{\partial T}{\partial y} = 0 \quad (10)$$

In Step-1, the objective of the model is to predict the temperature history and consequently the vapor-liquid and solid-liquid interfaces. Based on this analysis, the elements whose temperature was above the vaporization temperature ($T > T_v$) or B=1, were removed, indicating the loss of material due to vaporization. Then, the updated geometry was used in the Step-2 of the model.

2.2.3 Fluid Flow Coupled with Heat Transfer Model

In Step-2, the computational model considered the multi-phase fluid flow coupled with heat transfer and phase change kinetics. The new geometry was drawn by considering the material loss due to vaporization from the Step-1 results. The governing equations for conservation of mass, momentum, and energy for two-dimensional transient, incompressible-laminar flow coupled with natural convection heat transfer are listed below.

$$\frac{\partial u}{\partial x} + \frac{\partial v}{\partial y} = 0 \quad (11)$$

$$\rho\left(\frac{\partial u}{\partial t} + u\frac{\partial u}{\partial x} + v\frac{\partial u}{\partial y}\right) = -\frac{\partial p}{\partial x} + \mu\left[\frac{\partial^2 u}{\partial x^2} + \frac{\partial^2 u}{\partial y^2}\right] \quad (12)$$

$$\rho\left(\frac{\partial v}{\partial t} + u\frac{\partial v}{\partial x} + v\frac{\partial v}{\partial y}\right) = -\frac{\partial p}{\partial y} + \mu\left[\frac{\partial^2 v}{\partial x^2} + \frac{\partial^2 v}{\partial y^2}\right] + \rho g\alpha(T - T_m) \quad (13)$$

$$\rho c_p \left(\frac{\partial T}{\partial t} + u\frac{\partial T}{\partial x} + v\frac{\partial T}{\partial y}\right) = k\left[\frac{\partial^2 T}{\partial x^2} + \frac{\partial^2 T}{\partial y^2}\right] \quad (14)$$

The Boussinesq approximation is used to represent the convection induced by the surface conditions and volume force[54,55]. The Step-2 of the computational model also utilizes the phase change Eq. (2) along with heat transfer boundary conditions described in Eq. (6-10).

Boundary 6 shown in Fig. 3 is subjected to the action of two forces. The first force is due to the recoil pressure created by vapor expansion, and the second force is due to surface tension [50]. The evaporation-induced recoil pressure (P_r) at the evaporating surface depends on the incident average laser power density [26,30] and is given in Eq. (15).

$$P_r = (P_g)\frac{1.69}{\sqrt{L_v}}\left[\frac{\sqrt{\left(\frac{k.T_s}{M_v.L_v}\right)}}{1 + 2.2\left(\frac{k.T_s}{M_v.L_v}\right)^2}\right] \text{only when } T_s \geq T_v \quad (15)$$

The temperature fields determined from the computational model facilitate the calculation of evaporation-induced recoil pressure at the evaporating surface during laser machining of alumina. In this calculation, the experimentally verified physical model of melt hydrodynamics and laser-induced evaporation proposed by Anisimov [46] and Semak [47] were used. In the current model, the recoil pressure is applied only when the temperature is above the vaporization temperature ($T \geq T_v$).

The fluid flow prompted by surface tension is referred as Marangoni convection. This phenomenon has a crucial importance for penetration and enlargement of the melted pool. It derives from the surface tension gradients brought on by the temperature gradients along the free surface. Due to the Marangoni convection, the forces prompted on the liquid/air interface were incorporated such a way that the shear stress is proportional to the temperature gradient on the surface. To do so, the weak term was added from the Weak Contribution feature of the laminar

flow interface, shown in Eq. (16). This term imposed the velocity in x-direction and overrides the slip boundary condition [54]. In the impact zone, where the temperature is at its highest, the surface tension is at its weakest. The fluid therefore moves from the center to the edges of the molten pool.

$$\text{test}\,(\mathrm{u}) * \left[\frac{\partial \gamma}{\partial \mathrm{T}} \frac{\partial \mathrm{T}}{\partial \mathrm{x}}\right] \tag{16}$$

The temperature-dependent surface tension (γ) and dynamic viscosity (μ) for alumina are presented in Eq. (17-18) for the temperature range between 2190-2500 K [50].

$$\gamma(\mathrm{T}) = 0.64 - 8.2 \times 10^{-5}(\mathrm{T} - \mathrm{T_m}) \tag{17}$$

$$\mu(\mathrm{T}) = 3.2 \cdot \left[\exp\left(\frac{43.2 \times 10^3}{\mathrm{RT}}\right)\right] \tag{18}$$

The difference between the dynamic viscosity of solid phase and liquid phase is very large and the corresponding dynamic viscosity values for solid and liquid phases are presented in Table 1.

2.2.4 Meshing

The computational model was built using heat transfer and fluid flow physics in COMSOL^{TM} Multiphysics. A mesh-sensitivity analysis was performed for six different triangular mesh sizes. Based on the mesh size sensitivity analysis, maximum and minimum element sizes of 14×10^{-6} m and 2×10^{-6} m respectively were used in the model. The computational model was solved initially for small time steps (0.0001 s for $t < 0.01$ s) to grasp all the details precisely. Later, large time steps were used (0.01s for $0.01 < t < 20$ s) to economize the computational time and resources. A domain probe (virtual thermocouples) was assigned to track the variation in temperature and fluid velocity of each time step.

2.3 One-dimensional (1D) Laser Machining – Multiple Laser Pulses

For pulse mode (PM) lasers, one-dimensional laser machining is also carried out by supplying multiple laser pulses by keeping both workpiece and laser beam stationary (Figure 2.5). The average laser energy density (energy per pulse/surface area of laser beam) in each case is very high (~10^6 J/m^2) which results in a high loss of material. By delivering an increased number of pulses, higher material removal rates can be achieved. In order to obtain higher material removal rates, PM lasers deliver multiple laser pulses (which is preferred for laser machining of structural ceramics). Therefore, in the present study, the effect of multiple laser pulses on the evolution of surface topography is modeled to understand the laser-machining mechanism for various conditions. Subsequently, this understanding can be extended to predict the surface topography during multi-dimensional laser machining processes.

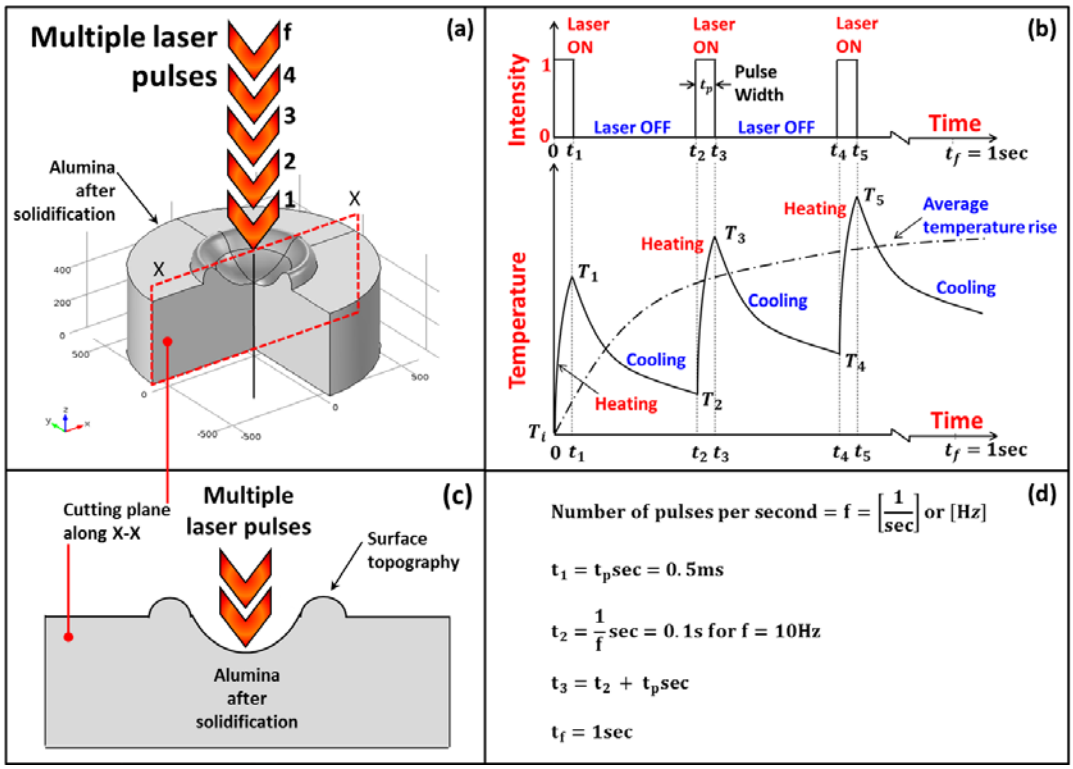

Figure 2.5 Schematic of 1D laser machining processes (a) multiple pulse laser machining process, (b) temperature as function of time, (c) evolution of surface topography, and (d) laser pulsing parameters

In PM laser machining, the multiple laser pulses of short pulse width are delivered in a repeated manner (Figure 2.5a and 2.5b). The material removal during laser machining is carried out either by evaporation or by melt ejection, which solely depends on the laser machining parameters such as average energy density, pulse width, and pulse rate (repetition rate). The laser (or heating) is ON (Figure 2.5b) during the application of first pulse (till t_1) with preset value of pulse width followed by cooling until the end of the first pulse (time $t_2 = 1/f$ second). The surface temperature increases from initial temperature (T_i) to T_1 during heating, while during cooling the temperature decreases from T_1 to T_2 (where, $T_1 > T_2 > T_i$). Subsequently, the second pulse is supplied from time t_2 to t_3 and again cooling until time t_4. This pulse train successively delivers a specific number of pulses over the entire time of machining operation (until time t_f). However, during the application of multiple laser pulses, the temperature at the beginning of every pulse was always higher than the initial temperature (T_i) causing a gradual rise in average surface temperature (Figure 2.5b). Furthermore, the variations in surface temperature, in turn, influence the mechanism of evolution of surface roughness (topography). Hence, the distinct surface topography is generated (Figure 2.5c) due to the impact of multiple laser pulses based on the laser pulsing parameter (Figure 2.5d).

A two-dimensional axisymmetric computational model, which incorporates fluid flow and heat transfer, is developed using COMSOL^{TM} Multiphysics (Figure 2.6). The model is used to predict the temperature, cooling rate, and fluid velocity (all which influence the surface topology of alumina) after the surface is subjected to various laser-machining conditions. In order to predict the surface deformation under the application of multiple laser pulses, a two-step modeling approach was employed in the present computational model, which is same as previously used for single pulse 1D laser machining, (Figure 2.3 and 2.4).

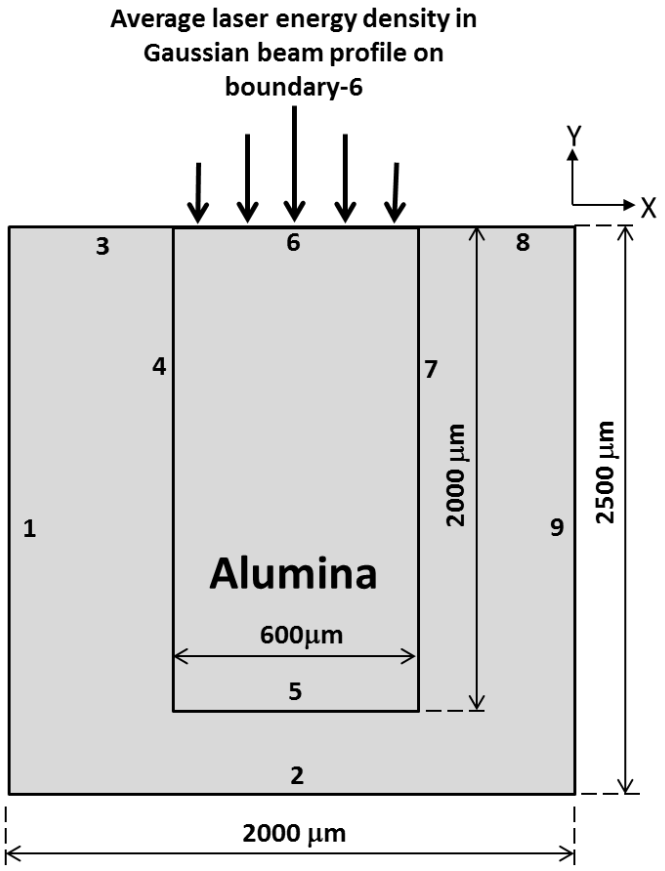

Figure 2.6 Two-dimensional geometry used in the computational model

In Step-1, the multi-phase (solid-liquid-vapor) heat transfer model is incorporated to evaluate the material loss due to evaporation which is used to predict the geometry of a crater. In order to get the geometry-independent solution, a mesh sensitivity analysis was carried out for six different mesh sizes and the optimal mesh size was used for the computation. The level-set method was also employed in Step-1 to identify liquid-solid and vapor-liquid interfaces. In Step-1, the elements identified as vapor phase are excluded from the geometry. The geometry of the crater (depth and width) evaluated from Step-1 plays an important role in predicting the final surface profile. Therefore, the crater geometry predicted from Step-1 is considered as an initial surface profile for Step-2. In Step-2, the multi-phase fluid flow model coupled with heat transfer and phase change kinetics is employed. The prime objective of Step-2 is to estimate the

contribution of the deformation of the liquid material pool inside of the crater under various forces (recoil pressure, surface tensions, and gravitational forces) and to predict the final surface topography. This integrated computational approach involves various physical phenomena for predicting the surface profile during multiple-pulse laser machining of alumina (Figure 2.4).

2.3.1 Heat Transfer Model

During laser machining, the material undergoes phase change (solid to liquid to vapor or vice-versa). In addition, the heat (latent heat of fusion and evaporation) consumed or released during the phase transition significantly influence the magnitude of surface temperature, recoil pressure, melt pool size, and fluid velocity. Therefore, the temperature-dependent properties of alumina such as density, thermal conductivity, and specific heat are specifically incorporated in the computational model. The change in density and thermal conductivity with respect to temperature (ranging from 293.15 K to 3500 K) is illustrated in Figure 2.7 [1,2,27,49,50,56]. However, the remaining material properties of alumina including the specific heat ($C_{p,}$ Eq. (2)), as summarized in the Table 1, are incorporated in the model. In addition, Table 3 summarizes the laser-machining parameters used in the computational model.

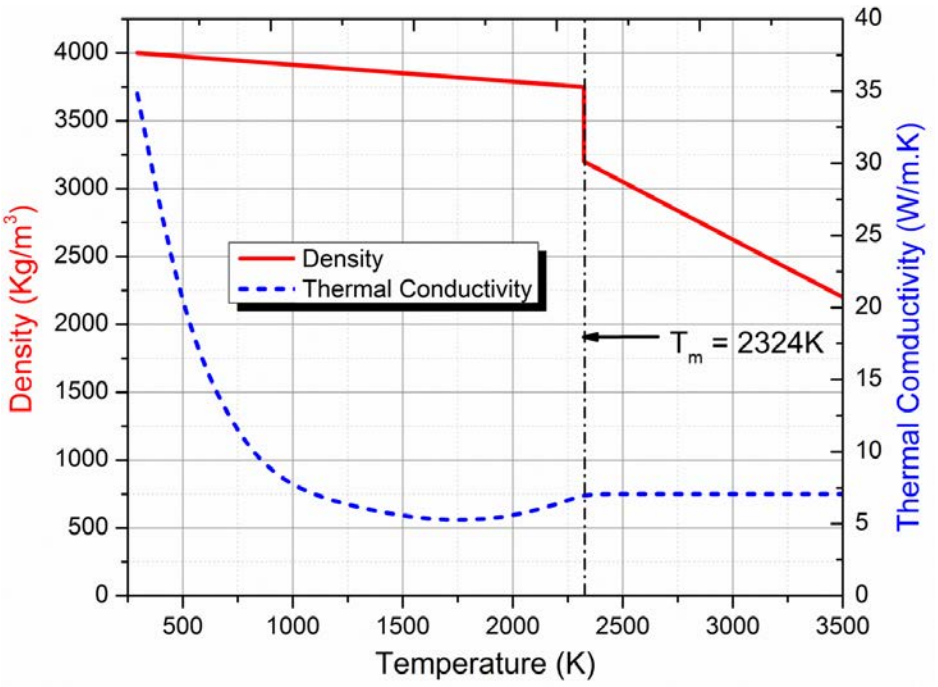

Figure 2.7 Temperature dependent material properties of alumina (a) density, and (b) thermal conductivity

Table 3 Laser machining parameters for 1D Multi-pulse laser machining

Parameter	**Nomenclature**	**Value (units)**	**References**
Number of laser pulses	f	10,20,30,40,50 pulses	-
Pulse energy(E_p) and corresponding average laser energy density(E_d)	$E_d = \frac{E_p}{\left(\frac{\pi}{4}D^2\right)} \times f$	1 (J) 3.5, 7.1, 10.6, 14.1, 17.7 ($J/m^2 \times 10^7$) respectively	-
Pulse width	P_w	0.5 (ms)	-
Beam diameter	D	0.6 (mm)	-
Emissivity	ε	0.7	[1-2]
Heat transfer coefficient	h	10 ($W/m^2.K$)	[16]
Absorptivity	A	0.25	[27]
Half-width of the curve	ΔT	30 (K)	-
Reference point to represents the center of the laser beam	x_r	1000 (μm)	-
Standard deviation of the Gaussian laser beam.	ϕ	100 (μm)	-
Ambient temperature	T_a	293.15 (K)	-
Initial temperature	T_i	293.15 (K)	-

2.3.2 Simulation of Multiple Laser Pulses

The governing equations and the various boundary conditions employed in the present multi-pulse computational model are same as previously used for the single pulse 1D laser machining, from Eqs. (1-5) and (7-18). In the present work, multiple pulses (10, 20, 30, 40, and 50) are delivered in durations of 1s. Thus, analytic function (β) was designed to simulate the repetition of multiple laser pulses that are expressed by Eq. (19) [51].

$$-k\frac{\partial T}{\partial y} = -\beta P_g + h[T - T_0] + \varepsilon\sigma[T^4 - T_0^4] \tag{19}$$

$$\text{where, } \beta = \text{rect1}\left(\text{mod}\left(t, \frac{1}{f}\right)\right) \tag{20}$$

As discussed earlier (Figure 2.5b), during the application of the first pulse, the laser is ON with a specific value of pulse width (P_w = 0.5ms) followed by cooling until the end of first pulse (time t_2 = 1/f second). Hence, the laser ON time is simulated by the rectangle function (lower and upper limit of 0 and 0.5ms respectively). The β function only works when $t \geq 0$ and $t \leq 1$s, so that it simulates the pulse train of 1s.

2.4 Two-dimensional (2D) Laser Machining

In extension of the previous work (1D laser machining – Single and multiple laser pulses), the present efforts investigated the influence of moving PM laser beam (multiple laser pulses, lateral overlap, stationary workpiece) on the surface topography (finish/roughness) during laser machining via integrated computational and experimental approach to mimic/replicate the generic cutting process. In the present effort, computational model with three-dimensional geometry was developed under the platform of COMSOL™ multiphysics finite-element software and then validated with the experimental observations.

During moving PM laser machining, the laser beam or the workpiece is travelling in relation to each other and the multiple laser pulses of short pulse width (~0.5ms) are delivered in a repeated manner (Figure 2.8). The material removal during laser machining is carried out either by evaporation or by melt ejection, which solely depends on the selected laser machining parameters such as average energy density, pulse width, scanning speed and pulse rate. The main goal of the present efforts is to obtain the better surface finish during moving PM laser machining and therefore the selection of lowest laser energy density per pulse (i.e. 3.5×10^{6} J/m^{2}) can be more appropriate to reduce the losses due to evaporation.

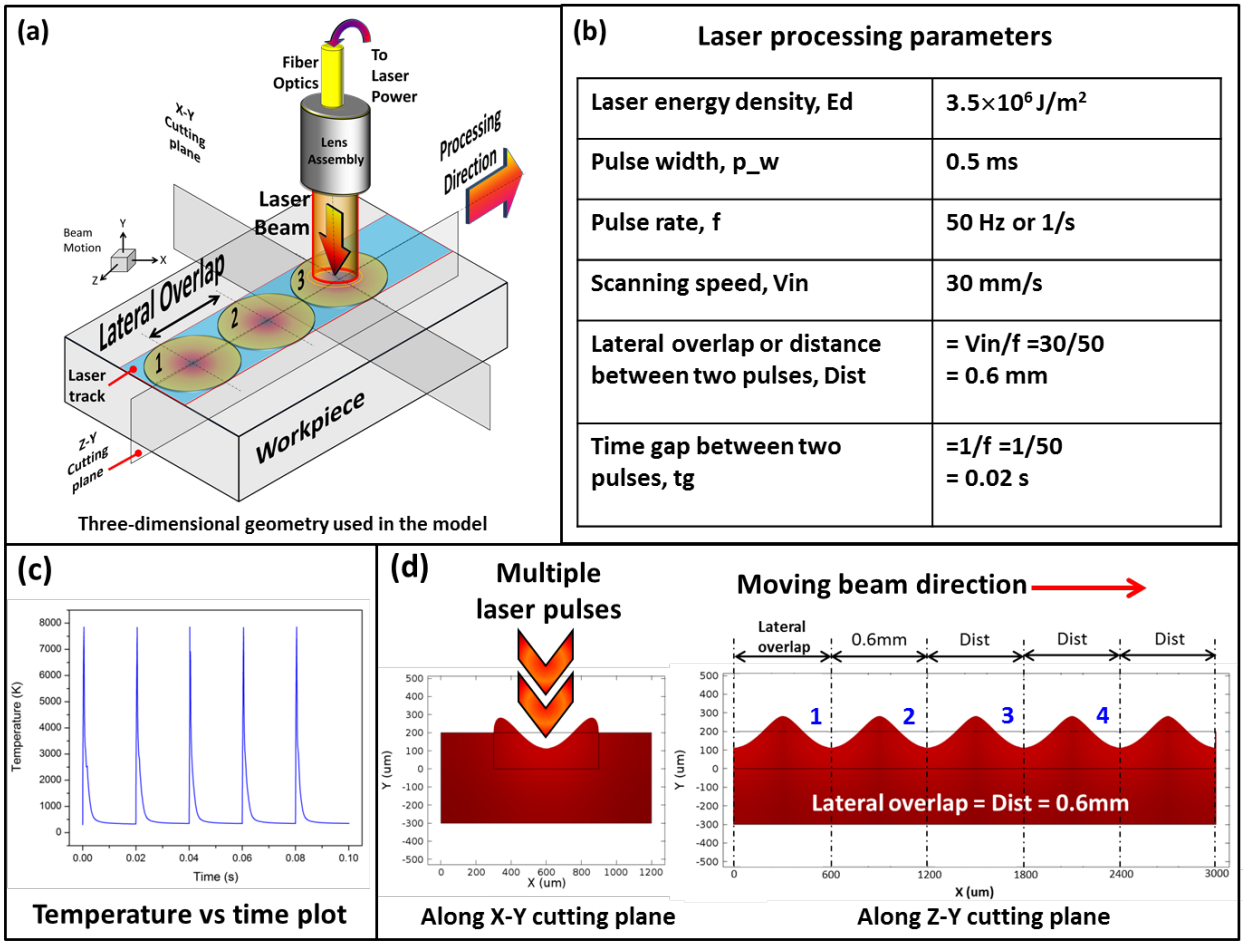

Figure 2.8 Schematic simulation of moving laser beam during 2D laser machining processes (a) geometry used in the model, and evolution of surface topography (roughness) on (b) laser processing parameters, (c) temperature profile, and (d) evolving surface topography along X-Y and Z-Y cutting planes

During PM moving laser machining, the laser beam is constantly moving along the principle axis (Z-axis), and therefore the distance between two pulses (lateral overlap), Dist, can play an important role in evolving surface roughness. Thus, the appropriate selection of scanning speed (Vin) and pulse rate (f) can change the evolving surface roughness (Figure 2.8a and 2.8b). In addition, the pulse rate (f) varies the time gap between two consecutive laser pulses (tg) which subsequently alters the temperature profile (Figure 2.8b and 2.8c) and its resultant effect on the surface roughness (Figure 2.8d). To accurately model all these phenomena and numerous modeling challenges, the three-dimensional (3D) computational model was developed using COMSOL^{TM} multiphysics to precisely simulate the moving PM laser machining process. The model incorporating the multiphysics (heat transfer and computational fluid dynamics) effects to estimate the temperature field, cooling rates, and velocity of molten material that in turn influence the generation of surface topography/profile/roughness under the application of different laser processing parameters. A multi-step modeling methodology was employed in the present computational model to evaluate the surface topography/profile/roughness under the application of multiple laser pulses and moving laser beam, which is systematically presented in the flow diagram (Figure 2.9 and 2.10).

Both, Step-1 and Step-2 were specifically designed to provide adequate accuracy in predicting the surface deformation during PM moving laser beam machining condition by incorporating the temperature-dependent material properties for density (ρ), thermal conductivity (k), specific heat (Cp), surface tension (γ), and dynamic viscosity (μ) of alumina which can be found from Table 1, Figure 2.7, and Eqs. (2, 17-18). The laser-machining parameters used for model and experiments are enumerated in Table 4.

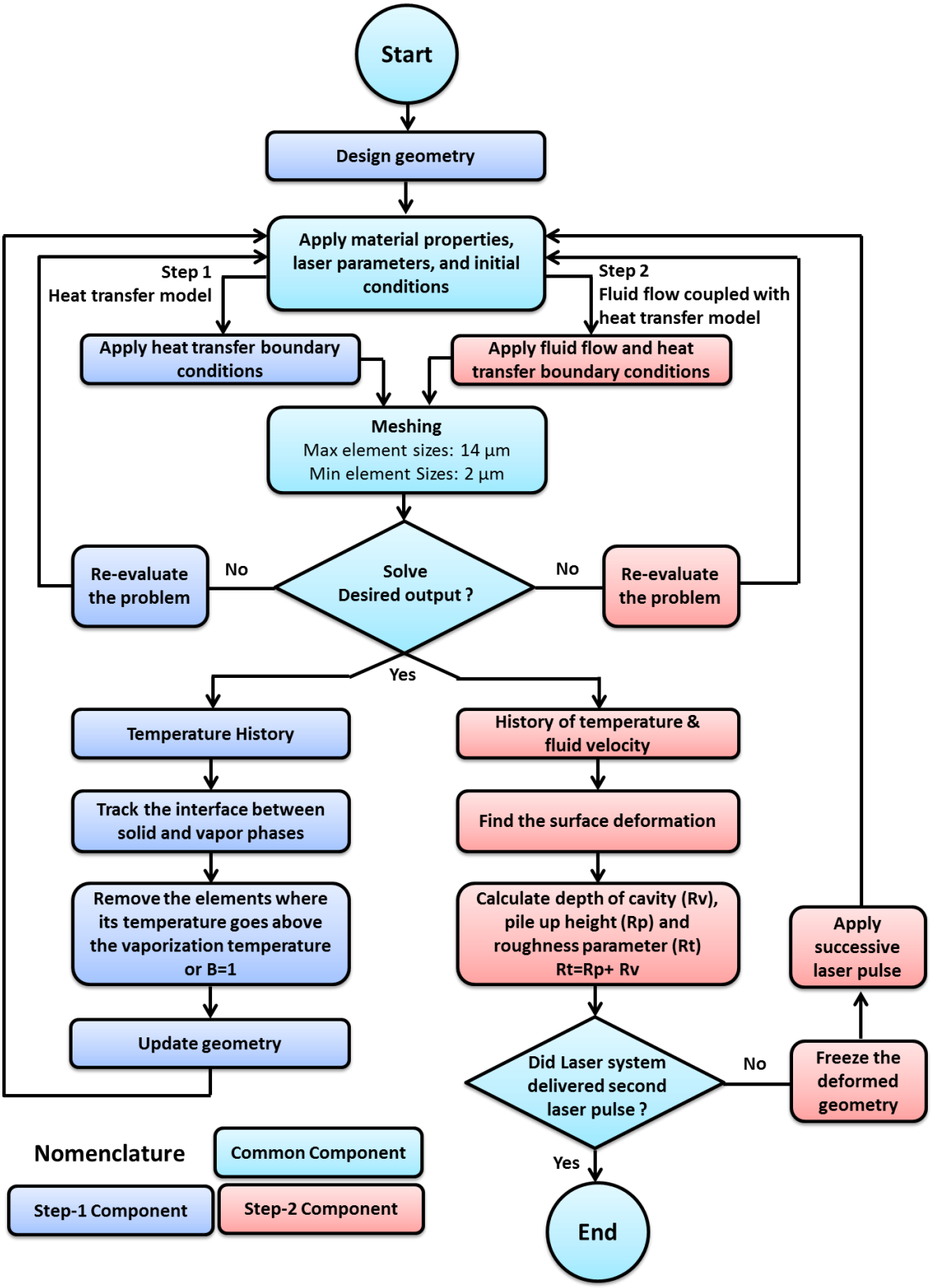

Figure 2.9 Flow chart of computational model - 2D laser machining

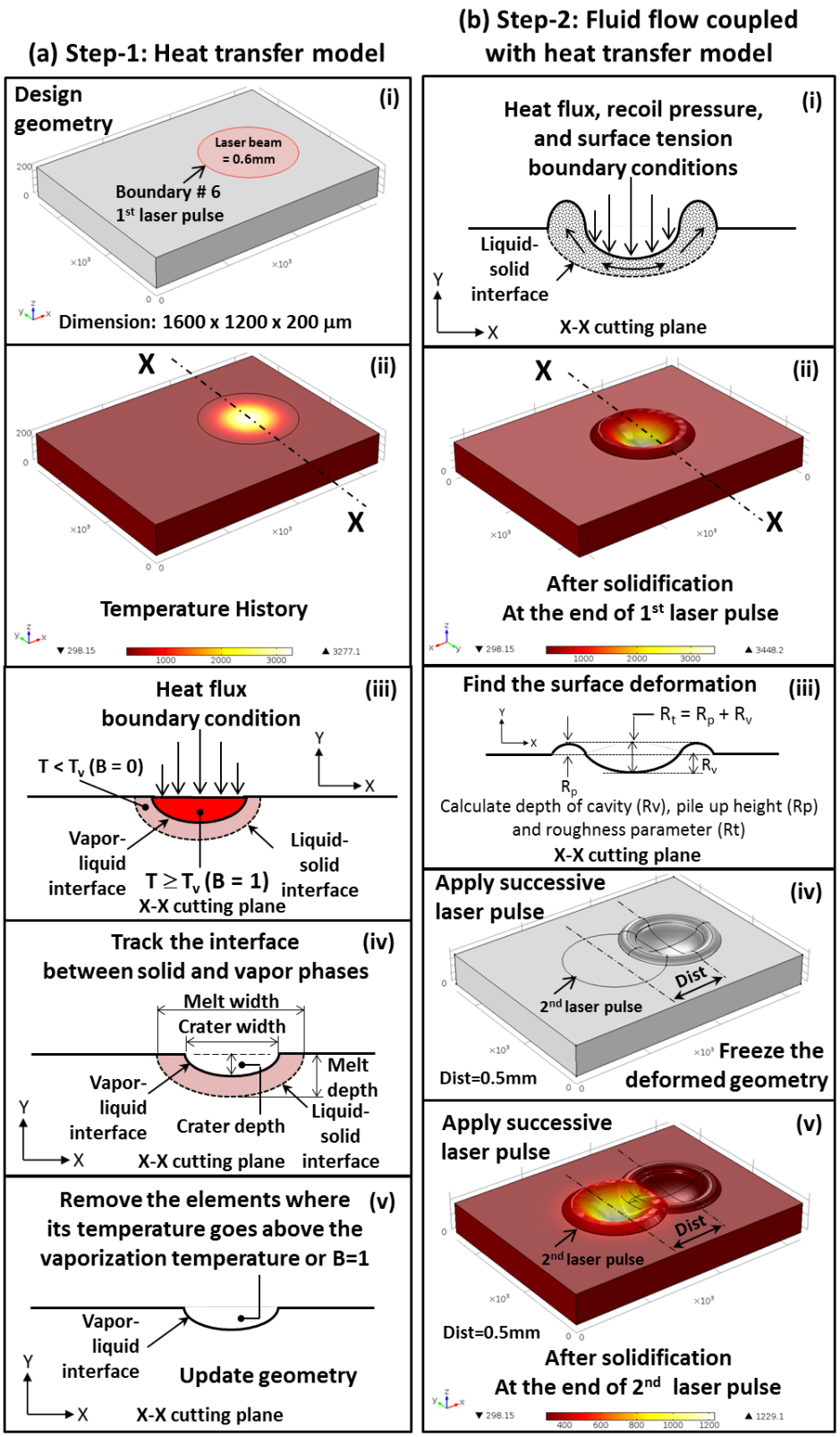

Figure 2.10 Two-step modeling approach to predict the surface profile (topography) during PM moving laser beam 2D laser machining conditions

Table 4 Laser machining parameters for moving laser beam 2D laser machining

Parameter	**Nomenclature**	**Value (units)**
Pulse energy	E_p	1 (J)
Pulse width	P_w	0.5 (ms)
Beam diameter	D	0.6 (mm)
Pulse rate or pulses per second	f	17, 20, 25, 34, 50,100 pulses
Scanning speed	Vin	10 (mm/s)
Distance between two pulses	Dist = Vin/f	0.6, 0.5, 0.4, 0.3, 0.2, 0.1 (mm) respectively
Average laser energy density per pulse	$E_d = \frac{E_p}{\left(\frac{\pi}{4}D^2\right)}$	3.5×10^6 (J/m^2)
Effective laser energy density per second	$E_{eff} = \frac{E_p}{\left(\frac{\pi}{4}D^2\right)} \times f$	6.02×10^7, 7.08×10^7, 8.85×10^7, 12.0×10^7, 17.7×10^7, 35.4×10^7 (J/m^2) respectively
Time gap between two pulses	tg = 1/f	0.06, 0.05, 0.04, 0.03, 0.02, 0.01 (s)

2.4.1 Step-1 Computational Model

Step-1 of the model was only incorporating the heat transfer to facilitate the prediction of crater geometry. The initial three-dimensional geometry, dimension: 1600×1200×200μm, for the Step-1 of the model is shown in the Figure 2.10a (i). The convective cooling and surface to ambient radiation boundary conditions was assigned to the whole geometry and insulated boundary condition is allocated to the bottom surface of the geometry. However, Boundary 6, shown in Figure 2.10a (i), is subjected to boundary heat source, convective cooling, and surface to ambient radiation boundary conditions, which are expressed by the Eq. (21). Here, ∇ is the Del operator, represented by the nabla symbol.

$$-k\nabla T = -\varphi P_g + h[T - T_i] + \varepsilon\sigma[T^4 - T_i^4] \quad (21)$$

$$\text{where, } \varphi = 1 \text{ for } 0 \le t \le P_w, \text{ and } \varphi = 0 \text{ for } t \ge P_w$$

The present model uses the Gaussian distribution for the laser energy and therefore the average laser power density assigned to the boundary heat source as expressed by the Eq. (22). Here, A is the absorptivity parameter [27], x_r and y_r are the reference point to represents the center of the laser beam along x- and y-axis, respectively.

$$P_g = A\left[\frac{E_p}{P_w\left(\frac{\pi}{4}D^2\right)}\right]\cdot\exp\left[-\left(\frac{(x-x_r)^2}{2\emptyset^2}\right)\right]\cdot\exp\left[-\left(\frac{(y-y_r)^2}{2\emptyset^2}\right)\right] \quad (22)$$

$$\text{where, } \varphi = 1 \text{ for } 0 \le t \le P_w, \text{and } \varphi = 0 \text{ for } t \ge P_w$$

Level-set method developed by Sussman at el. [53], as shown by Eqs. (3-5), was adopted in the Step-1 of the model to distinguish the interface between vapor-liquid and removed the elements where it temperature goes above the vaporization temperature, which is shown in Figure 2.10a (iii to v). In this way, Level-set method helps to track the interfaces between two phases and estimates the phase fraction of a corresponding phase. Also, this method helps to evaluate the evaporated material lost besides the prediction of melt pool dimensions. Based on this findings, the updated geometry was evaluated, which plays an important role in defining the much more effective multiphysics boundary conditions for Step-2, shown in Figure 2.10a (v).

2.4.2 Step-2 Computational Model

The Step-2 considered the updated geometry as a starting geometry. In Step-2, it can be noticed that the shape of boundary 6, Figure 2.10a (i), which is flat in Step-1, but due to the loss of material it had changed to concave shape, Figure 2.10b (i). Therefore, the updated surface geometry of boundary 6 accurately defines the normal and tangential boundary conditions (boundary heat source, recoil pressure, and surface tension). Although, the phase change phenomena and heat transfer physics adopted in Step-2 are identical as Step-1, but the change of

shape of Boundary 6 strongly influences the corresponding boundary conditions, and hence the generation of typical surface roughness profile. Step-2 of the model was designed by incorporating the phase change kinetics and multiphysics (heat transfer and fluid flow) to calculate the surface deformation of melt pool by assigning the various boundary conditions for corresponding body (gravitational, Marangoni) and surface (recoil pressure, surface tensions) forces and to predict the final surface topography, shown in Figure 2.10b (i). The Boussinesq approximation [54,55] was adopted to assign the natural convection prompted by the buoyancy-driven flow and volume force to the whole updated geometry, which is as shown in Eq. (23). However in Step-2, recoil pressure (P_r) [28,30], expressed by Eq. (15), was also assigned to the Boundary 6 of updated geometry (Figure 2.10). Thus, the Boundary 6 of updated geometry was subjected to surface tension forces, recoil pressure, heat flux, surface-to-ambient radiation, and natural convective cooling boundary conditions.

$$\text{Volume Force} = \rho g \alpha (T - T_m) \tag{23}$$

The Marangoni convection is nothing but the fluid flow driven by the surface tension [54]. The Step-2 of the model incorporated the Marangoni convection forces (at the liquid-air interface) by assigning the shear stress proportionate to the temperature gradient $\left(\frac{\partial T}{\partial x} \text{or } \frac{\partial T}{\partial x}\right)$ on the corresponding surface [54], which was done by incorporating the weak terms, shown by Eq. (24-25), to enforce the velocity in x-, y-direction and supersedes the slip boundary condition[54].

$$\text{test}(u) * \left[\frac{\partial \gamma}{\partial T}\frac{\partial T}{\partial x}\right] \tag{24}$$

$$\text{test}(v) * \left[\frac{\partial \gamma}{\partial T}\frac{\partial T}{\partial y}\right] \tag{25}$$

By following the step-1 and -2 of the model and corresponding boundary conditions, the surface topography on the completion of first laser pulse was predicted (Rp, Rv, and Rt), shown

in Figure 2.10b (ii and iii). This two-step modeling cycle was again used to predict the surface topography for the successive laser pulses. The predicted surface topography at the end of first laser pulse was considered as an initial geometry for Step-1, shown in Figure 2.10b (iv). The distance between two pulses (lateral overlap), Dist (=Vin/F), was calculated and the heat transfer boundary conditions for step-1 was assigned to predict the geometry that estimated the material loss due to evaporation during the application of second laser pulse, shown in Figure 2.10b (iv). The resultant geometry was considered as an initial geometry for Step-2 that incorporated the fluid flow and heat transfer boundary conditions to calculate the surface topography, which is systematically shown in Figure 2.10b (v). Likewise, these multi-step modeling stages were followed for consecutive laser pulses until laser beam travels preset/desired distance. However, the present model only considered the effect of two consecutive laser pulses on the evolving surface roughness/topography.

2.5 Three-dimensional (3D) Laser Machining

In extension of the previous work (2D laser machining - moving laser beam), the present efforts investigated the influence of moving PM laser beam (multiple laser pulses, lateral as well as transverse overlap, stationary workpiece,) on the surface topography (finish/roughness) during laser machining via integrated computational and experimental approach to mimic/replicate the generic milling process. In the present effort, computational model with three-dimensional geometry was developed by using the COMSOL^{TM} multiphysics finite-element software and then validated with the experimental observations. The only major difference between the present model and the previous 2D laser machining model is the incorporation of transverse overlap.

The 3D laser machining is specifically intended to process large area. However, due to the smaller beam diameter (0.6mm), the laser machining of large area is carried out by successive laser racks with specific transverse overlap (or distance between two laser tracks). In 3D laser machining, the laser beam is moving continuously along the principle axis (Z-axis) with predefined lateral overlap (Dist = Vin/f) to complete each laser track (1st laser track - A, laser beam is ON in forward direction) (Figure 2.11). Once the laser beam completes the laser track, the laser beam turned OFF and the focusing head or workpiece is indexed by the preset transverse overlap distance followed by the consecutive laser rack (2nd laser rack- B, laser beam is ON in forward direction) (Figure 2.11). Similarly, this cycle continuously runs for 'n' number of laser tracks to machine the large surface area.

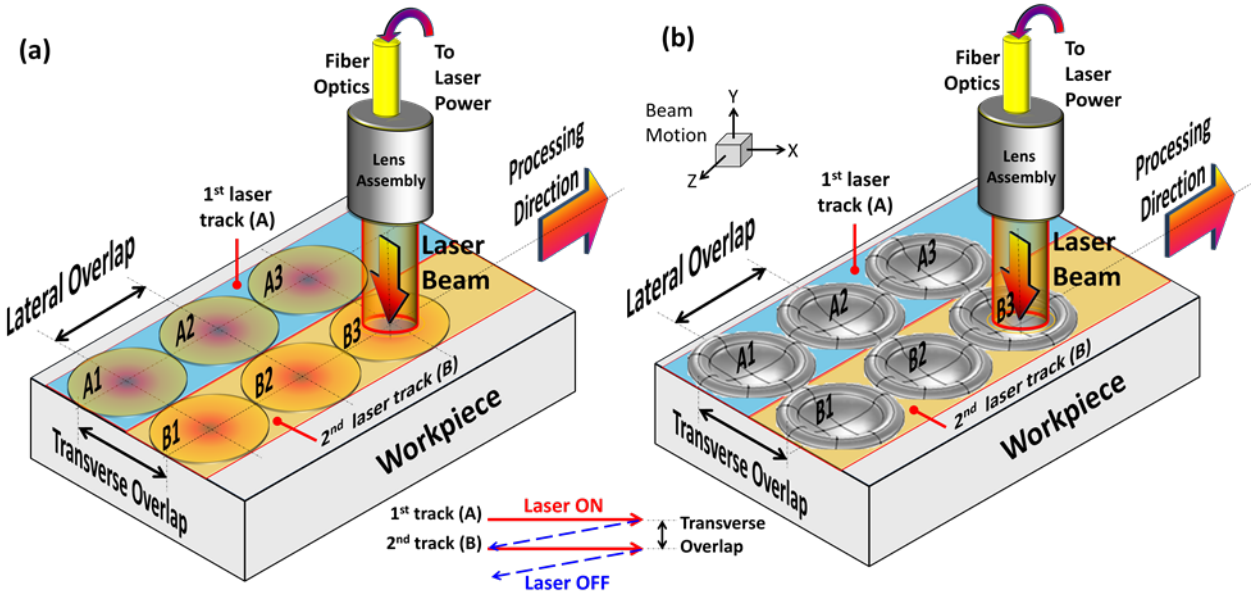

Figure 2.11Three-dimensional laser machining

In 3D laser machining, lateral overlap (Dist = Vin/f) and transverse overlap can be varied by the laser parameters. Therefore, the selection of laser machining conditions is very crucial and it plays a significant role in resultant surface roughness. Hence, three-dimensional (3D)

computational model was developed to precisely simulate the moving PM laser machining process with incorporating the lateral and transverse overlap. The higher modeling accuracy was achieved by accurately incorporating all the involving phenomena via multiphysics (heat transfer and computational fluid dynamics) modeling approach and temperature-dependent material properties (Table 1, Figure 2.7, and Eqs. (2, 17-18)) , which can facilities the evaluation of the temperature field, cooling rates, and velocity of molten material that in turn influence the generation of surface topography under the application of various laser machining conditions. The present computation model is same as used for the 2D laser machining that uses the multi-step modeling methodology (Figure 2.9 and 2.10) to predict the evolving surface topography under the 3D laser machining conditions that are basically carried out by the application of multiple laser pulses and moving laser beam with lateral and transverse overlap. The laser-machining parameters used for model and experiments are enumerated in Table 5.

Table 5 Laser machining parameters for 3D laser machining

Parameter	**Nomenclature**	**Value (units)**
Pulse energy	E_p	1 (J)
Pulse width	P_w	0.5 (ms)
Beam diameter	D	0.6 (mm)
Pulse rate or pulses per second	f	17, 20, 25, 34, 50,100 pulses
Scanning speed	Vin	10 (mm/s)
Lateral overlap or distance between two laser pulses	Dist = Vin/f	0.6, 0.5, 0.4, 0.3, 0.2, 0.1 (mm) respectively
Transverse overlap or distance between two laser tracks	O_T	0.6, 0.5, 0.4, 0.3, 0.2, 0.1 (mm) respectively
Average laser energy density per pulse	$E_d = \frac{E_p}{\left(\frac{\pi}{4}D^2\right)}$	3.5×10^6 (J/m^2)
Effective laser energy density per second	$E_{eff} = \frac{E_p}{\left(\frac{\pi}{4}D^2\right)} \times f$	6.02×10^7, 7.08×10^7, 8.85×10^7, 12.0×10^7, 17.7×10^7, 35.4×10^7 (J/m^2) respectively
Time gap between two pulses	tg = 1/f	0.06, 0.05, 0.04, 0.03, 0.02, 0.01 (s)

2.6 Thermal Stresses

Laser machining technique have emerged as an innovative tool to effectively machines the hard and brittle structural ceramics in complex shapes. On the other hand, during laser machining of structural ceramics (e.g. alumina - higher melting temperatures and lower thermal conductivity), the localized nature of heating (small laser beam and laser-material interaction zone) creates the larger temperature gradient (sudden temperature rise and fall) that in turn induces the thermal stresses in the small laser-material interaction zone and heat affected zone (HAZ). A considerable amount of work was carried out to investigate the thermal stresses during laser machining of structural ceramics and its detrimental effects on the machining quality [57-60]. Most of this works revealed that the large thermal gradient caused by the localized laser generate the thermal stresses, which is generally higher than the fractural and/or yield strength of structural ceramics is sufficient enough to nucleate micro-cracks that grows by subsequent heating/cooling cycle. Therefore, to improve the quality of laser machining it is very important to evaluate the magnitude and location of thermal stresses during laser machining.

In light of this, the present work utilizes the computational approach (to save time and cost) to evaluate the thermal stresses during laser machining. The temperature history predicted from the previously discussed multi-step multiphysics computational model for one-, two-, and three-dimensional laser machining (section 2.2 to 2.5) are further used to estimate the thermal stresses. The magnitude of thermal stresses (σ_T) for alumina (obtained from Advalue Technology Inc., Tucson, AZ) can be calculated from the Eq.(26) [16].

$$\sigma_T = \frac{E\alpha}{1-\vartheta}(T_i - T) \tag{25}$$

Here, E is the elastic modulus (375 GPa), α is the coefficient of thermal expansion (8.4×10^6 1/K), ν is the Poisson's ratio (0.22), T_i is the initial temperature, and T is the

instantaneous temperature [61]. It was anticipated that the thermal stresses higher than the fractural strength of the alumina (379 GPa) [61] can lead to the micro-cracks during laser machining. An environmental scanning electron microscope (ESEM, FEI Quanta 200) was utilized to obtain the micrographs of the top-view of the laser machined alumina. The main objective of using SEM in the present work is to capture the micro-cracks on the surface of the laser machined alumina during various laser machining conditions.

CHAPTER 3

EXPERIMENTAL METHODS[3]

3.1 Sample Preparation and Laser Machining

An alumina slab (90×65×6mm^3) with purity of 99.6 wt. % (<0.1% SiO_2, <0.05% Fe_2O_3, and < 0.1 % R_2O all in wt.%) obtained from Advalue Technology Inc., Tucson, AZ was used in this study. The samples were then machined using JK 701 Lumonics pulsed Nd:YAG (1.064 μm wavelength) fiber optic laser system. The laser machining parameters used for 1D (single and multiple laser pulses), 2D and 3D laser machining are presented in Table 1, 3, 4, and 5, respectively. The layout of laser-machined alumina for various processing conditions is schematically shown in Figure 3.1.

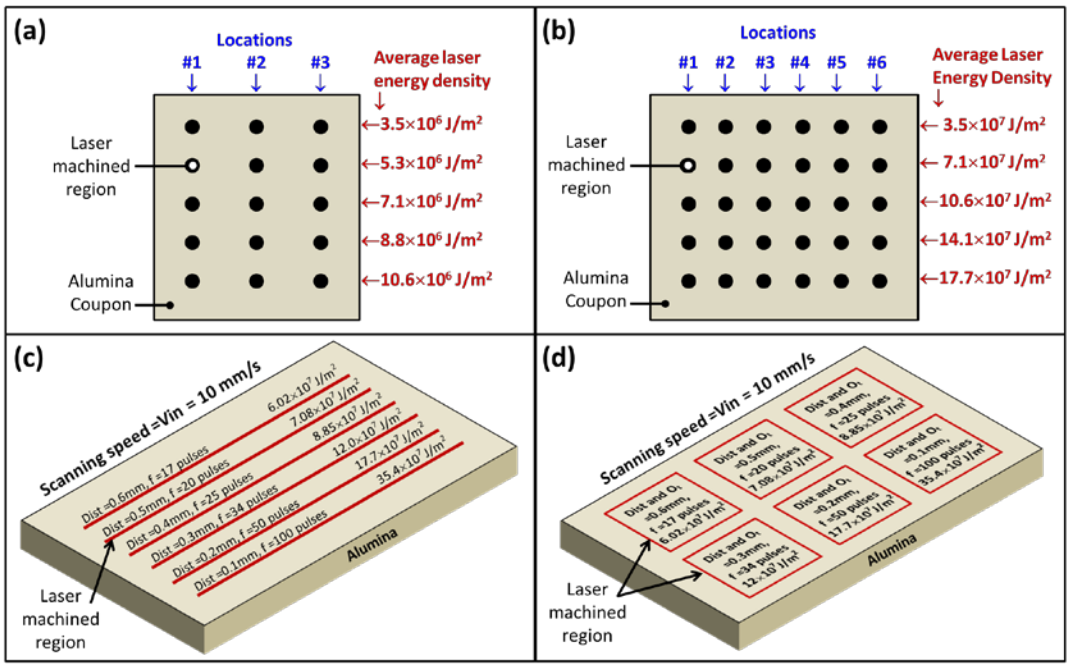

Figure 3.1 Schematic of laser-machined alumina

[3] Parts of this chapter have been previously published, either in part or in full, from (1) Hitesh D. Vora, Soundarapandian Santhanakrishnan, Sandip P. Harimkar, Sandra K.S. Boetcher, Narendra B. Dahotre, *Journal of European Ceramic Society* 2012, 32 (16), 4205–4218 with permission from Elsevier, and (2) Hitesh D. Vora, Soundarapandian Santhanakrishnan, Sandip P. Harimkar, Sandra K.S. Boetcher, Narendra B. Dahotre, *International Journal of Advanced Manufacturing Technology* 2013, 68(1), 69-83 with permission from Springer

3.2 Surface Profile Measurements

There are various standard surface profile (topography) measurement techniques available such as contact stylus profilometer, contact-less optical profilometer, Scanning Electron Microscopy (SEM), and Atomic Force Microscopy (AFM). However, the selection of appropriate measurement techniques is vital since it predominantly depends on the magnitude and periodicity of surface profiles. In the contact stylus tracing method, the main requirement for proper measurement is the size of the stylus tip and stem, which should be smaller than the roughness of the surface. On the contrary, the no-contact optical profilometer measurement is independent of the size of the stem and the stylus tip. Conversely, for measuring the surface topography using SEM requires the cross-sectioning of the sample. However, it is extremely difficult to cross-section the ceramic sample (alumina) of finer dimensions (diameter and depth < 1000 μm) exactly across the center of the crater for accurate measurement. In addition, piled-up and re-solidified alumina around the crater lip tends to get removed during cross-sectioning and subsequent polishing thereby leading to inaccurate surface profile (roughness) measurements. In light of this, the optical profilometer proved to be the most appropriate tool to conduct the topographic measurements on the surface and within the crater without missing the details of irregular pile-up and re-solidified layer around the crater lip. Hence, the NANOVEA® optical profilometer , model PS50, with an optical pen of 3.5 mm was employed in the present work to measure the surface roughness parameters of the evolving surface topography/profile (Figure 3.2).

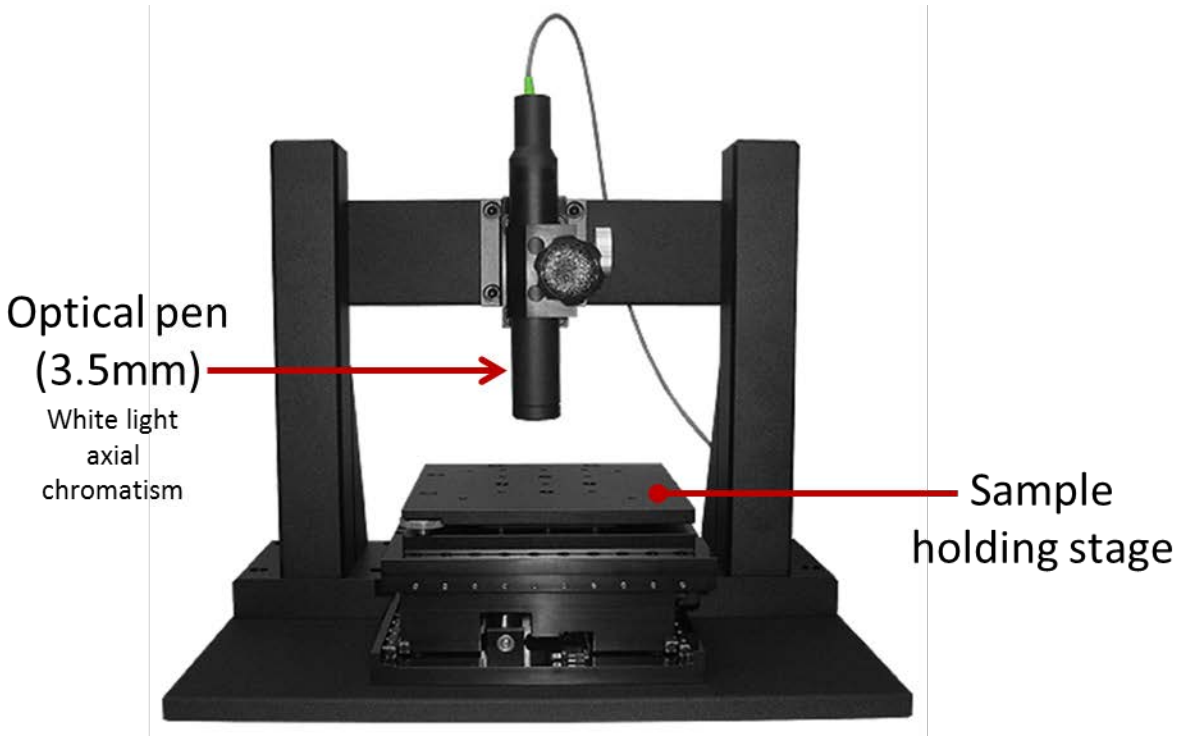

Figure 3.2 NANOVEA® optical profilometer (model PS50) with an optical pen of 3.5 mm. Courtesy: NANOVEA® Inc.

3.2.1 One-dimensional (1D) Laser Machining - Single and Multiple Laser Pulse

The NANOVEA® optical profilometer (model PS50) with an optical pen of 3.5 mm at the scan speed of 1 μm/s is used for the surface profile measurements. The ISO 25178-2:2012 (Geometric Product Specifications– Surface texture: areal) specifications was followed during the surface profile measurements. In addition, the ISO 4287:1996 standards are utilized for the line profile measurement on the previously scanned surfaces to measure the amplitude parameters, R_p (maximum peak height of the line profile in μm), R_v (maximum valley depth of the line profile in μm, and R_t (maximum height of the line profile in μm, $R_t = R_p + R_v$). The raw data obtained during the surface profile measurements using the optical profilometer is further post-processed by using the NANOVEA® 3D software. In addition, the standard post-processing procedure suggested by the inbuilt NANOVEA® template is followed. The spatial filtering

operator with a median denoising filter 3×3 is used to eliminate the outliers (bad points). The surface has been leveled by subtracting the least square plane from the whole surface area. Later, the median smoothing filter 7×7 was applied to filtered out the noise (micro-roughness) and improve the quality of the scanned surface profile. Moreover, the surface was split into its waviness and roughness component by using an Areal Gaussian filter with a cut-off of 0.25 mm. Finally the line-profile measurement was taken across the crater of the previously processed sample as schematically shown in Figure 3.3a. Thus, this procedure ensured the minimization or elimination of error in surface topography measurements. Further, a total of eight readings are taken for each processing condition (8 line-profile × 3 locations = 24 readings) in order to achieve higher accuracy in surface profile measurements. From each line profile measurement the roughness parameters R_p, R_v and R_t were evaluated (Figure 3.3b).

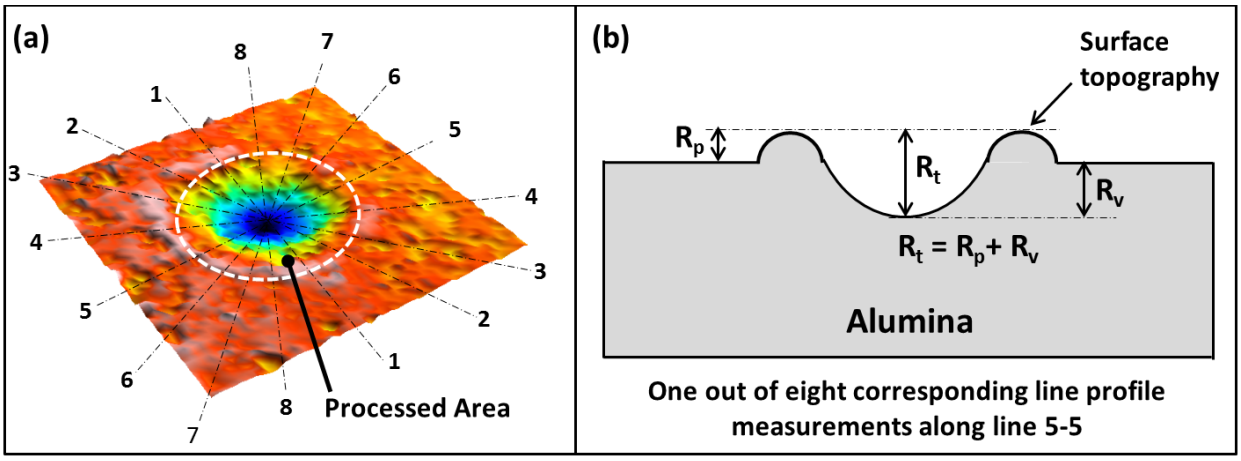

Figure 3.3 Surface profile measurement for 1D laser machining (a) tracks of line profile measurements, and (b) two-dimensional representation of line profile measurements along line 5-5 and corresponding roughness parameters

3.2.2 Two-dimensional (2D) Laser Machining

NANOVEA® optical profilometer (model PS50, 3.5mm optical pen, 1 μm/s scanning speed, 1.5×3mm^2 scanning area) was used for the surface profile (topography) measurements.

The amplitude parameters, Sp (highest peak height of the surface profile), Sv (highest valley depth), and Sz (maximum height of the surface profile, Sz = Sp + Sv) are evaluated by following the geometric product specifications for surface texture (areal, ISO 25178-2:2012). A NANOVEA® 3D software standard was utilized for the post-processing the raw data to obtained the amplitude parameters (Sp, Sv and Sz), which is as shown in Figure 3.4. Based on this data, the series of measurements along X-Z planes were overlaid (Figure 3.4b) to evaluate the mean profile (Figure 3.4c) as well as roughness parameters R_p, R_v and R_t. For each machining condition, a total of 5 surface profile measurements were taken to attain the statistically highest precision. Finally, the experimentally measured surface roughness values, (Sp, Sv and Sz), were used to validate the computational model of 2D laser machining.

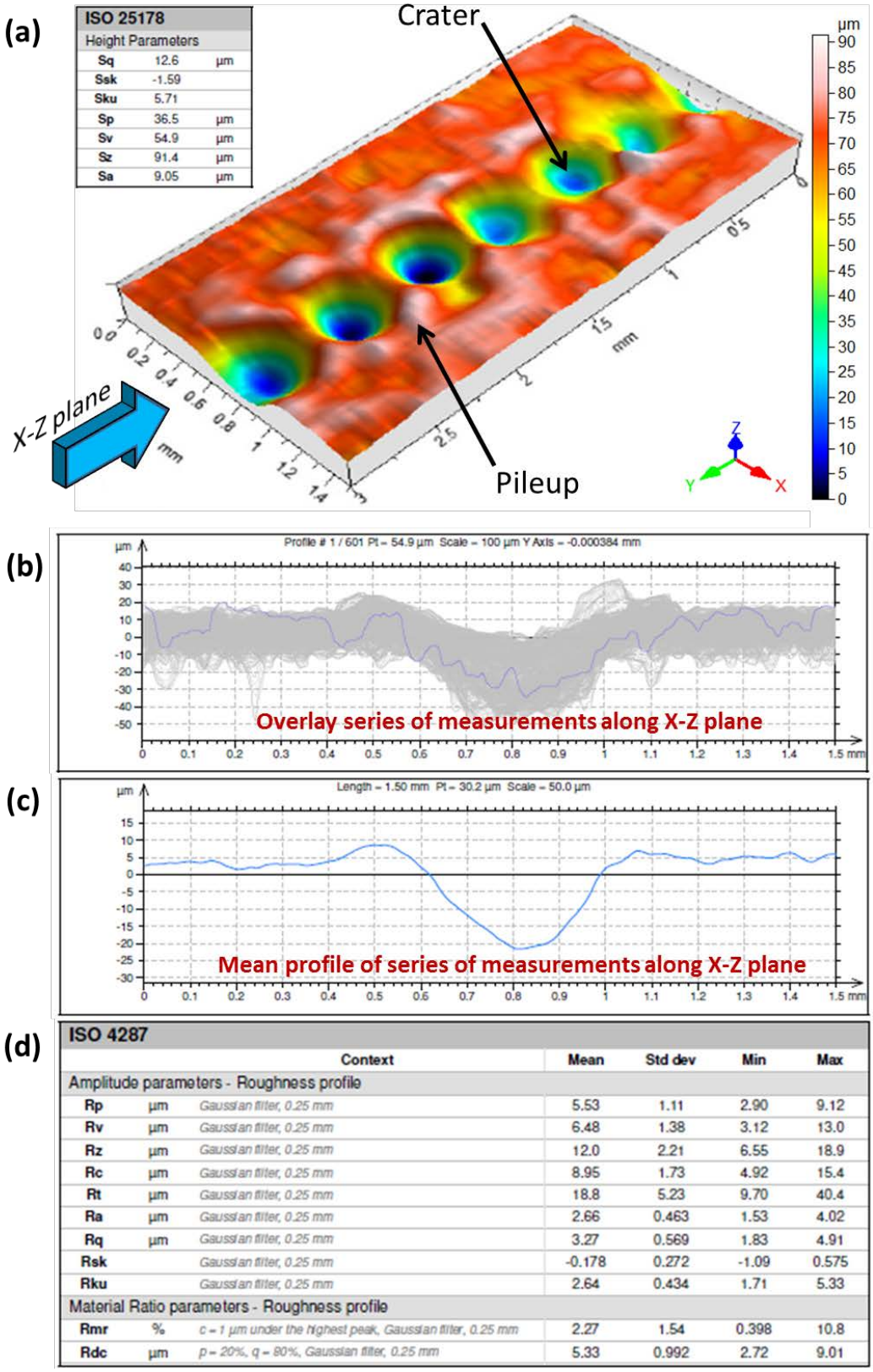

Figure 3.4 Schematic of surface profile measurements for 2D laser machining

3.2.3 Three-dimensional (3D) Laser Machining

NANOVEA® optical profilometer (model PS50, 3.5mm optical pen, 1 μm/s scanning speed, $5\times5mm^2$ scanning area) was used for the surface profile (topography) measurements. The amplitude parameters such as Sp (highest peak height), Sv (highest valley depth), and Sz (maximum height of the surface, Sz = Sp + Sv) are evaluated by following the geometric product specifications for surface texture (areal, ISO 25178-2:2012). A NANOVEA® 3D software standard was utilized for the post-processing the raw data to obtained the amplitude parameters (Sp, Sv and Sz), which is as shown in Figure 3.5. The series of measurements along X-Z planes obtained from the previous data were overlapped (Figure 3.5b) in order to estimate the mean surface profile (Figure 3.5c) and corresponding roughness parameters R_p, R_v and R_t. To achieve higher statistical accuracy, a total of 5 surface profile measurements were taken for each machining condition. Finally, the experimentally measured surface roughness values, (Sp, Sv and Sz) and (R_t, R_p, and R_v), were used to validate the computational model of 3D laser machining.

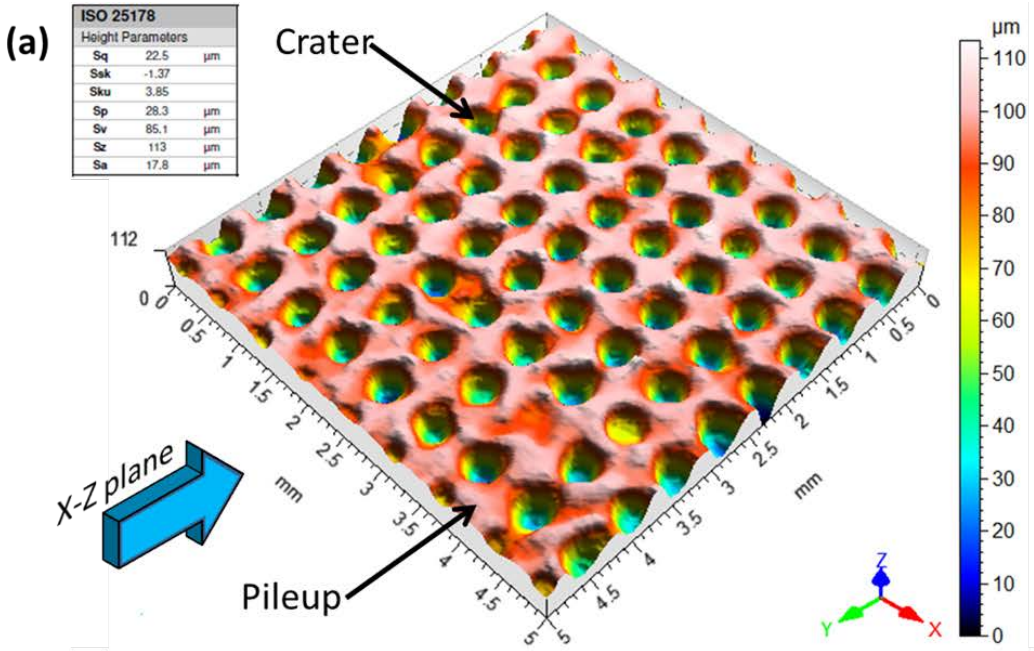

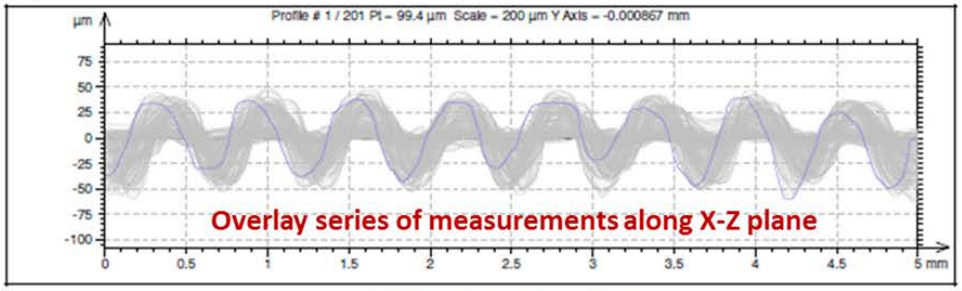

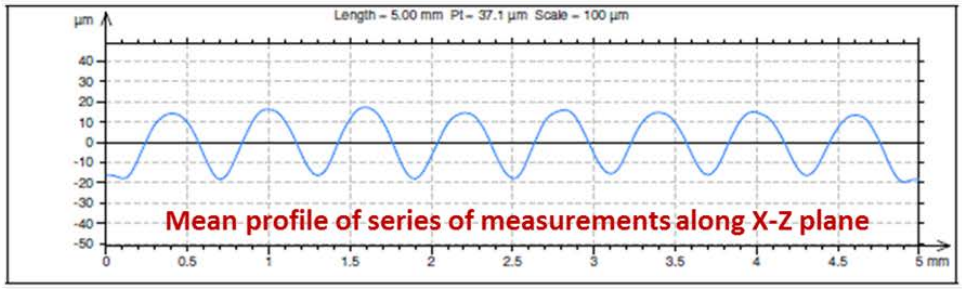

(d)

ISO 4287

Context			Mean	Std dev	Min	Max
Amplitude parameters - Roughness profile						
Rp	µm	*Gaussian filter, 0.8 mm*	12.0	7.89	2.08	27.8
Rv	µm	*Gaussian filter, 0.8 mm*	17.5	10.7	2.56	33.7
Rz	µm	*Gaussian filter, 0.8 mm*	29.5	18.4	4.83	59.8
Rc	µm	*Gaussian filter, 0.8 mm*	28.0	18.3	3.94	58.1
Rt	µm	*Gaussian filter, 0.8 mm*	36.6	19.9	6.52	68.0
Ra	µm	*Gaussian filter, 0.8 mm*	8.83	6.31	1.14	20.7
Rq	µm	*Gaussian filter, 0.8 mm*	9.96	6.86	1.37	22.5
Rsk		*Gaussian filter, 0.8 mm*	-0.425	0.264	-1.07	0.473
Rku		*Gaussian filter, 0.8 mm*	2.11	0.456	1.36	3.25
Material Ratio parameters - Roughness profile						
Rmr	%	*c = 1 µm under the highest peak, Gaussian filter, 0.8 mm*	2.56	1.76	0.592	13.0
Rdc	µm	*p = 20%, q = 80%, Gaussian filter, 0.8 mm*	20.4	15.5	2.46	50.3

Figure 3.5 Schematic of surface profile measurements for 3D laser machining

CHAPTER 4

RESULTS AND DISCUSSIONS[4]

4.1 One-dimensional (1D) Laser Machining - Single Laser Pulse

4.1.1 Evaporative Material Removal

The temperature history extracted from boundary 6 (Figure 2.2d) for various single-pulse laser machining conditions is presented in Figure 4.1a. The rise and drop of the temperature is due to rapid heating by the high laser intensities, self-quenching by the bulk mass material, and due to the losses by external natural convection and radiation that in turn control the different physical phenomena taking place in the material. From the heating and cooling temperature histories for various laser machining conditions (Figure 4.1a), corresponding heating and cooling rates were computed (Figure 4.1b). The laser is ON for one pulse duration ($P_w = 0.5 \times 10^{-3}$ s) for the heating cycle (Figure 4.1a), and the temperature rise during this time followed by the cooling cycle. For lowest energy density (3.5×10^6 J/m^2) the peak temperature is close to the vaporization temperature (3273 K). Also, the material remains at this temperature for short time duration (< 0.01×10^{-3} s). Hence, only the material from shallow depth reaches temperature above vaporization. Therefore, in this case the material loss due to ablation is small which results in a shallow crater depth. It can be observed that the peak temperature increases with increasing laser pulse energy density leading to creation of higher crater depth.

[4] Parts of this chapter have been previously published, either in part or in full, from (1) Hitesh D. Vora, Soundarapandian Santhanakrishnan, Sandip P. Harimkar, Sandra K.S. Boetcher, Narendra B. Dahotre, *Journal of European Ceramic Society* 2012, 32 (16), 4205–4218 with permission from Elsevier, and (2) Hitesh D. Vora, Soundarapandian Santhanakrishnan, Sandip P. Harimkar, Sandra K.S. Boetcher, Narendra B. Dahotre, *International Journal of Advanced Manufacturing Technology* 2013, 68(1), 69-83 with permission from Springer

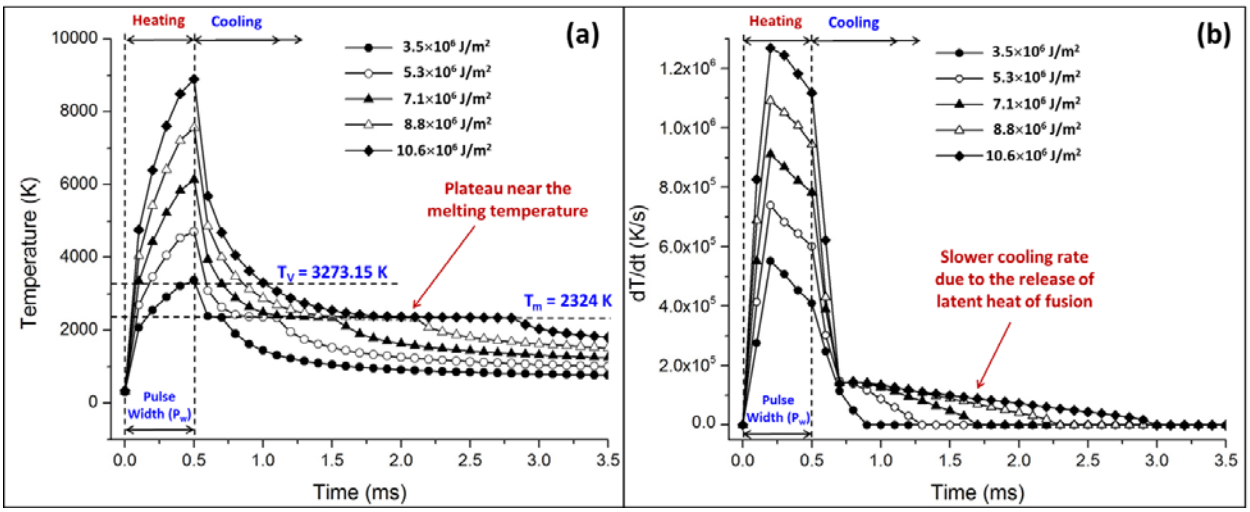

Figure 4.1 Computational plots for various laser energy density machining conditions (a) temperature vs. time plot, (b) rate of heating/cooling with respect to time

Due to the localized nature of laser beam, the surface temperature in confined volume is instantaneously increased. However, the remaining surrounding material acts as a heat sink which subsequently decreases the temperature along with the heat loss due to radiation and convective cooling. As a cumulative result, the material experiences higher cooling rates (dT/dt > 10^5 K/s) (Figure 4.1b). For the processing condition of highest energy density (10.6×10^6 J/m^2), initially during heating cycle (< 0.2×10^{-3} s), the material experienced the rapid increase in temperature (from room temperature to 4759 K, dT/dt = 4461 K / 0.1×10^{-3} s) which led to higher heating rate (1.27×10^6 K/s). During the same heating cycle between 0.2ms to 0.3ms, the temperature increases gradually from 4759 K to 6399 K. Due to the gradual increase in temperature (from 4759 K to 6399 K, dT/dt = 1640 K / 0.1×10^{-3} s) the heating rate slightly drops (< 1.24×10^6 K/s) compared to initial heating rates. Similarly during the same heating cycle, the gradual increase in temperature causing the steady drop in the heating rate until the laser is switched off (1.22×10^6 K/s at 0.5×10^{-3} s). During cooling cycle (after 0.5×10^{-3} s), the cooling rate drops drastically due to self-quenching along with heat losses by external natural convection

and radiation. When the solidification (change from liquid phase to solid phase) starts, the temperature decreases quickly towards room temperature. During this cooling cycle, the heat consumed or released by phase change affects the temperature history (Figure 4.1a) which is evidenced by the plateau near the melting temperature (2324 K) and the change in cooling rate (Figure 4.1b).

Even for lowest energy density machining condition (3.5×10^6 J/m^2) used in the current study (Figure 4.1a), the highest temperature reached is near or above vaporization temperature (3273 K). Hence, to realize the effects of laser machining in the most pronounced manner, the processing condition with highest energy density machining (10.6×10^6 J/m^2) is selected for detailed analysis (Figure 4.2). Under the action of higher energy density, the surface rapidly rises to melting temperature. This melting range expands through heat conduction. In this case, the laser energy density is high enough for the surface to start vaporizing before a significant melting depth in molten material is formed. Although, vaporization is preferred for high material removal rate, it results in considerably rough surface profile. In contrast, melting with minimal vaporization provides better surface finish with lower material removal rate. For highest energy density machining condition (10.6×10^6 J/m^2), the material is in liquid phase for short duration of time (t_1 to t_2 time, ~0.06×10^{-3} s) than the vapor phase (t_2 to t_4 time,~1.1×10^{-3} s) indicating the dominance of laser ablation (Figure 4.2a). This results in higher material loss due to evaporation. From this observation it is assumed that for the lower energy densities ($< 3.5\times10^6$ J/m^2) used in the present work, the dominance of material removal by laser ablation decreased with decrease in energy densities and hence decrease in material loss by vaporization.

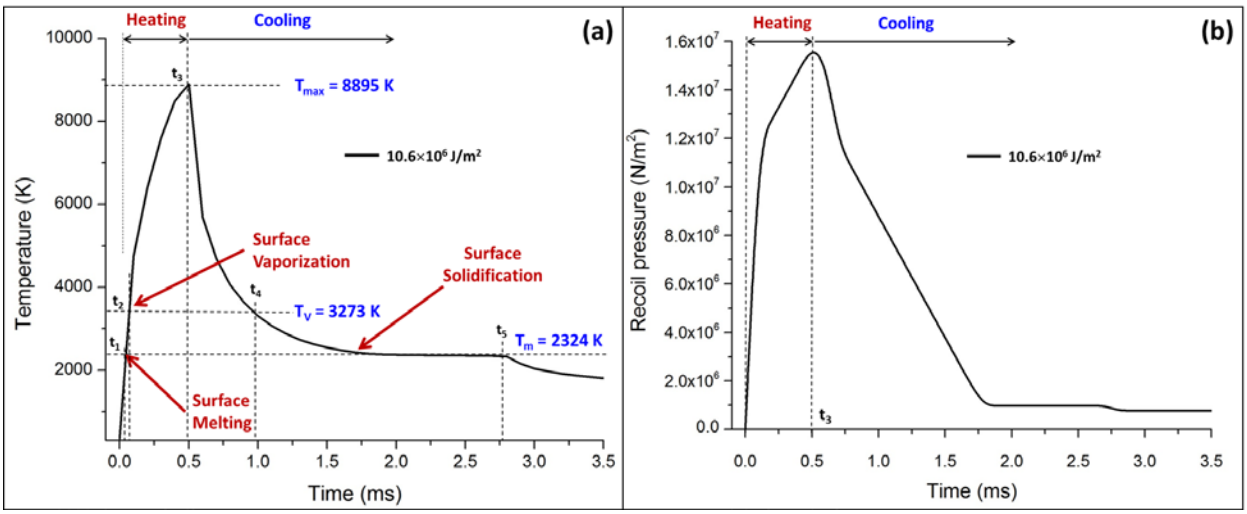

Figure 4.2 Computational plots for highest laser energy density machining condition (10.6×10^6 J/m^2) (a) temperature vs. time (b) recoil pressure vs. time

For laser pulse durations longer than microseconds, hydrodynamic ablation is dominating component over pure vaporization ablation [5,15,16]. The commonly used pulse width for laser machining is 0.1 to 10×10^{-3} s (in the present case it is 0.5×10^{-3} s), and this time scale allows the surface to heat to the vaporization temperature and remain there for some time [1,2]. When vaporization occurs, it generates a recoil pressure shield around the molten material [43,46,47]. Also there exists strong temperature gradients in the molten material; usually the center is hotter than the outer because of the Gaussian profile of the laser beam. The recoil pressure and temperature gradient drives the molten material towards the edge of the laser beam impact. In the present computational model, the recoil pressure strongly depends on the applied laser energy density. Within the set of laser energy densities employed in the present work, as the laser energy density increases, the surface temperature increases which in turn increase the recoil pressure. For the higher laser energy density (10.6×10^6 J/m^2), (Figure 4.2a), the surface temperature and corresponding recoil pressure is higher at the end of the laser pulse (Figure 4.2b). In this case, since the material remains at this elevated temperature for about 0.5ms, a significant amount of

material is ablated. In the computational model, the recoil pressure is calculated and the corresponding boundary condition was applied only when the surface temperature is above the vaporization temperature ($T \geq T_v$).

The interface between vapor and liquid phases was distinguished using the level-set method described earlier by Eq. (3-5). From this method, the crater depth and width are calculated (Figure 4.3) in order to incorporate the material loss due to evaporation. The present model also predicts the melt depth and width (Figure 4.3) that in turn predicts the molten material available to undergo surface deformation during laser machining to generate the final surface topography. It can be noticed that the crater depth and width as well as melt depth and width increase with the increase in average energy density.

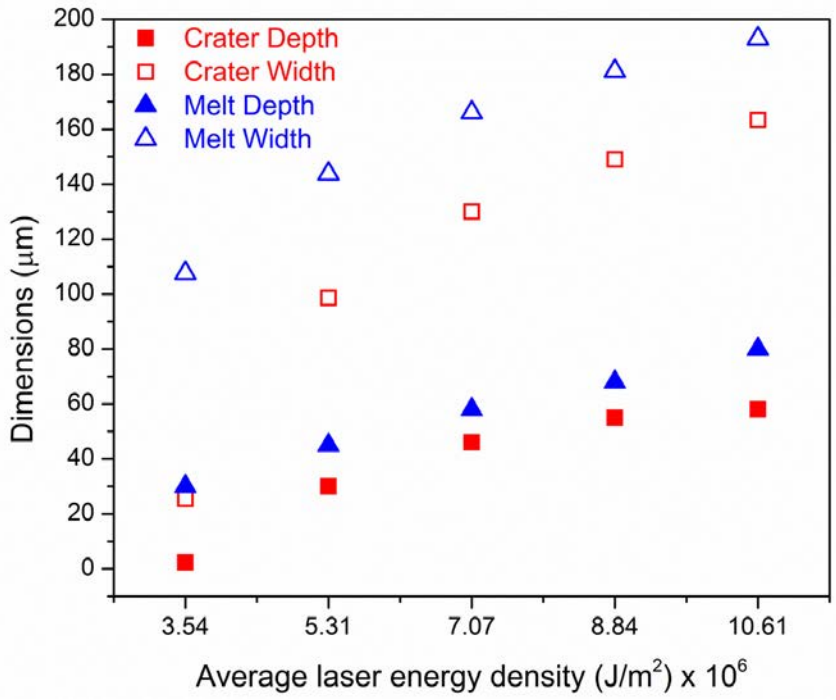

Figure 4.3 Predicted crater depth and width, and melt depth and width for various laser energy density machining conditions at the end of laser pulse (0.5ms)

4.1.2 Surface Profile Prediction

The multi-phase fluid flow coupled with heat transfer and phase change kinetics was considered in the Step-2. The new surface geometry (creation of crater) was designed to include the material loss due to evaporation based on the data provided by the Step-1 heat transfer and phase change kinetics model. Due to material lost by evaporation (laser ablation), the new boundary 6 in Step-2 model is in concave shape which was originally flat in Step-1 model (Figure 2.4). Thus, the new surface geometry precisely defines the fluid flow and heat transfer boundary conditions in Step-2 model. Although, Step-2 model adopted the same scheme as in Step-1 model for heat transfer and phase change boundary conditions, the change in surface geometry bore tremendous influence on fluid flow, heat transfer, and phase change boundary conditions and hence on the evolution of final surface topography.

For the laser beams of higher energy densities and shorter pulse duration, the resulting recoil pressure may be high enough to prompt the shock waves. This generates the hydrodynamic melt motion on the liquid melt pool underneath. As a consequence, the liquid metal ejected out from the melt pool. However, at the end of the heating cycle, the liquid metal tends to return to its original place due to the gravitational and surface tension forces. Simultaneously, the liquid material tends to solidify rapidly due to the effects of self-quenching and higher cooling rates during this dynamic process. The tangential stresses generated by the surface tension forces tend to provide a profile to the solidified material. Thus, a distinct surface topography (roughness) is generated on the laser machined surface (Figure 2.4).

The present fluid flow model was designed to evaluate the hydrodynamic melt motion and its subsequent effect by calculating the velocity of the molten material subjected to heating and cooling cycles. The recoil pressure is principally the temperature dependent phenomenon

and plays a significant role along with surface tension forces in driving the molten material during the laser machining. As the temperature increases with increase in energy density (Figure 4.1a), a higher recoil pressure leads to the higher velocity of the molten material (Figure 4.4). It was previously noticed (Figure 4.3) that the maximum temperature and corresponding maximum recoil pressure for the highest laser energy density machining condition (10.6×10^{6} J/m^{2}) existed at the end of the heating cycle (0.5×10^{-3} s). This suggests that the velocity is high at the end of the laser pulse (Figure 4.4).

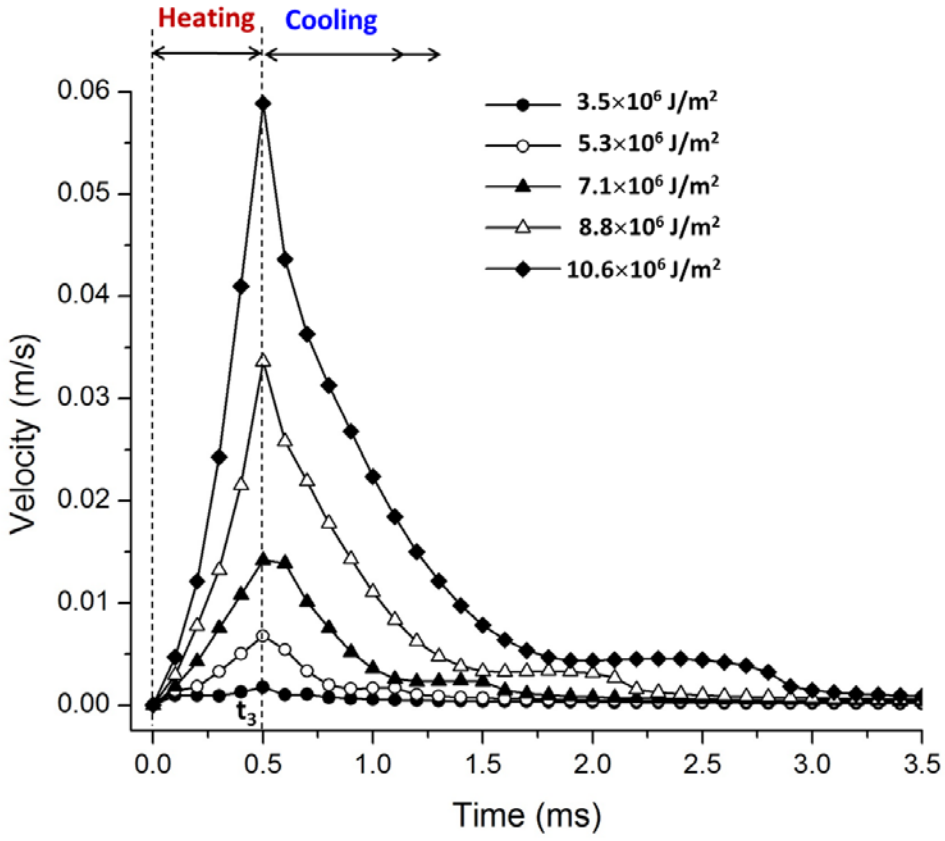

Figure 4.4 The velocity profile for various laser energy density machining conditions

When the surface temperature was above the vaporization temperature the recoil pressure was high and a dominating factor to drive (displace) the molten material. On the contrary, the surface tension and gravitational forces were dominating factors to displace the molten material

when the surface temperature dropped below the vaporization temperature. As the material remained above the melting temperature (2324 K) for longer duration (~3×10^{-3} s) even after the end of heating cycle (Figure 4.1a) (when the recoil pressure was not active), the surface tension continued to cause surface deformation (Figure 4.4) and this combined with longer time of solidification (~3×10^{-3} s) allowed the liquid material to displace towards the edges of the molten pool thereby creating a crater with crown of piled up and re-solidified material. Thus a pronounced surface topography was generated through the combination of these physical processes on the laser machined surface.

The computationally predicted surface deformation plots in cross-section for various laser machining conditions are presented in Figure 4.5a. The present computational model assumed the piled-up and/or re-solidified material was symmetric around the plane X-X (Figure 2.2 and Figure 4.5b). In this case, the predicted results can be revolved around the axis (z-axis, Figure 4.5c) of crater (along the circumference) and hence a uniform ring like structure formed along the crater lip as illustrated in Figure 4.5d. Under this assumption the cross-sectional view (Figure 4.5a) facilitated the measurement of surface roughness parameters, R_p (maximum peak height of the line profile in μm), R_v (maximum valley depth of the line profile in μm, and R_t (maximum height of the line profile in μm, $R_t = R_p + R_v$). It was previously noticed that, increased average laser energy density increased in-process vaporization and subsequent material removal; recoil pressure, and corresponding velocity of the molten material. The material lost due to ablation increased the crater depth, while the strong velocity gradient created by the recoil pressure increased the liquid pile-up. Both of these effects considerably increased the overall surface roughness of the laser machined surface and suggested that the surface roughness values increased with the increase in average energy density.

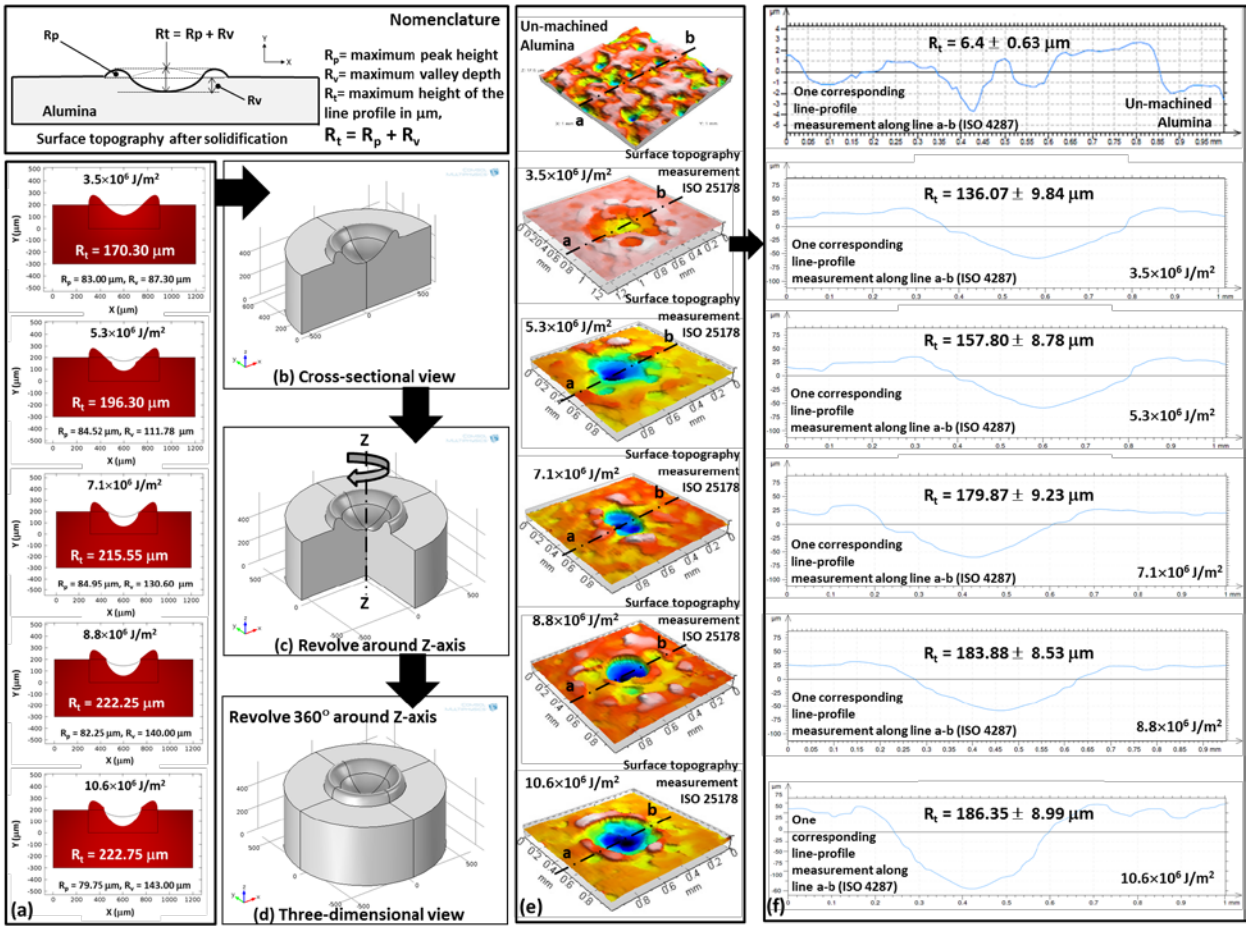

Figure 4.5 Computationally predicted and experimentally measured Surface topography (line profiles). (a) Computationally predicted surface topography, (b) cross-sectional view of predicted surface topography, (c) predicted profile revolved around Z-axis, (d) three-dimensional view of predicted surface topography, (e) experimentally measured surface topography of un-machined and laser machined alumina, and (f) corresponding line profile measurement along line X-X

4.1.3 Validation of Computational Model - 1D Laser Machining (Single Laser Pulse)

The computationally predicted and experimentally measured surface topography (profiles) for various laser energy density machining conditions are presented in Figure 4.5. The cross-sectional view (Figure 4.5a) of the computationally predicted surface topography facilitates to measure the surface roughness parameters R_p, R_v and R_t. The contact-less optical profilometer was employed to measure the surface topography of laser processed coupons under various laser energy density machining conditions (Figure 4.5e). The line-profile measurement (8 line-profile

× 3 locations = 24 readings for each processing conditions) was carried out on each processing condition (Figure 4.5f) and average value was utilized to validate the computational results. It was observed that the surface roughness increases with the increase in average energy density. Although similar trends were observed for this relationship determined by both the computational model and the experimental observations, the difference between them is in the range of 16-20% (Table 6). Such difference can be attributed to several factors including but not limited to the adaption of various literature suggested boundary conditions and temperature dependent material properties in the computational model.

Table 6 Computationally predicted and experimentally measured surface roughness for 1D (single laser pulse) laser machining conditions

Pulse energy	**Average energy density**	**Predicted R_t**	**Measured $R_t \pm$ standard deviation**	**Difference**
(J)	(J/m^2)	(μm)	(μm)	(%)
1.0 J	3.5×10^6	170.30	136.07 ± 9.84	20.09
1.5 J	5.3×10^6	196.30	157.80 ± 8.78	19.61
2.0 J	7.1×10^6	215.55	179.87 ± 9.23	16.55
2.5 J	8.8×10^6	222.25	183.88 ± 8.53	17.26
3.0 J	10.6×10^6	222.75	186.35 ± 8.99	16.34

The present computational model, considered the thermo-physical properties such as thermal conductivity, density, heat capacity, absorptivity, viscosity, and surface tension coefficient can affect the size (width and depth) of the melt pool. In addition, the variation of these thermo-physical properties could play a critical role in generating the hydrodynamic melt motion of the liquid metal during the simulation. In addition, the shape of the crater was also continuously changing during the laser processing that can change the angle of incidence of the incoming laser beam. Thus, the absorbance of the laser energy changed drastically that can cause the variation in surface temperature and subsequently the temperature dependent material

properties. Hence, the difference between computational and experimental results can be narrow down by inserting the more accurate thermo-physical properties in the computational model. On the contrary, as mentioned earlier the in-situ measurement of thermo-physical properties is a very challenging task due to high temperature, very short time duration, and very small volume of interaction and hence very limited data is presently available in the literature. In light to this, further work is underway to minimize the difference between the computational model and the experimental observations.

4.2 One-dimensional (1D) Laser Machining - Multiple Laser Pulses

4.2.1 Prediction of Material Loss

From Step-1, the temperature history for various laser machining conditions is extracted from the boundary 6 (Figure 4.6a). Due to higher laser energy density ($> 3.5\times10^7$ J/m^2) and the localized nature of the laser beam, the surface temperature in a confined volume quickly rises. Self-quenching and heat losses due to external natural convective cooling and radiation cause the drop in temperature. Both the increase and decrease of the temperature controls the different physical phenomena taking place in the material (heat conduction, melting, and vaporization). During one-dimensional multiple pulse laser machining, the temperature rises when the laser is ON for time duration of 0.5 ms (P_w) for each laser pulse, followed by the temperature drop during the laser OFF time ([1/f] - P_w). Based on the pulse rate (f = 10, 20, 30, 40, 50), the laser is turned ON again for a second pulse (for duration of pulse width, P_w = 0.5 ms) which increases the surface temperature. Likewise, the pulses are continuously delivered every 1/f second until the end of the laser cycle at 1s causes the sequential rise and drop of temperature. In the present

study, each individual laser pulse has constant laser pulse energy (1 J) and laser ON time (P_w = 0.5 ms).

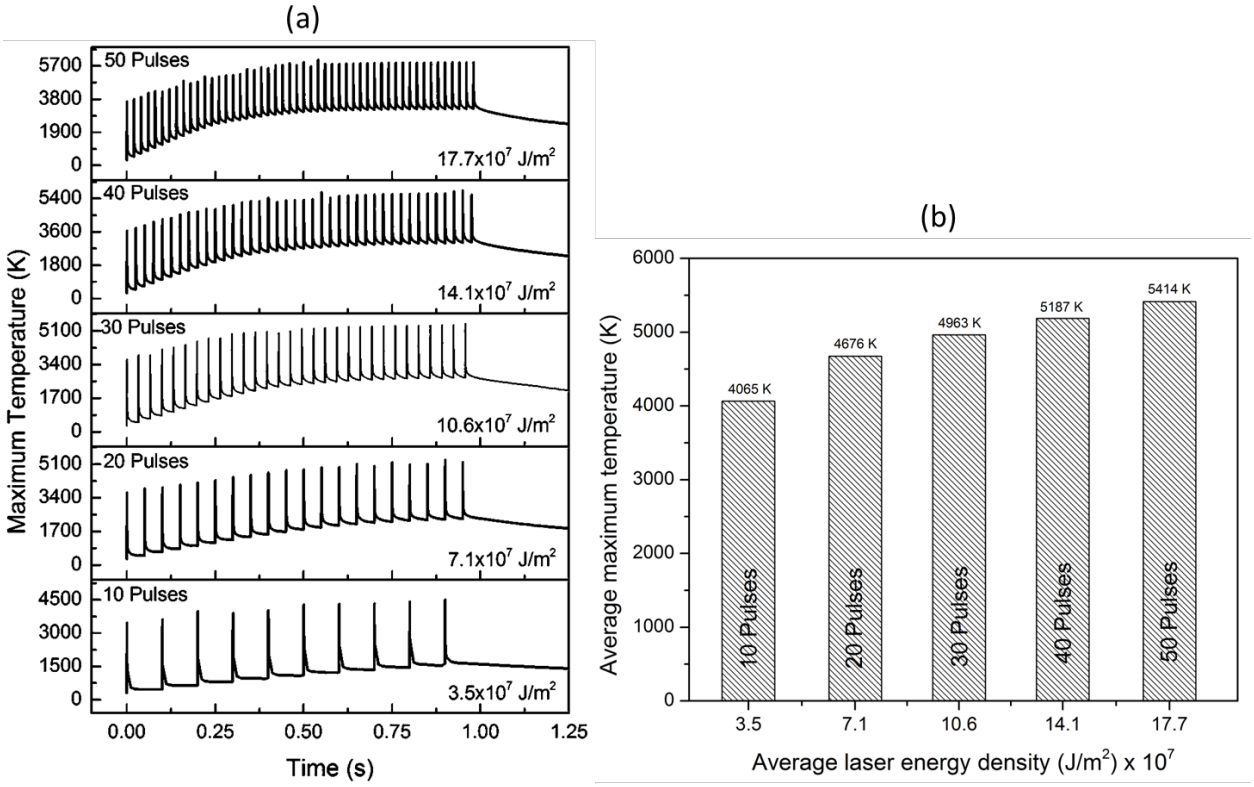

Figure 4.6 Computational plots (a) maximum temperature as function of time, and (b) average maximum temperature as function of average laser energy density

Due to the heat accumulation by the repetition of multiple laser pulses (Figure 2(b)), the maximum surface temperature gradually increases with increase in number of laser pulses (Figure 4.6a). But, above a certain average laser energy density (> 7.1×10^7 J/m^2), the material experiences the state where the heat losses (natural convective cooling and radiation) are balanced by the given heat input (absorbed laser energy) and do not show substantial rise or drop of the surface temperature (Figure 4.6a). However, the average laser energy density increases with increase in pulse rate which in turn increases the surface temperature (Figure 4.6a). The average maximum temperature for all laser machining conditions are plotted to analyze the

increase in surface temperature more accurately (Figure 4.6b). It is also observed that the average surface temperature increases with increase in pulse rate (or average laser energy density). Even for lowest average laser energy density (3.5×10^7 J/m^2) used in the current study (Figure 4.6b), the average maximum temperature (4065 K) is considerably higher than vaporization temperature (3273 K) indicating the higher material loss due to evaporation.

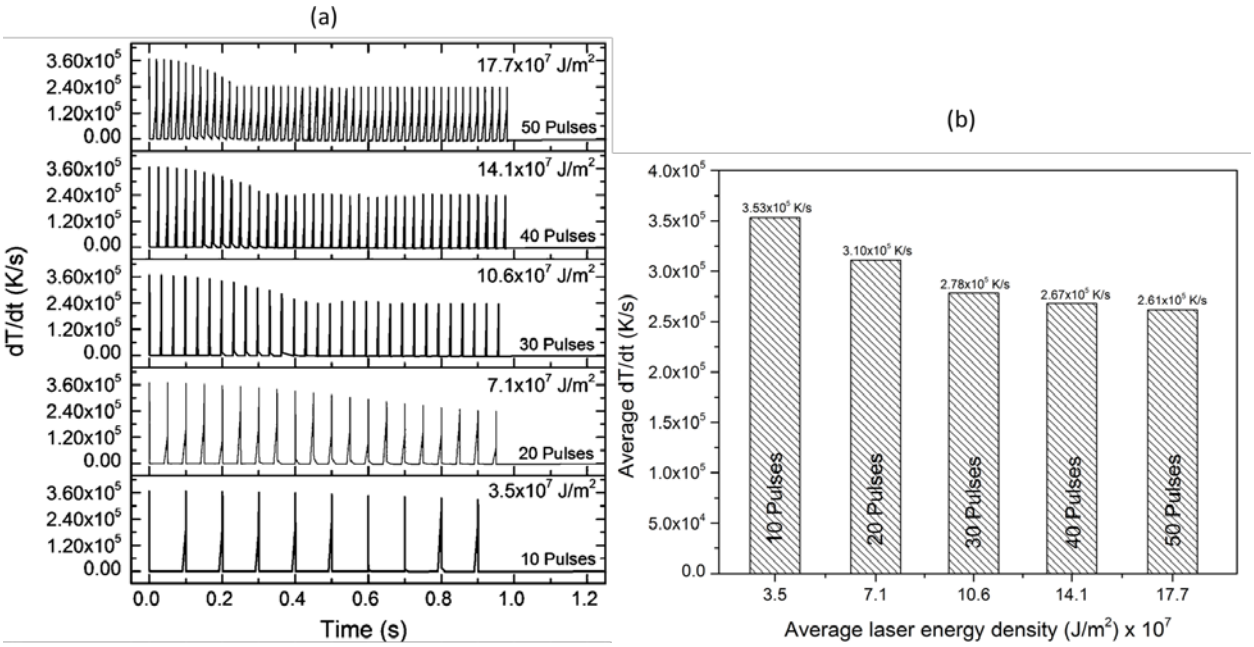

Figure 4.7 Computational plots (a) rate of heating/cooling (dT/dt) as function of time, and (b) average dT/dt as function of average laser energy density

Due to the rapid increase and decrease of surface temperature (Figure 4.6a), the material experiences the higher heating and cooling rates (dT/dt) during the laser machining. Furthermore, due to repetition of multiple laser pulses on the alumina surface, the material initially experiences a sudden increase in temperature which is evidenced by the initial higher heating/cooling rates (Figure 4.7a). However, once the bulk material attains the saturation state, the further increases in temperature in subsequent laser pulses is not as high as in the initial stage and caused the gradual drop in heating/cooling rates until the laser is switched off. As a result, the heating/cooling rate decreases with increase in number of pulses for all laser machining

conditions (Figure 4.7a). The average value of heating/cooling rate is calculated to represent the corresponding value of heating/cooling rate for each machining condition (Figure 4.7b). It can be observed that the average heating/cooling rate decreases with increase in average laser energy density (or pulse rate) for all laser machining conditions (Figure 4.7b). Furthermore, it is noticed that as the pulse rate increases the material remains in the liquid phase for longer time and the surface deforms continuously during this time.

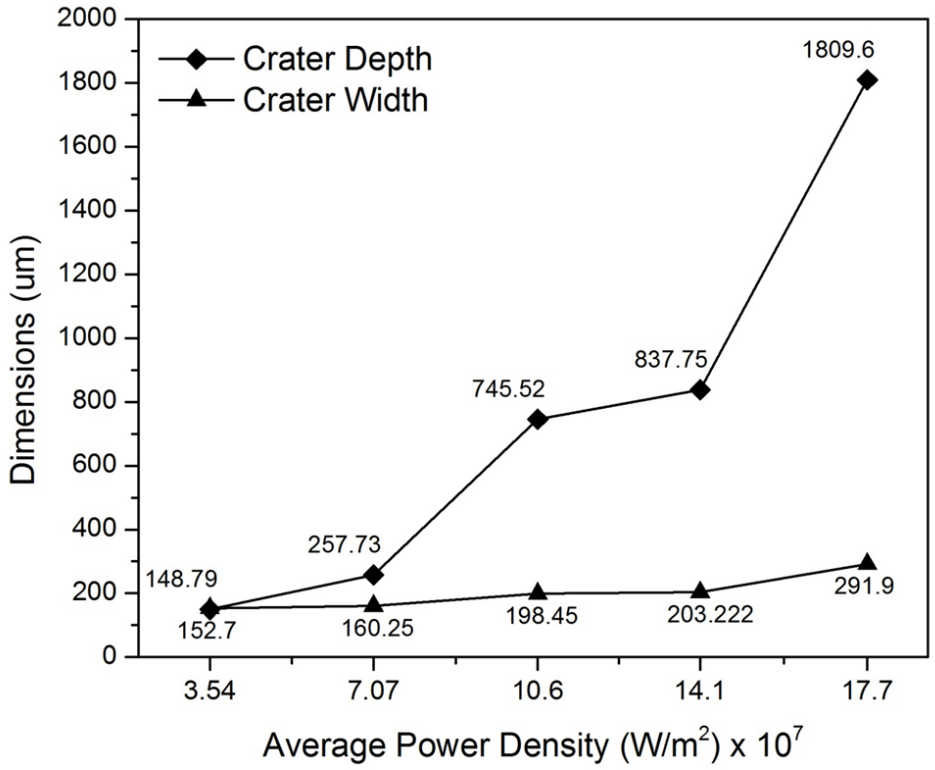

Figure 4.8 Measured crater depth and width for various laser machining conditions

The level-set method is used to predict the crater depth and width for various laser machining conditions. The crater depth and width increases with the increase in average laser energy density or pulse rate (Figure 4.8). In present work, the energy distribution of laser beam is in Gaussian, i.e. the laser energy is highest at the center of the beam and it gradually reduces as going towards the edges of the laser beam. Therefore, the surface temperature is higher at the

center of the laser beam compared to the edge. As a result, the material experiences preferential heat conduction. Hence, the penetration of heat inside the material normal to the top surface is higher than the lateral direction, causing the higher crater depth compared to crater width (Figure 4.8). During the repetition of multiple laser pulse, the material experiences a sequential loss of material due to evaporation. This material lost also increases with increase in number of laser pulses, which directly contributes in increasing the crater depth. From this data the updated geometry was then created and utilized in Step-2.

4.2.2 Prediction of Surface Topography

The fluid flow coupled with heat transfer and phase change kinetics is incorporated in Step-2. Based on the dimension of crater depth and width provided by Step-1 heat transfer model, the new geometry (creation of crater) is designed in Step-2 to include the material loss due to evaporation. It can be noticed that the shape of boundary 6 (Figure 2.4) in Step-1 is flat but due to the loss of material it had changed to concave shape. Thus, the new surface geometry of boundary 6 precisely defines the normal and tangential boundary conditions (heat flux, recoil pressure, and surface tension). Even though, the heat transfer and phase change boundary conditions adopted in Step-2 are same as Step-1 but the change in surface geometry of boundary 6 (Figure 2.4) strongly influences the corresponding boundary conditions of fluid flow, heat transfer, and phase change kinetics and hence the generation of final surface profile.

The recoil pressure, surface tension, and gravitational forces are the important factors to generate the hydrodynamic melt pool motion. During the heating cycle, when the surface temperature is above the vaporization temperature, the recoil pressure is the dominating factor to drive the molten material out from the crater that further increases the crater depth as well as the

liquid pile-up. On the other hand, when the temperature drops below the vaporization temperature, surface tension and gravitational forces lead the motion of the molten material and therefore liquid metal tends to return to its original place. At the end of the heating cycle, the higher cooling rates and self-quenching simultaneously affect the solidifying liquid material and the tangential stresses generated by the surface tension forces; provide the profile to the solidified material.

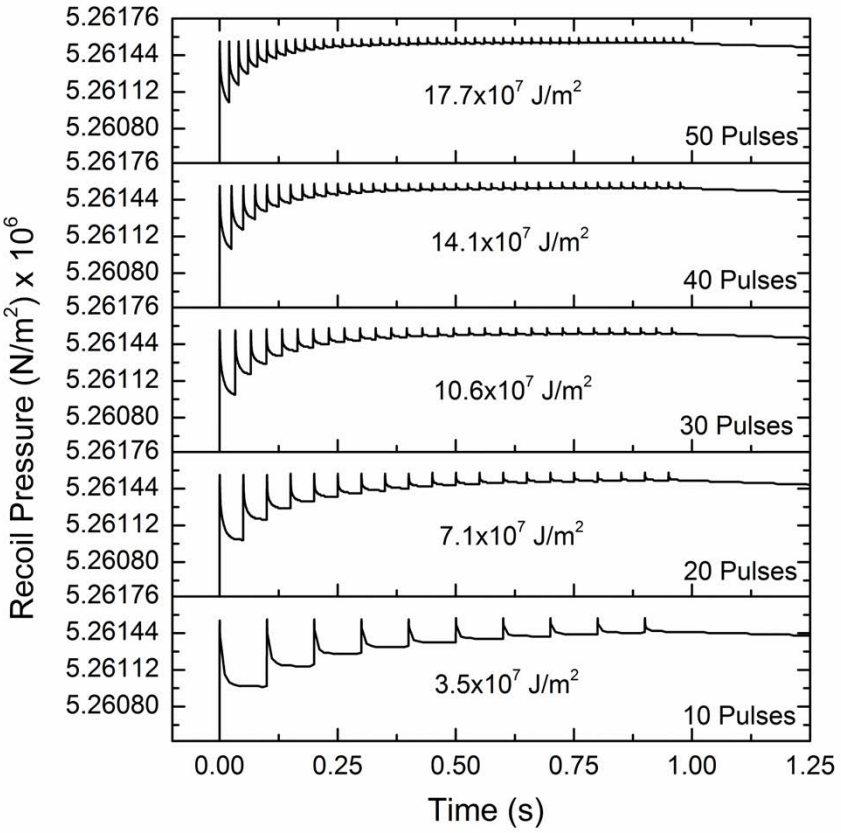

Figure 4.9 Effect of recoil pressure as function of time for various laser energy density machining conditions (only applied when $T \geq T_v$)

The recoil pressure strongly depends on average laser energy density and the instantaneous surface temperature (Eq. (15)) and hence its magnitude gradually increases with increase in average laser energy density and the instantaneous surface temperature (Figure 4.9).

The Figure 4.9 only shows the numerically calculated recoil pressure during various laser energy density machining conditions. However, in the computational model, the actual recoil pressure is only applied on the melt pool when the surface temperature reaches above the vaporization temperature. Once the material reaches the saturation state, the further increase in the number of pulses or average laser energy density does not alter the magnitude of recoil pressure (Figure 4.9). In addition, the depth of the crater increases drastically due to the increase in average laser energy density (or pulse rate) and recoil pressure. However, above a certain critical crater depth (~260 μm), the magnitude of recoil pressure is not enough to drive the molten material out of the crater even though the surface temperature is above the vaporization temperature. Here, the magnitude of surface tension and gravitational forces dominate over the higher recoil pressure causing the drop in velocity of molten material. Hence, net velocity of the molten material initially increases with increase in average laser energy density (3.5×10^7 J/m^2 and 5.3×10^7 J/m^2) (Figure 4.10).

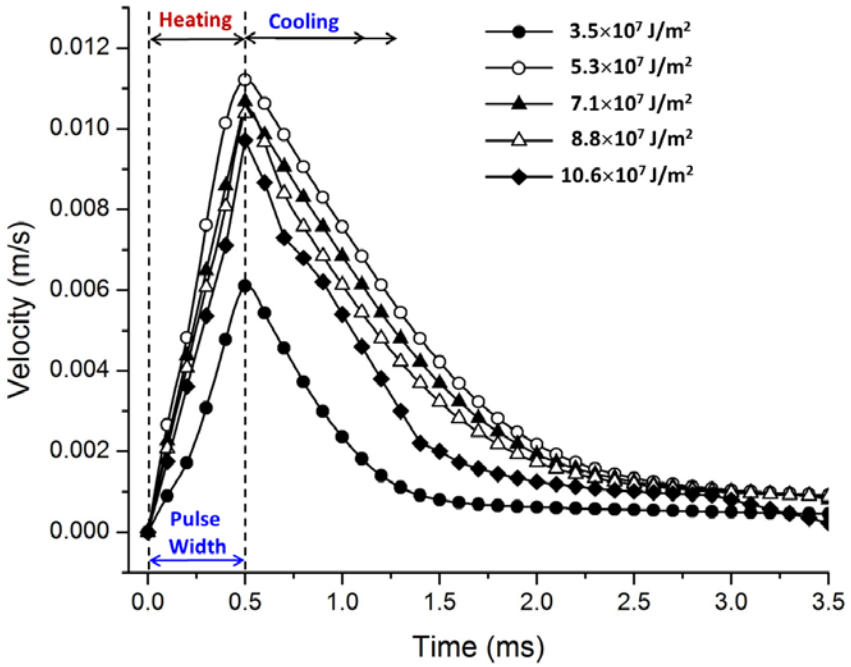

Figure 4.10 The velocity profile for various laser energy density machining conditions during the last laser pulse

However, after reaching a certain critical crater depth (~260 μm), net velocity of molten material drops down for further increase in average laser energy density (> 5.3×10^7 J/m^2). The velocity is high at the end of the laser on time due to the maximum temperature and corresponding maximum recoil pressure for all the average laser energy density machining conditions, existed at the end of the heating cycle (Figure 4.10). However, as the surface temperature continuously drops down immediately after the laser off time until the end of cycle (1s) it in turn causes the gradual drop in the velocity of the molten material.

The computationally predicted surface deformation plots in cross-section for various laser machining conditions are presented in Figure 4.11a. The present computational model assumes that the piled-up and/or re-solidified material is symmetric around the plane X-X (Figure 2.5 and Figure 4.11b). In this case, the predicted results are revolved around the axis (z-axis, Figure 4.11c) of crater (along the circumference) and hence a uniform ring like structure formed along the crater lip as illustrated in Figure 4.11d. Under this assumption, the cross-sectional view (Figure 4.11a) facilitates the measurement of the surface roughness parameters R_p, R_v and R_t. During the application of each laser pulse, the surface temperature of the material goes above the vaporization temperature leading to material loss due to evaporation. As the number of laser pulses increases, the material experiences material removal which increases the crater depth. In addition to this, the molten material expelled out by recoil pressure directly contributes to increasing the R_v value (Figure 4.11 and 4.12). Although the crater depth increases, the recoil pressure is not sufficient to eject the molten material out from the crater resulting in a decrease in the R_p value (Figure 4.11 and 4.12). Hence, after reaching a certain critical crater depth (~260 μm) the net velocity of the molten material decreases with increase in average laser energy density.

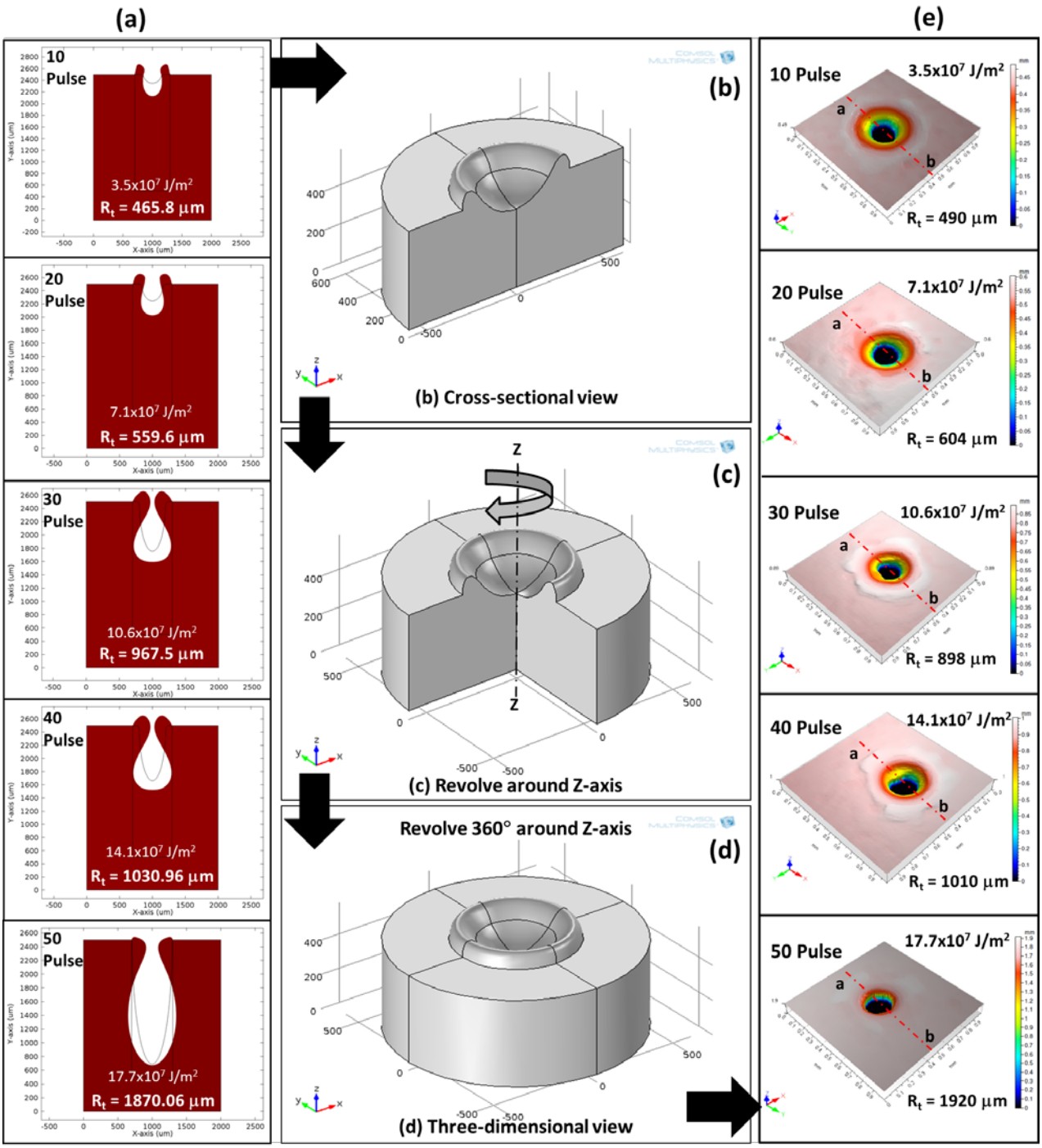

Figure 4.11 Computationally predicted and experimentally measured surface topography (profiles) (a) computationally predicted surface topography, (b) schematic cross-sectional view of predicted surface topography, (c) schematic of predicted surface profile revolved around Z-axis, (d) schematic three-dimensional view of predicted surface topography, and (e) experimentally measured surface topography (ISO 25178) and one out of eight corresponding line profile measurement along line a-b (ISO 4287)

On the contrary, a longer time necessary for solidification (~2-5 s) allows the expelled molten material to solidify on the inside wall of the crater (known as recast layer) without the possibility of returning to its original place which will reduce the pile-up height (R_p) (Figure 3.3b, 4.11, and 4.12). Thus, distinct tear-drop shape topography is generated on the wall of crater (Figure 4.11a). Among all laser machining conditions, the highest laser energy density machining condition (10.6×10^7 J/m^2) provides the largest crater depth (R_v = 1826.26 μm) with the least material pile-up (R_p = 43.8 μm) on the surface. This combination is responsible for the higher surface roughness (R_t = 1870.06 μm) for higher energy density.

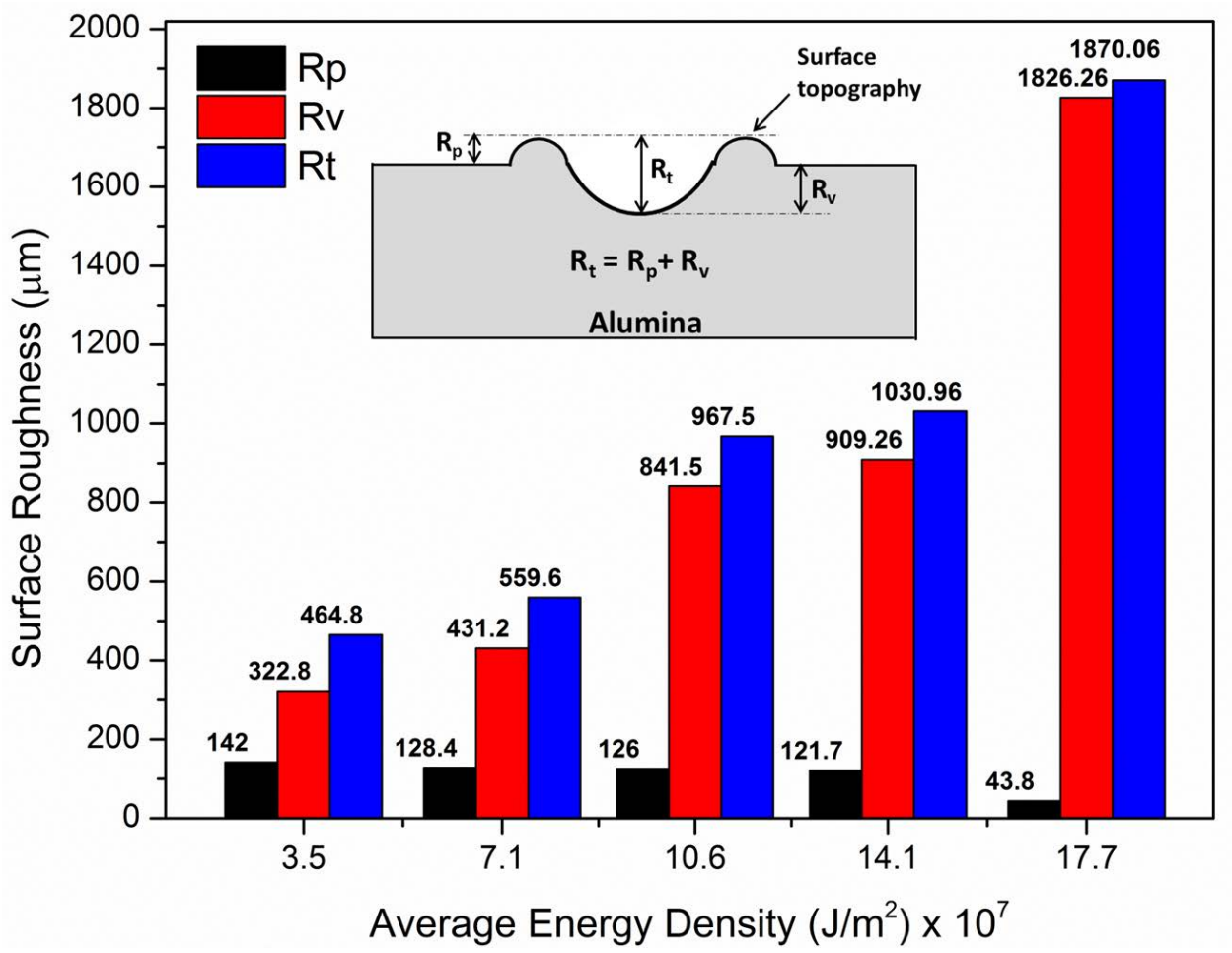

Figure 4.12 The change of surface roughness parameters for various average laser energy density machining conditions

4.2.3 Validation of Computational Model - 1D Laser Machining (Multiple Laser Pulses)

In order to validate the computational model, the computationally predicted and experimentally measured values of surface roughness for various laser machining conditions are summarized and presented in Table 7. It is observed that the surface roughness increases with the increase in average laser energy density. The difference between the computational model and the experimental observations are within the range of 2-8%, thereby strongly validating the computational model. The difference of computational results can be attributed to the adaptation of various literature suggested temperature dependent material properties [49,50,56] and boundary conditions [1,2,47,53,54].

Table 7 Computationally predicted and experimentally measured surface roughness for 1D (multiple laser pulses) laser machining conditions

Average Energy Density	**Laser pulses**	**Numerically calculated R_t**	**Experimentally measured $R_t \pm$ standard deviation**	**Difference**
(J/m^2)	(1/s)	(μm)	(μm)	(%)
$3.5x10^7$	10	465.8	490 ± 5.92	5.19
$7.1x10^7$	20	559.6	604 ± 3.80	7.93
$10.6x10^7$	30	967.5	898 ± 5.16	7.18
$14.1x10^7$	40	1030.96	1010 ± 4.84	2.03
$17.7x10^7$	50	1870.06	1920 ± 3.89	2.67

The present computational model incorporates temperature-dependent material properties such as thermal conductivity, density, heat capacity, absorptivity, viscosity, and surface tension coefficient. The deviation of these thermo-physical properties may play a critical role in generating the hydrodynamic melt motion of the liquid metal during the simulation. Furthermore, during the laser processing the crater shape is also constantly changing which can vary the angle of incidence of the laser beam. Therefore, the change in absorbance of the laser energy can cause the variation in surface temperature and consequently the temperature dependent material

properties. Hence, the more accurate thermo-physical properties can further reduce the difference between computational and experimental. Moreover, as mentioned earlier, the in-situ measurement of variable thermo-physical properties is a very challenging task due to high temperature, very short duration, and very small volume of laser-material interaction. Therefore, very limited data is presently available in the open literature. In addition, efforts are underway to minimize the difference between the results of computational model and experimental observations.

4.3 Two-dimensional (2D) Laser Machining

4.3.1 Prediction of Hydrodynamic Melt Pool Motion

The computational model facilitates the prediction of maximum temperature, which is shown with respect to time in Figure 4.13 for the Dist= 0.1mm, f=100 pulses, $E_d = 3.5\times10^6$ J/m^2, $E_{eff} = 6.02\times10^7$ J/m^2 (Table 4). During the cycle of PM moving laser beam machining, the sudden temperature increased is the resultant of the fast laser heating and the rapid decrease is the consequent effect of self-quenching and natural convection and radiation losses. It was also noticed (Figure 4.13a) that the final temperature (T_f) before the start of the consecutive pulse is ~300K, which is close to initial temperature (T_i). Particularly, this laser processing condition (Dist= 0.1mm) have a higher number of laser pulses (f= 100) and lowest time gap between two pulses (tg= 1/f= 0.01s= 10ms) and therefore it was further inferred that the temperature profile of the consecutive laser pulse remains unchanged even though the consecutive laser pulse is delivered just after 10 ms and only 0.1mm away from the previous laser pulse. For the other remaining laser processing conditions, the time gap between two pulses (tg) is even higher (tg= 0.02, 0.03, 0.04, 0.05, and 0.06) as the number of pulses delivered per second decreases (f= 50,

34, 25, 20, 17) and therefore the temperature profile in this case remains unaffected although the effective laser energy density of the processing condition varies with their corresponding pulse rate (Table 4). Based on the temperature history, the cooling rates (dT/dt) during the laser machining cycle was calculated (from melting temperature to different temperatures at various time steps) and presented in tabular format in the Figure 4.13a and 4.13b. However, the temperature history of each pulse was same for each machining conditions and therefore the calculated resultant cooling rate also remains unaltered.

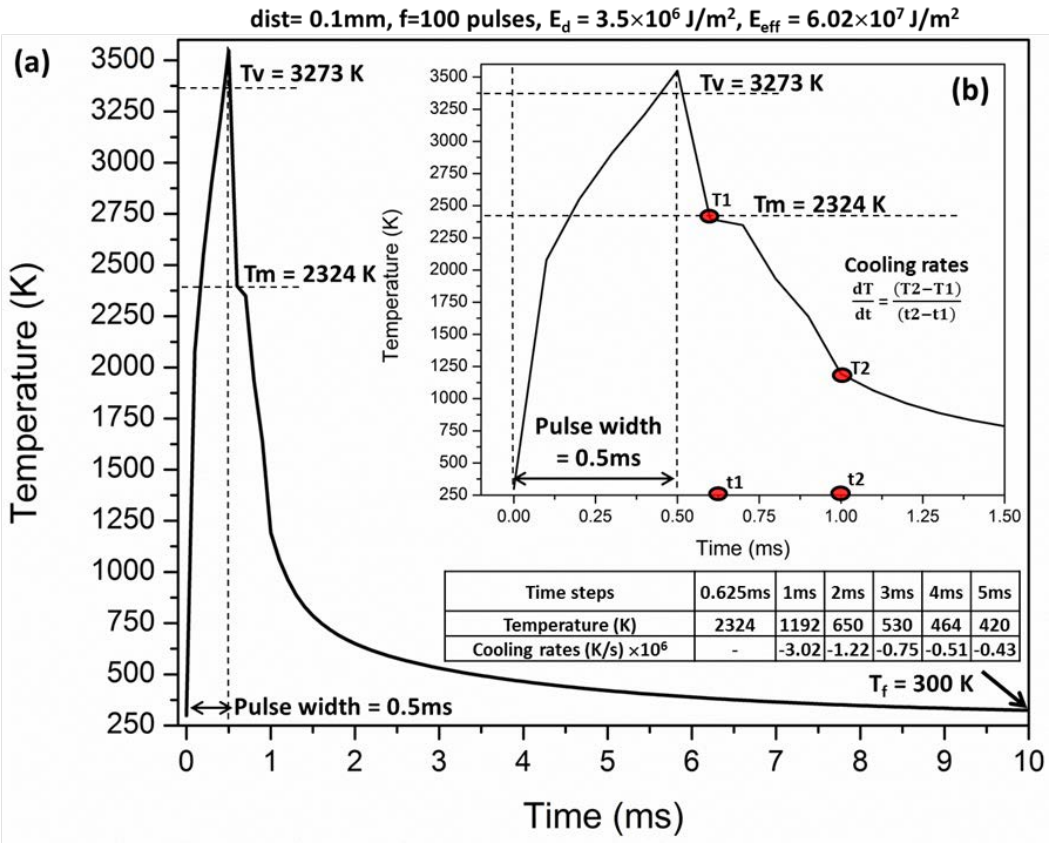

Figure 4.13 Computational plots: (a) maximum temperature as a function of time and (b) inset view of temperature vs time plot and the calculation for cooling rates (dT/dt)

During laser machining, the hydrodynamic melt pool motion is mainly influenced by the recoil pressure, surface tension, and gravitational forces. However, when instantaneous surface temperature (Ts) ≥ vaporization temperature (Tv), the recoil pressure is the significant factor to

expel the liquid material out from the crater (increase in crater depth and liquid pile-up) (Figure 4.13). The temperature history evaluated from the computational model was utilized to calculate the evaporation-induced recoil pressure under various laser machining conditions, Eq. (15). The recoil pressure (P_r) is mainly drives by the Ts and therefore variation in temperature varies the magnitude of the recoil pressure (Figure 4.14a). However, the boundary condition for recoil pressure in the present model is assigned in such a way that it applied on the surface only when Ts ≥ Tv. However, for Ts < Tv, the surface tension and gravitational forces dominate over recoil pressure to drives the hydrodynamic melt pool motion (Figure 4.13). Nonetheless, the higher cooling rates (Figure 4.13) and self-quenching at the completion of the laser pulse simultaneously affect the solidifying liquid material and tangential stresses generated by the surface tension forces provides the final profile/topography.

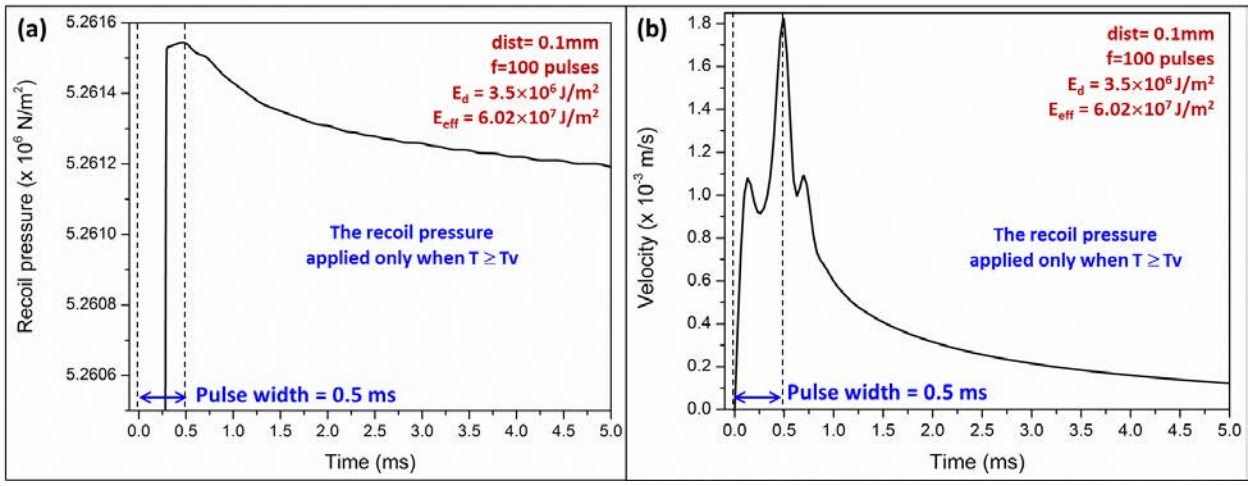

Figure 4.14 Computational plots (a) variation in recoil pressure as function of time and (b) variation in velocity profile as function of time

In the present case (Figure 4.13), during application of each laser pulse, the Ts of the material goes above the Tv for a very short time duration and that leads to the minimal material loss due to evaporation (Figure 4.13b). However, the magnitude of recoil pressure is sufficient enough to drive the more liquid material out of the crater which can be seen from the sudden

velocity rise near the end of pulse (Figure 4.14b). But, when the temperature drops below the Tv (in absence of recoil pressure), the magnitude of surface tension and gravitational forces dominate over the higher recoil pressure causing the drop in velocity of molten material (Figure 4.14b). The velocity is high at the end of laser pulse can be attributed to the highest temperature and resultant highest recoil pressure (Figure 4.13). However, as the surface temperature continuously drops down (Figure 4.13) immediately after the end of laser pulse in turn causes the gradual drop in the velocity of the molten material (Figure 4.14). Hence, net velocity of the molten material initially increased with an increase in surface temperature; boost up due to the application of recoil pressure; and gradually falls down due to decrease in surface temperature (Figure 4.14).

4.3.2 Prediction of Surface Topography

In the PM moving laser beam machining, the material undergoes various thermo-physical phenomena that resulted into the specific surface deformation, which is the truly a footprint of selected laser machining parameters such as scanning speed (Vin) of laser beam and the application of laser pulses at predefined pule rates (f). The computationally predicted surface deformation plots (after solidification), which is clearly distinguish based on the distance between two pulses (Dist = 0.1 to 0.6) or lateral overlap (0, 17, 33, 50, 67, and 83%) are presented in Figure 4.15. A lateral overlap between two consecutive laser pulses is systematically increased (0 to 83%) with an increase in the distance between two pulses (Dist = 0.6 to 0.1) and the corresponding variation in the resultant surface roughness parameters, Sp (highest peak height), Sv (highest valley depth), and Sz (maximum height of the surface profile, Sz = Sp + Sv) are shown in Figure 4.16.

Sp: highest peak height, Sv: highest valley depth, Sz: maximum height of the surface profile, Sz = Sp+Sv

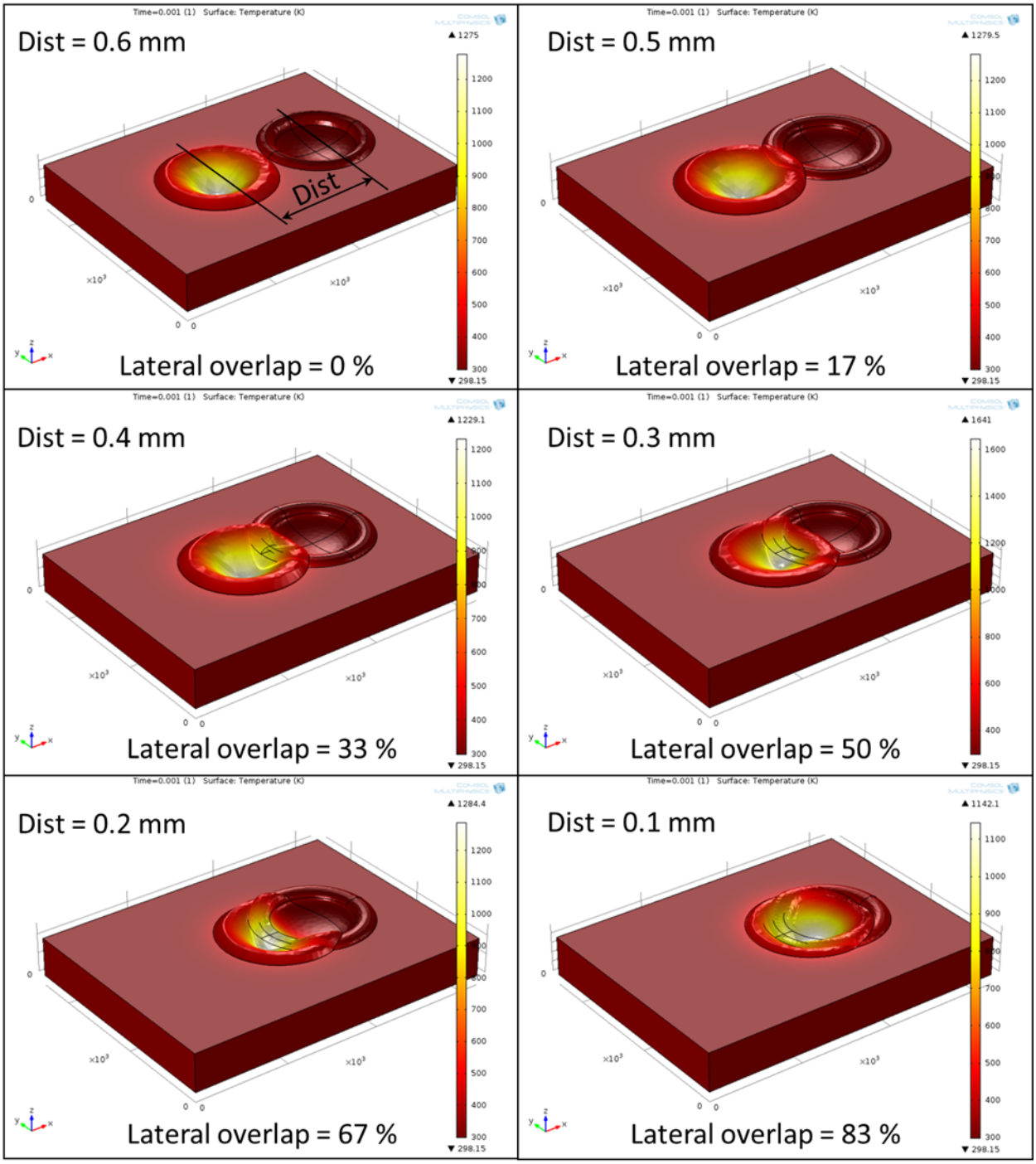

Figure 4.15 Predicted surface profile (topography) for various distances between two pulses (Dist = 0.1 to 0.6mm)

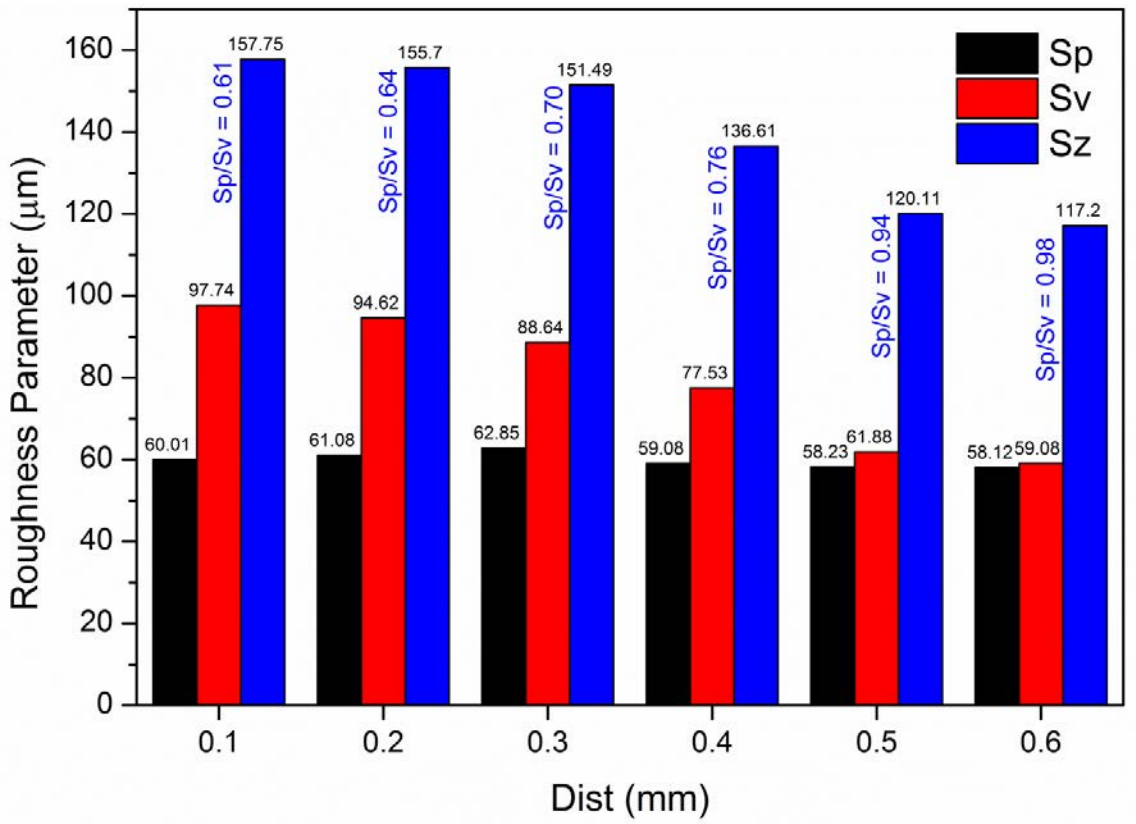

Figure 4.16 Computationally predicted surface roughness parameters for various distances between two pulses (Dist = 0.1 to 0.6mm)

For Dist=0.6mm, the two consecutive laser pulses and resultant surface deformation are distinctly separated from each other (Figure 4.15), which is resulted into the specific surface profile (Figure 4.16). In this case, the ratio of pile up height to crater depth (Sp/Sv) is 0.98 (close to one). However, with the decrease in distance between two pulses (Dist=0.5 to 0.1 mm), the surface deformation occurred on the previously evolved surface profile (Figure 4.15), and therefore, material experiences the repeated surface melting, vaporization, and re-solidification and resultant influence of recoil pressure, surface tension, and gravitational forces. Since, the re-solidification occurred on the previously created crater and pile up that dramatically causes the increase in surface roughness parameter (Sz). Although, it was also observed that the variation in crater depth (Sv) is more significant than the pile up height (Sp) for the selected laser machining

conditions (Dist=0.5 to 0.1 mm), which causing the systematic reduction in the Sp/Sv ratio. Initially, with the decrease in Dist (from 0.6 to 0.3mm), the re-solidification predominantly happened on the pile up than the crater that caused the increase in pile up height (Sp). Though, with the decrease in Dist (from 0.3 to 0.1 mm), the re-solidification predominantly happened on the crater as compared to pile up that causing the systematic increase in crater depth (Sv) and decrease in pile up (Sp), as shown in Figure 4.16.

4.3.3 Validation of Computational Model - 2D Laser Machining

To validate the predictions of computational model, the optical profilometer was used to measure the surface roughness parameters (Sp, Sv, and Sz) for various distances between two pulses (Dist = 0.1 to 0.6mm), as shown in the Figure 4.17. Experimentally, it was also observed that the as the distance between two pulses decreased (from 0.5 to 0.1mm), the re-solidification occurred on the previously created crater and pile that causes the increase in surface roughness parameter (Sz) as well as decrease in Sp/Sv ratio, which follows the same trend as previously predicted by the computational model (Figure 4.16 and 4.17). In addition, the predicted and measured surface roughness parameters from the computational model and experimental observations under various adopted laser machining conditions are summarized and differences are enumerated in Table 8. The deviation of surface roughness parameters among the prediction and experimental measurements are within the range of ± 3.5%, thereby successfully validating the computational model. However, the present deviation in the computational model may be due to the incorporated boundary conditions and temperature dependent material properties as suggested by various literatures and as a result causes the slight variation in fluid flow and solidification phenomena and its subsequent effects on the surface roughness.

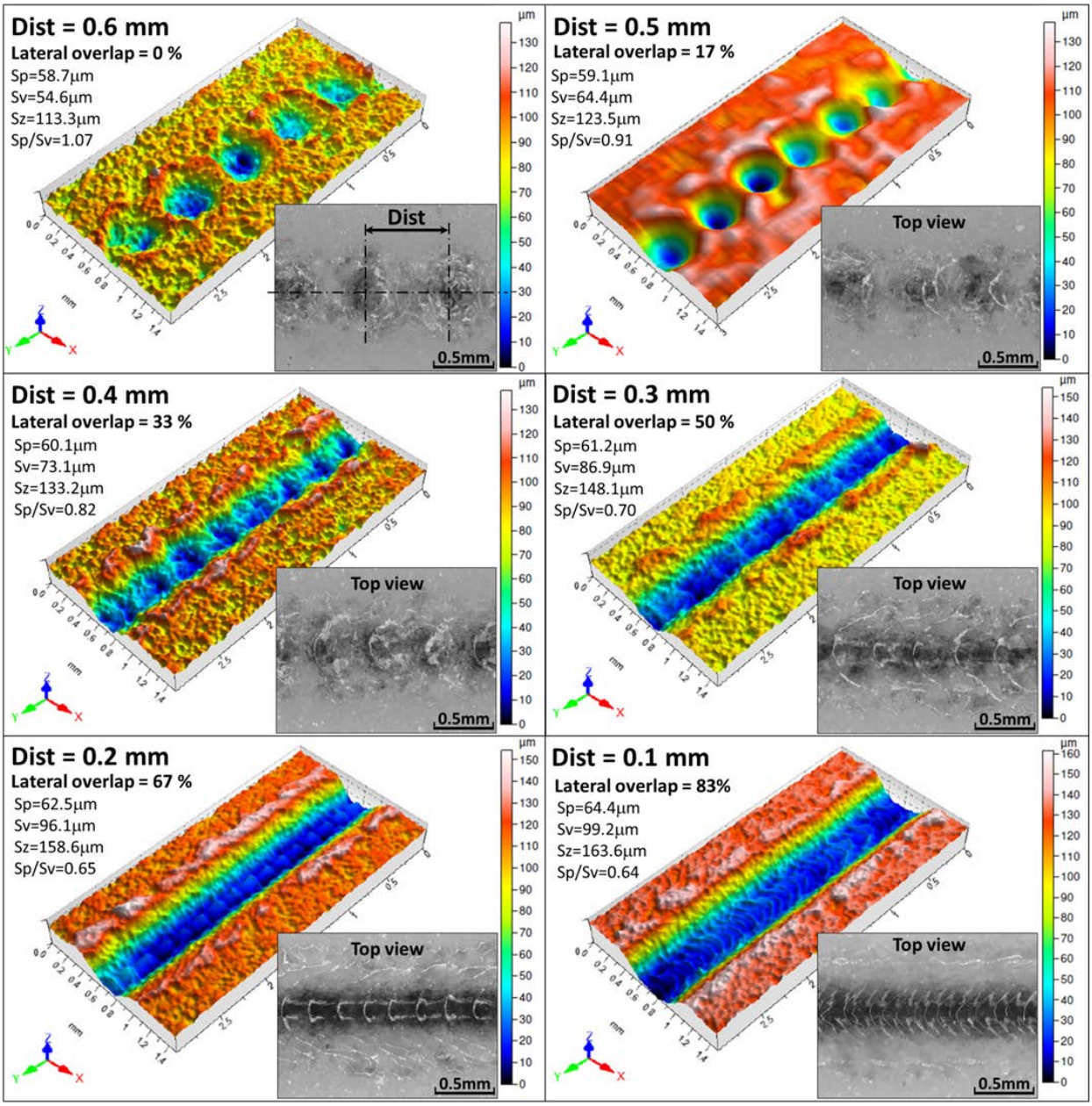

Figure 4.17 Experimentally measured surface topography/profile (ISO 25178) for various distances between two pulses (Dist = 0.1 to 0.6mm). The inset view shows the top view of low magnification image

Table 8 Computationally predicted and experimentally measured surface roughness for 2D (moving laser beam) laser machining conditions

Average energy density per pulse, E_d	**Effective laser energy density per second, E_{eff}**	**Distance between two laser pulses, Dist**	**Computationally predicted S_z**	**Experimentally measured $S_z \pm$ standard deviation**	**Difference**
(J/m^2)	(J/m^2)	(1/s)	(μm)	(μm)	(%)
3.5×10^6	6.02×10^7	0.6	117.20	113.3 ± 4.53	3.57
	7.08×10^7	0.5	120.11	123.5 ± 4.18	1.82
	8.85×10^7	0.4	136.61	133.2 ± 6.11	-2.28
	12.0×10^7	0.3	151.49	148.1 ± 5.83	-2.56
	17.7×10^7	0.2	155.70	158.6 ± 5.41	2.74
	35.4×10^7	0.1	157.75	163.4 ± 5.94	-3.44

Furthermore, during laser processing the shape of crater is constantly varying that resulted into the variation in absorptivity parameter that in turn induces the deviation in temperature field and the correspondingly on the material properties. Therefore, the adoption of more precise material properties can further reduce the difference between computational and experimental results. In light of this, efforts are in progress to reduce the deviation of computational predictions.

4.4 Three-dimensional (3D) Laser Machining

The same computational model for 2D laser machining is utilized to investigate the influence of various laser processing conditions (Table 5). Moreover, the lateral and transverse overlap distances used in the present work are ranging from 0.1 to 0.6 and therefor total of six processing conditions (0.6×0.6, 0.5×0.5, 0.4×0.4, 0.3×0.3,0.2×0.2, and 0.1×0.1mm) are used to process the structural alumina. The experimentally measured surface topography for these particular processing conditions is shown in Figure 4.18.

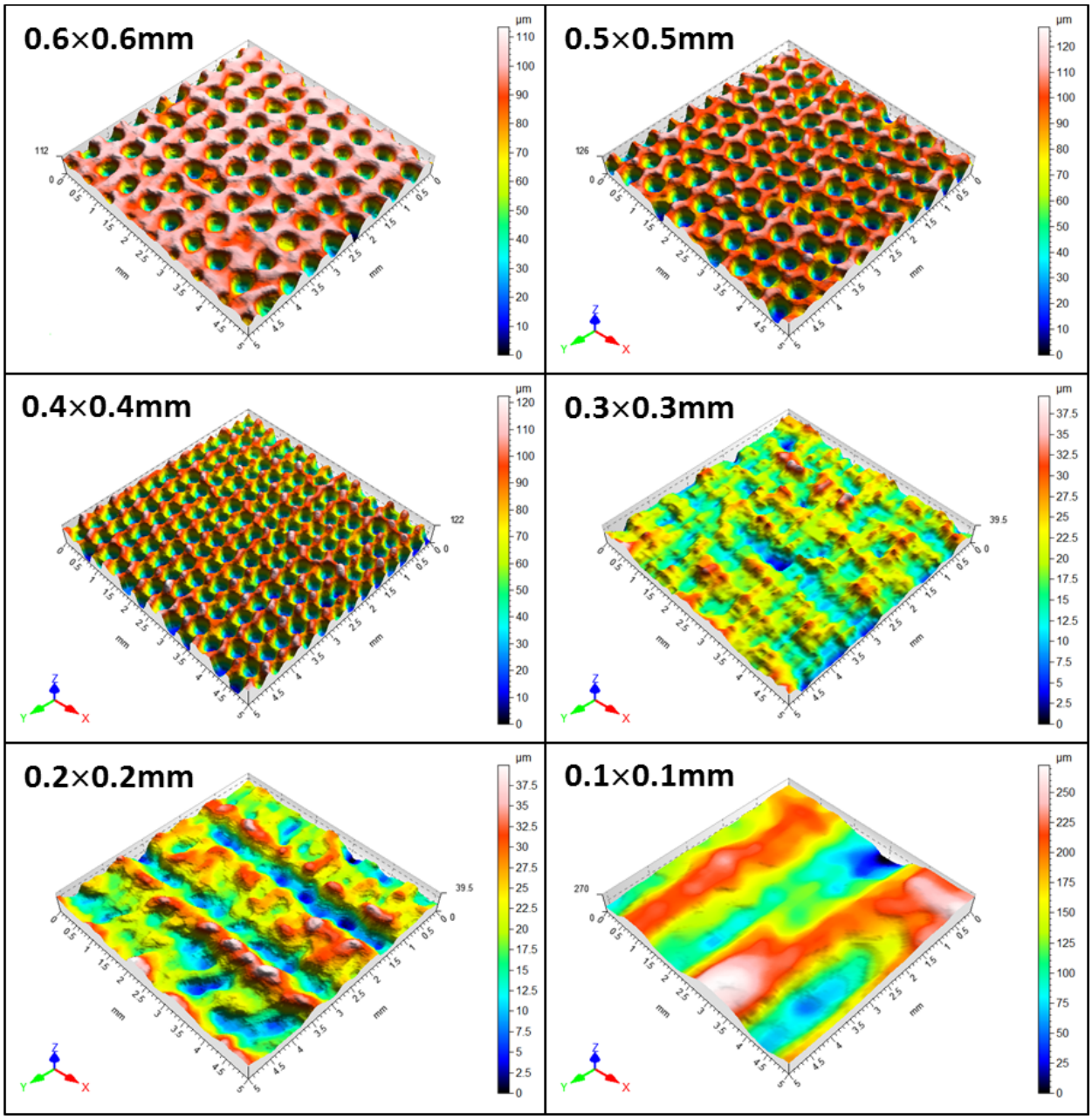

Figure 4.18 Experimentally measured surface topography/profile (ISO 25178) for various lateral and transverse overlap distances (Dist = O_T = 0.1 to 0.6mm).

A lateral and transverse overlap between two consecutive laser pulses is systematically increased (0 to 83%) with an increase in the distance between two pulses (Dist = 0.6 to 0.1mm and O_T = 0.6 to 0.1mm) and the corresponding variation in the resultant surface roughness parameters (Sp, Sv and Sz, where Sz = Sp+Sv) are shown in Figure 4.19. Table 9 summarized

the depth of cavity removed and obtained material removal rates (MRR) of corresponding 3D laser machining conditions.

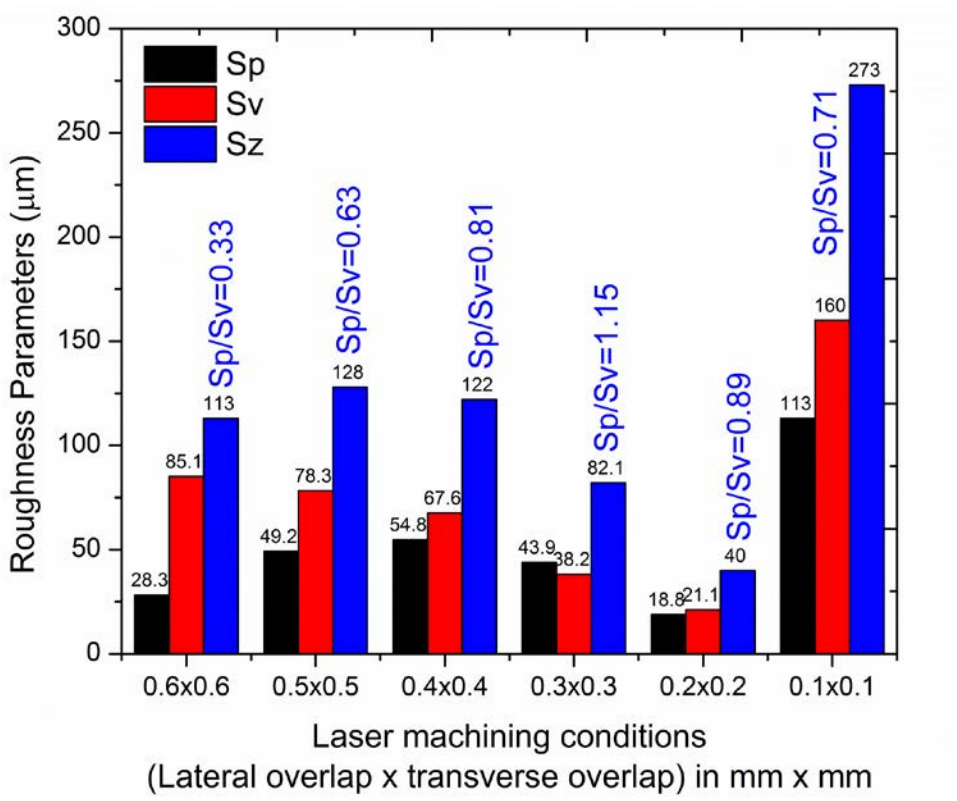

Figure 4.19 Experimentally measured surface roughness parameters for various lateral and transverse overlap distances (Dist = 0.1 to 0.6mm and O_T = 0.6 to 0.1mm)

Table 9 Experimentally measured attributes of machined cavities during 3D laser machining

Average energy density per pulse, E_d	**Effective laser energy density per second, E_{eff}**	**Lateral overlap, Dist**	**Transverse overlap, O_T**	**Sp/Sv ratio**	**Depth of cavity removed**	**Material removal rate**
(J/m^2)	(J/m^2)	(mm)	(mm)		(μm)	(mm^3)
3.5×10^6	6.02×10^7	0.6	0.6	0.33	37.1	0.93
	7.08×10^7	0.5	0.5	0.63	124	3.10
	8.85×10^7	0.4	0.4	0.81	126	3.15
	12.0×10^7	0.3	0.3	1.15	167	4.18
	17.7×10^7	0.2	0.2	0.89	191	4.78
	35.4×10^7	0.1	0.1	0.71	1000	25.00

For 0.6×0.6mm, the ratio of pile up height to crater depth (Sp/Sv) is 0.33, corresponding surface parameter (Sz) is 113μm (Figure 4.19), and depth of material removed during laser machining is 37.1 μm (Table 9) that gives the material removal rates of 0.93 mm^3 (for 5×5mm cavity). However, with a decrease in overlap (from 0.6×0.6 to 0.5×0.5 mm), surface roughness parameter (Sz) increased from 113 to 128 μm, which is mainly due to the re-solidification occurred on the previously created pile up. Therefore, due to the predominance of pile up height (Sp) over crater depth (Sv) causing the systematic increase in the Sp/Sv ratio (from 0.33 to 0.63). Due to the repetition of consecutive laser pulse is 0.5mm away from the previous pulse and corresponding laser energy density in turn removes the material of depth 124 μm (Table 9). Furthermore, for laser processing conditions with 0.4×0.4 to 0.2×0.2 mm (Dist×O_T), the surface deformation occurred on the previously evolved surface profile dramatically causes the decrease in surface roughness parameter (Sz) from 128 to 40μm. Particularly, for 0.4×0.4 to 0.2×0.2 mm, pile up height (Sp) is more significant than crater depth (Sv) causing the systematic increase in the Sp/Sv ratio (from 0.63 to 0.81 to 1.15). However, for 0.2×0.2 mm, crater depth (Sv) is more significant than pile up height (Sp) causing the sudden reduction in the Sp/Sv ratio (from 1.15 to 0.89). Moreover, as the overlap distances further decreased from 0.2×0.2 to 0.1×0.1 mm the laser processing and re-solidification predominately happened on the previously created crater that causes the sudden increase in surface roughness parameter (Sz). In this case, the crater depth (Sv) is more significant than pile up height (Sp) that causes the rapid reduction in the Sp/Sv ratio (from 0.89 to 0.71). Also, the depth of cavity removed due to evaporation is 1000 μm and corresponding material removal rate is 25 mm^3 (Table 9), which is highest in the presently used machining conditions.

In the present efforts, a Rigaku III Ultima X-ray diffractometer generating Cu Kα radiation (1.5418 Å wavelength), operating at 40 kV and 44 mA in a 2θ range of 20 - 90° (step size of 0.02° and scanning speed of 2 degree/minute) was employed to do the XRD analysis of the laser machined alumina machined using various laser energy density processing conditions to evaluate the phase transformation. Standard international center for diffraction data (ICDD) from the joint committee of powder diffraction standards (JCPS) was utilized for phase identification. However, XRD plot (Figure 4.20) shows that the all the peaks of laser machined alumina matching with the unprocessed alumina that corresponds to the α-Al_2O_3, evidently confirmed the no phase transformation occurred during the present 3D laser machining conditions.

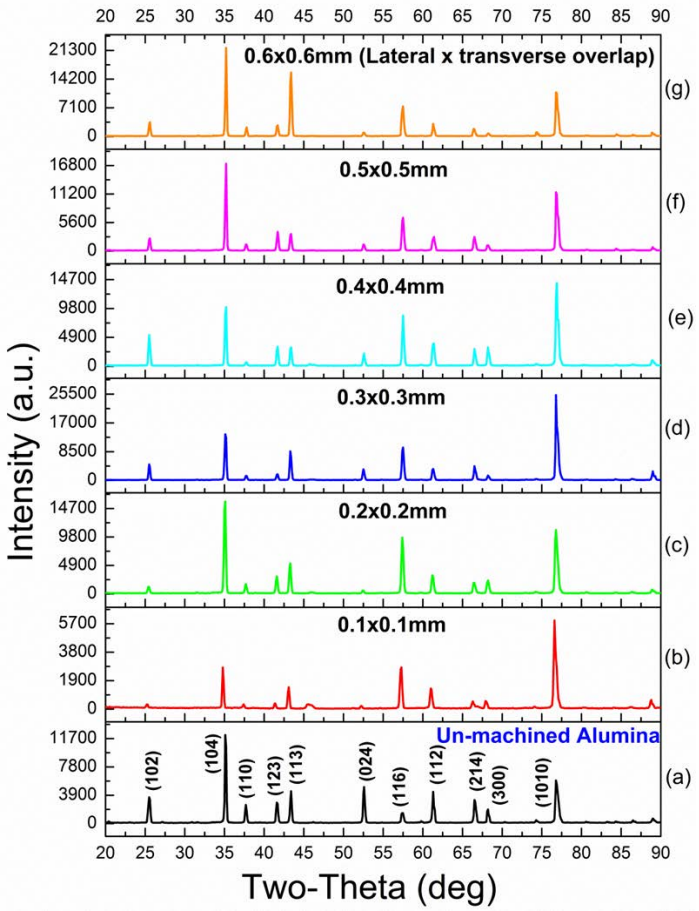

Figure 4.20 XRD plots of (a) un-machined alumina and (b-g) laser machined alumina processed using various 3D laser machining conditions (lateral×transverse overlap)

4.4.1 Validation of Computational Model - 3D Laser Machining

As discussed earlier, the optical profilometer was used to measure the surface roughness parameters (Sp, Sv, and Sz) for various distances between two pulses (Dist = 0.1 to 0.6mm) to validate the predictions of computational model. The predicted and measured surface roughness parameters from the computational model and experimental observations under various adopted during 3D laser machining conditions is summarized in Table 10. The deviation of surface roughness parameters among the prediction and experimental measurements are within the range of ± 6%, thereby successfully validating the computational model. However, the present deviation in the computational model may be due to the incorporated boundary conditions and temperature dependent material properties as suggested by various literatures and as a result causes the slight variation in fluid flow and solidification phenomena and its subsequent effects on the surface roughness.

Table 10 Computationally predicted and experimentally measured surface roughness for 3D laser machining conditions

Average energy density per pulse, E_d	**Effective laser energy density per second, E_{eff}**	**Lateral overlap, Dist**	**Transverse overlap, O_T**	**Predicted S_z**	**Measured S_z ± standard deviation**	**Difference**
(J/m^2)	(J/m^2)	(mm)	(mm)	(μm)	(μm)	(%)
3.5×10^6	6.02×10^7	0.6	0.6	116.1	113.3 ± 7.67	-2.74
	7.08×10^7	0.5	0.5	121.3	128 ± 1.96	5.23
	8.85×10^7	0.4	0.4	117.17	122 ± 6.11	3.96
	12.0×10^7	0.3	0.3	78.2	82.1 ± 2.02	4.75
	17.7×10^7	0.2	0.2	41.98	40 ± 0.293	-4.95
	35.4×10^7	0.1	0.1	257.05	273 ± 1.56	5.84

4.5 Thermal Stresses

4.5.1 One-dimensional (1D) Laser Machining - Single Laser Pulse

The temperature history predicted on the top surface of the geometry (Figure 2.2d) of the 1D single laser pulse computational model was further utilized to evaluate the thermal stresses (σ_T), which is calculated based on the Eq. (25). The thermal stress at the end of the laser pulse (after 0.5ms) on the top of the surface was shown in the Figure 4.21.

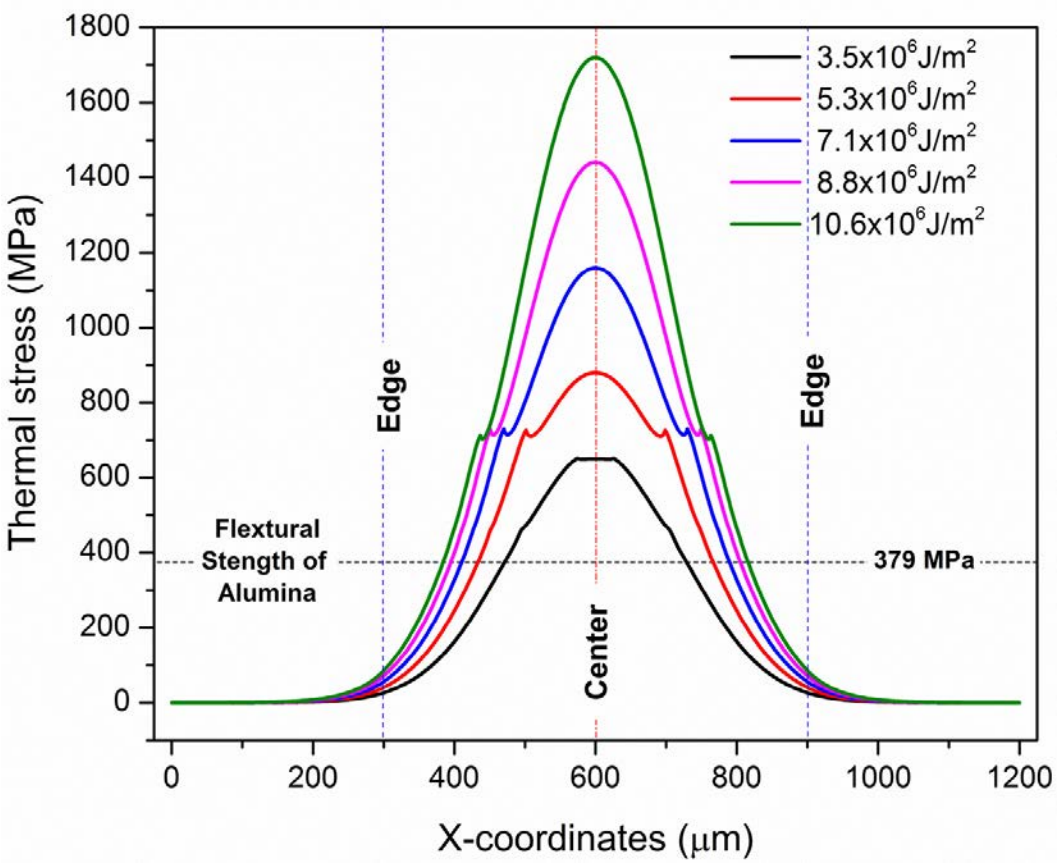

Figure 4.21 Predicted thermal stresses of alumina at the end of the laser pulse (0.5ms) during various 1D (single pulse) laser machining conditions

Due to the localized nature of laser beam, the surface temperature in confined volume is instantaneously increased (Figure 4.1a). However, the remaining surrounding material acts as a heat sink which subsequently decreases the temperature along with the heat loss due to radiation and convective cooling. As a cumulative result, the material experiences higher cooling rates

($dT/dt > 10^5$ K/s) (Figure 4.1b). In addition, due to the Gaussian distribution of the laser beam, the center of the laser beam supplies higher laser energy density and gradually decreased as moving towards the edges that in turn causing higher temperatures at center compared to edges of the laser beam. As a result, material experiences preferential heat conduction as well as higher temperature gradient at the end of the laser pulse (0.5ms) in turn induces the higher thermal stresses at the center than the edges of the laser beam (Figure 4.21). Also, it was observed (Figure 4.1a) that the peak temperature increases with increasing laser pulse energy density that lead to higher thermal stresses (Figure 4.21). The Figure 4.21 shows the contour plot to illustrate the distribution of transient thermal stresses at the end of 0.5ms laser pulse (Figure 4.22a) and the residual stresses at the room temperature (Figure 4.22b). It is observed that the alumina undergoes higher thermal stresses than its flexural strength (379 MPa) at the end of the 0.5ms laser pulse during all the existing 1D laser machining conditions presently used. In this case, it is anticipated that the micro-crack can nucleates. However, the SEM micrograph of the laser machined alumina shows very few micro-cracks (Figure 4.23) significantly at the center of the crater. This may be due to the transient thermal stress is momentarily higher and after the end of 0.5ms laser pulse thermal stresses keeps on decreasing and reached to its minimal values. The computational model also estimates the residual stresses at room temperature, which is shown in Figure 4.22b. It was observed that the residual stresses are very low in magnitude and predominately concentrated mainly around the crater that mainly due to the Gaussian beam profile of laser beam and preferential thermal gradient caused by the localized heating and rapid cooling rates.

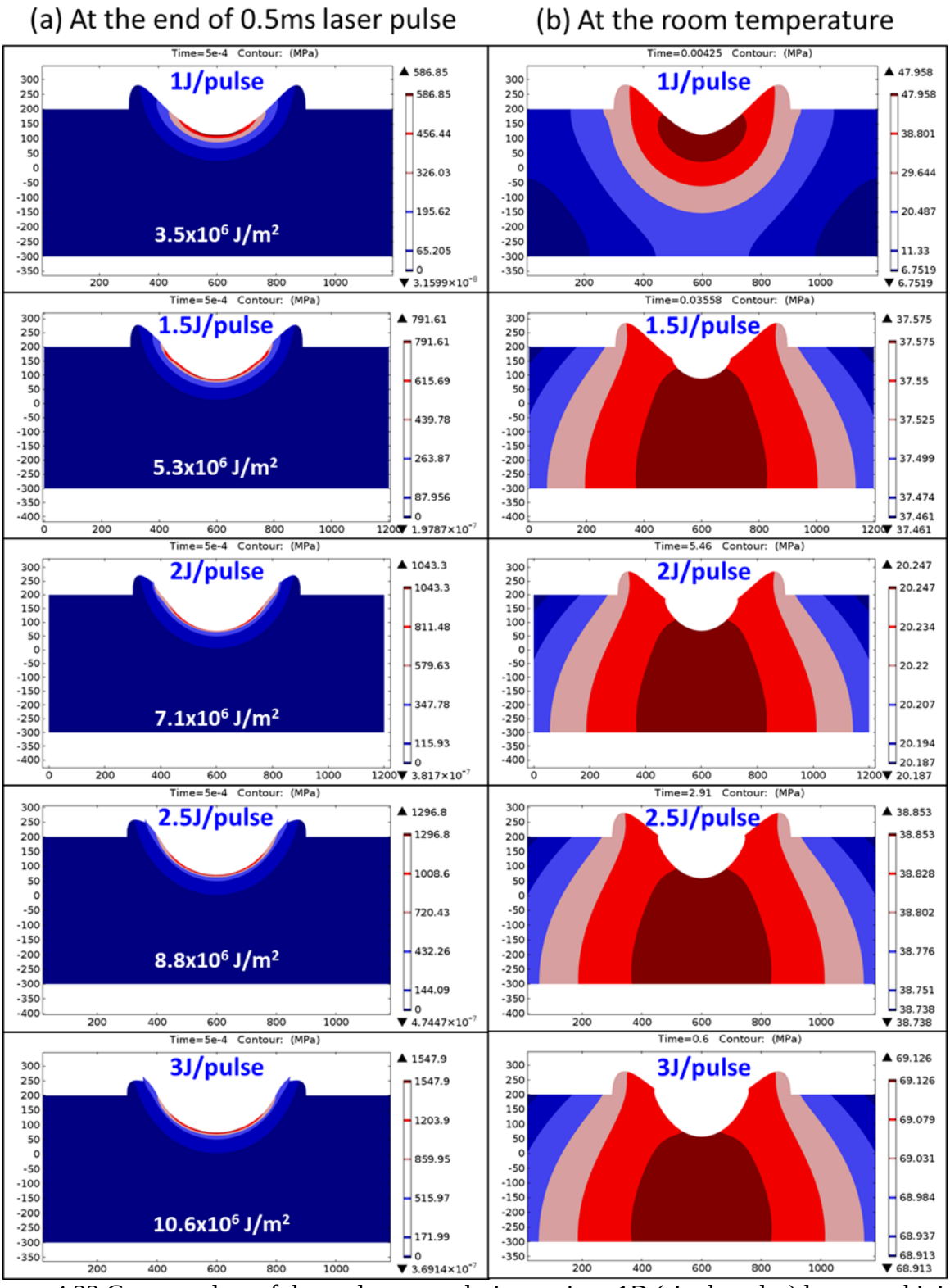

Figure 4.22 Contour plots of thermal stresses during various 1D (single pulse) laser machining conditions

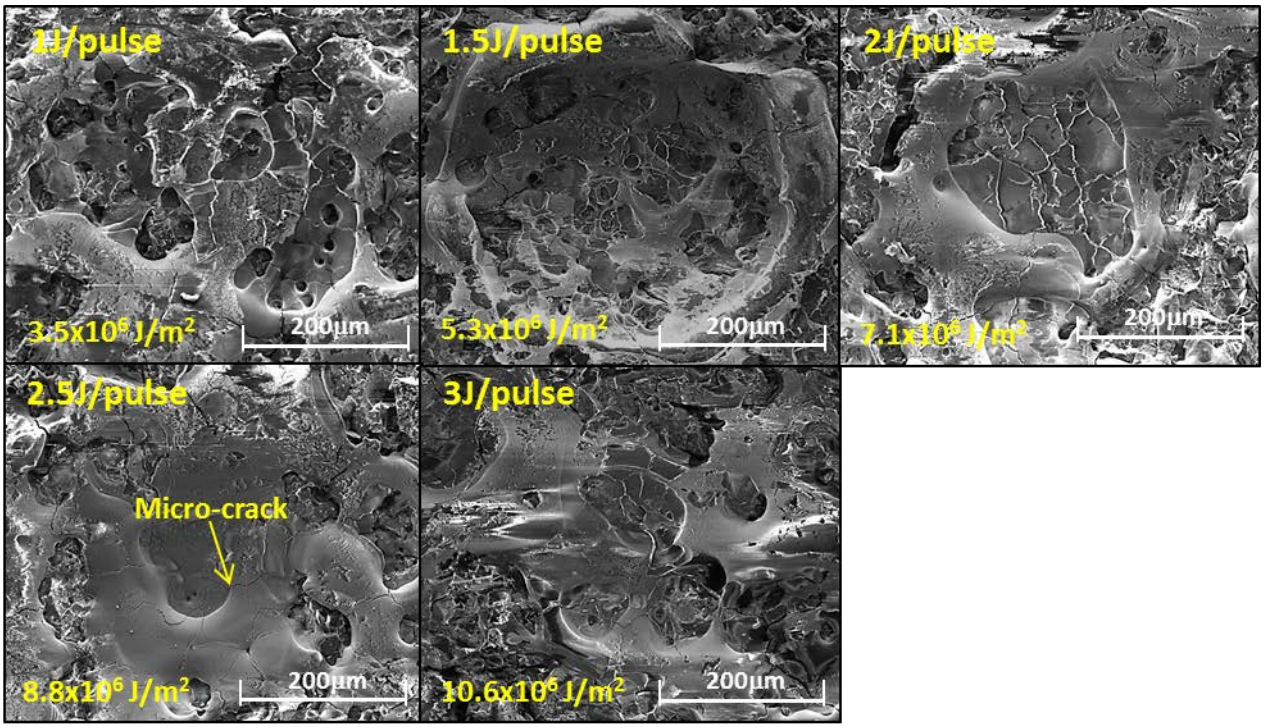

Figure 4.23 SEM micrograph of the top surface of machined alumina using various 1D (single pulse) laser machining conditions

4.5.2 One-dimensional (1D) Laser Machining - Multiple Laser Pulses

Thermal stresses are calculated as similar to 1D (single pulse) laser machining. Figure 4.24 shows the transient thermal stresses at the end of the laser pulse. The thermal stresses on the top surface of the alumina is increasing with increase in number of laser pulses (or laser energy density) and highest thermal stresses (1019 MPa) are evaluated at the center of the laser beam for the 50 laser pulse (17.7×10^6 J/m^2) laser processing condition. However, all the processing conditions exceed the flexural strength limit of the alumina (379 MPa) that in turn sufficient to nucleate micro-cracks and few numbers of cracks with smaller length was evidently found on the SEM micrograph (Figure 4.25). Moreover, the estimated residual stresses (Figure 4.26) are within the range of 25 to 38 MPa and mainly concentrated below or near the crater.

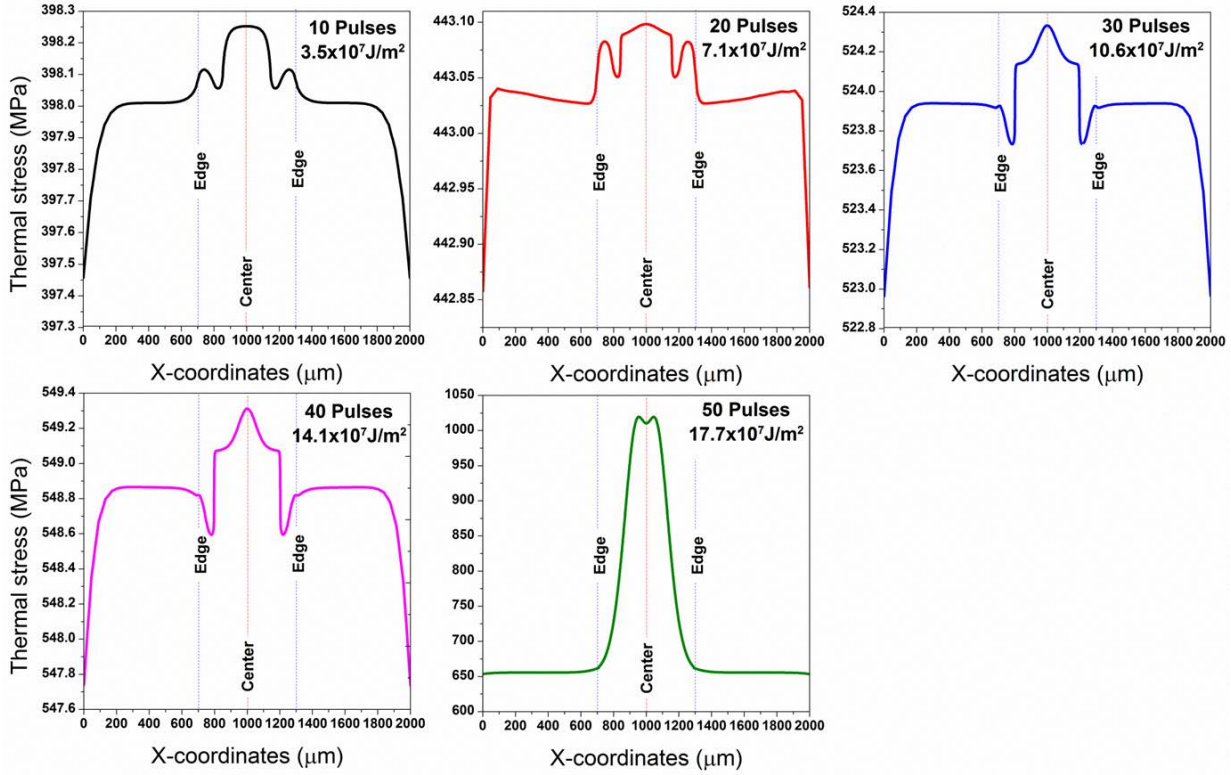

Figure 4.24 Predicted thermal stresses of alumina at the end of the laser pulse (0.5ms) during various 1D (Multiple laser pulses) laser machining conditions

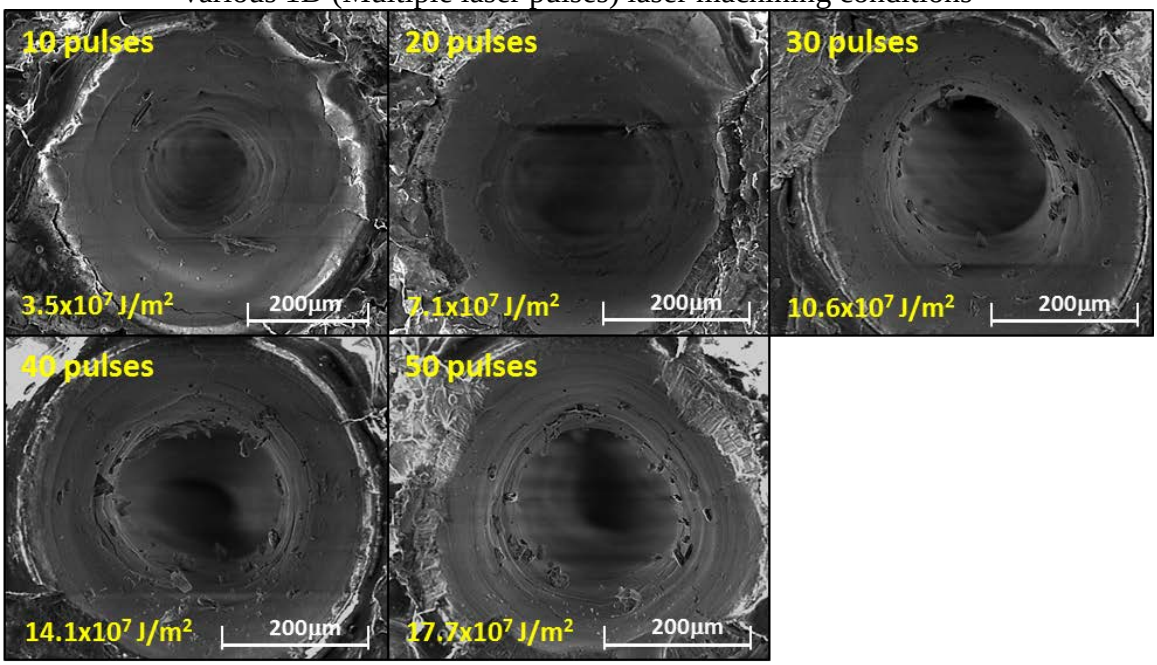

Figure 4.25 SEM micrograph of the top surface of machined alumina using various 1D (multiple laser pulses) laser machining conditions

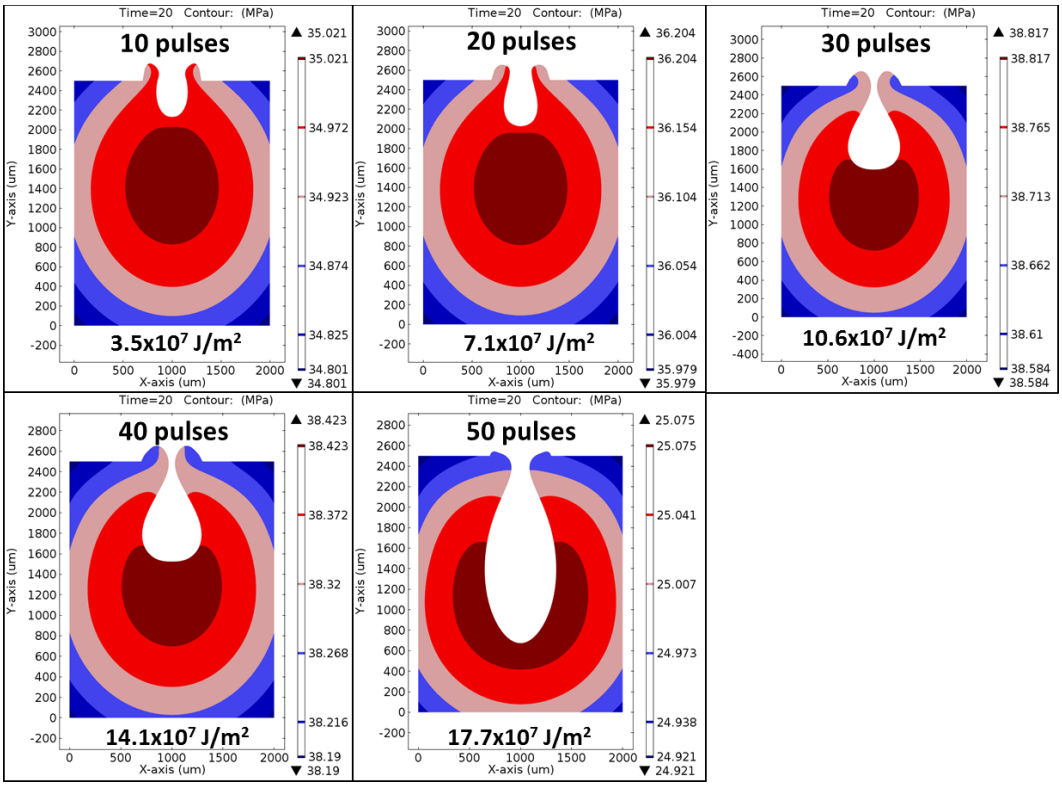

Figure 4.26 Contour plots of thermal stresses during various 1D (multiple laser pulses) laser machining conditions

4.5.3 Two-dimensional (2D) Laser Machining - Lateral overlap

As similar to 1D (single pulse) laser machining, the transient thermal stresses are evaluated and corresponding counter plot at the end of 0.5ms second pulse is as shown in Figure 4.27 and found that the thermal stresses are higher at the center of the crater. Since all the processing conditions uses 1J laser energy per pule and final temperature before the consecutive laser pulse is same as initial temperature causing no temperature build up during the subsequent laser processing (Figure 4.13). As a result, the temperature profile of each laser pulse remains the same and corresponding thermal stresses produced after the end of second pulse is shown in the Figure 4.27. It was observed that the estimated thermal stresses are crossing the flexural strength limit of alumina and which likely to produced micro-cracks. However, very few micro-cracks were evidently seen in the SEM micrograph (Figure 4.28).

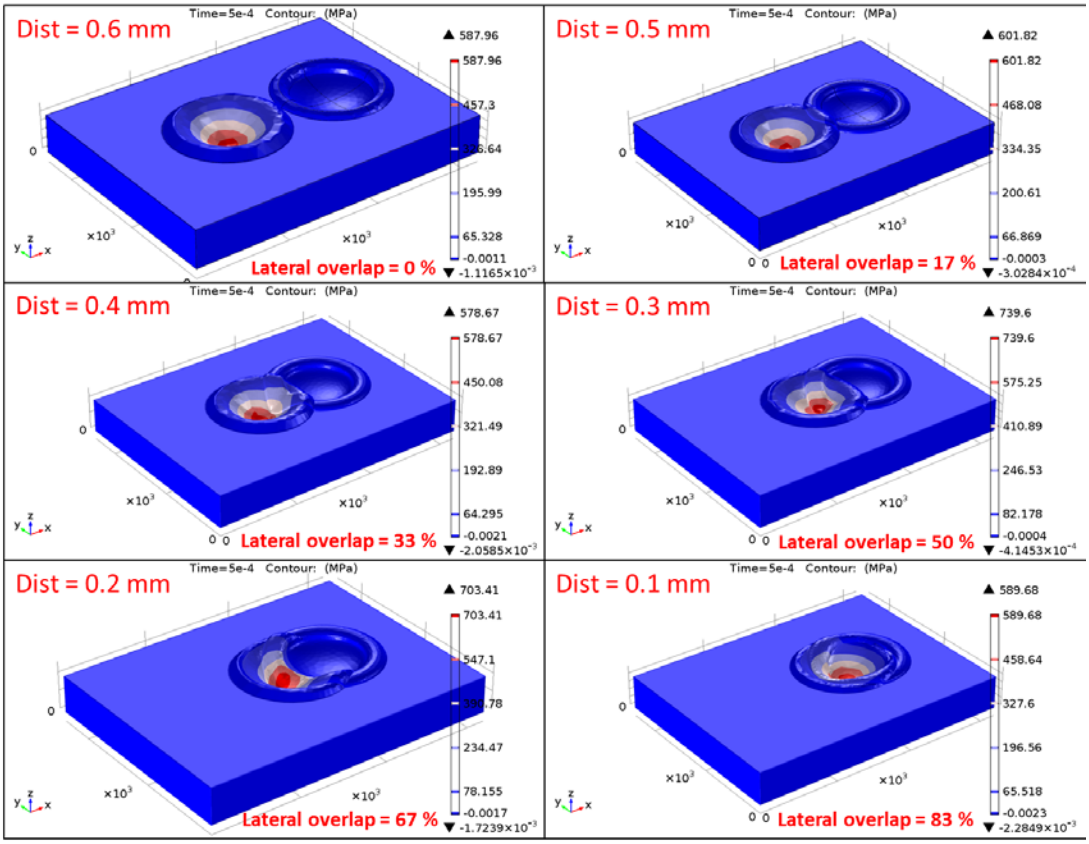

Figure 4.27 Predicted thermal stresses of alumina at the end of the laser pulse (0.5ms) during various 2D (moving laser, lateral overlap) laser machining conditions

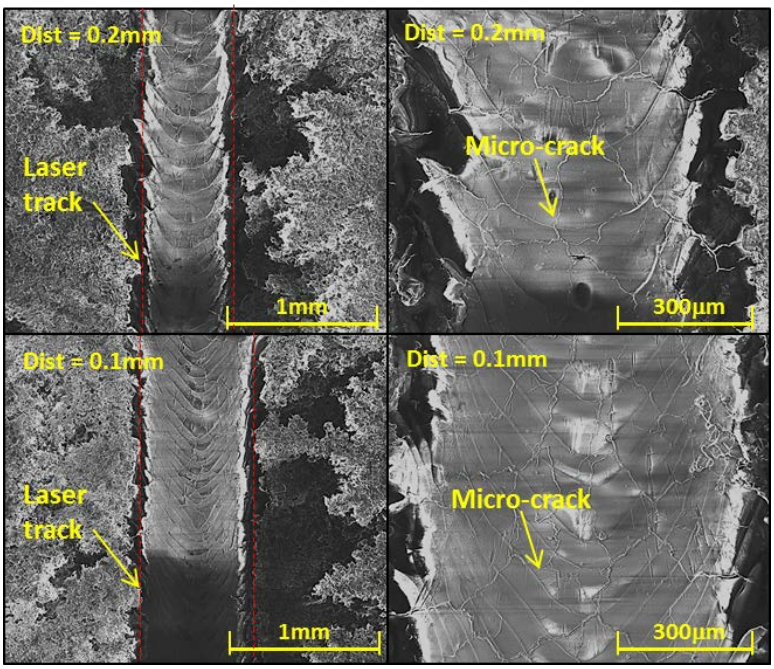

Figure 4.28 SEM micrograph of the top surface of machined alumina using various 2D laser machining conditions

4.5.4 Three-dimensional (3D) Laser Machining - Lateral and transverse overlap

As similar to 1D (single pulse) laser machining, the transient thermal stresses are evaluated along top surface (x-axis) and perpendicular to top surface (symmetric or center axis) along y-axis, which is as shown in Figure 4.29. Similar to 2D machining, all the processing conditions are carried using 1J laser energy per pule and therefore temperature history per pulse remains same (Figure 4.13). As a consequence, the corresponding transient thermal stresses profile produced during the end of one pulse cycle is shown in the Figure 4.29. It was observed that the estimated thermal stresses are crossing the flexural strength limit of alumina that induced the micro-cracks. However, very few micro-cracks were evidently seen in the SEM micrograph (Figure 4.30).

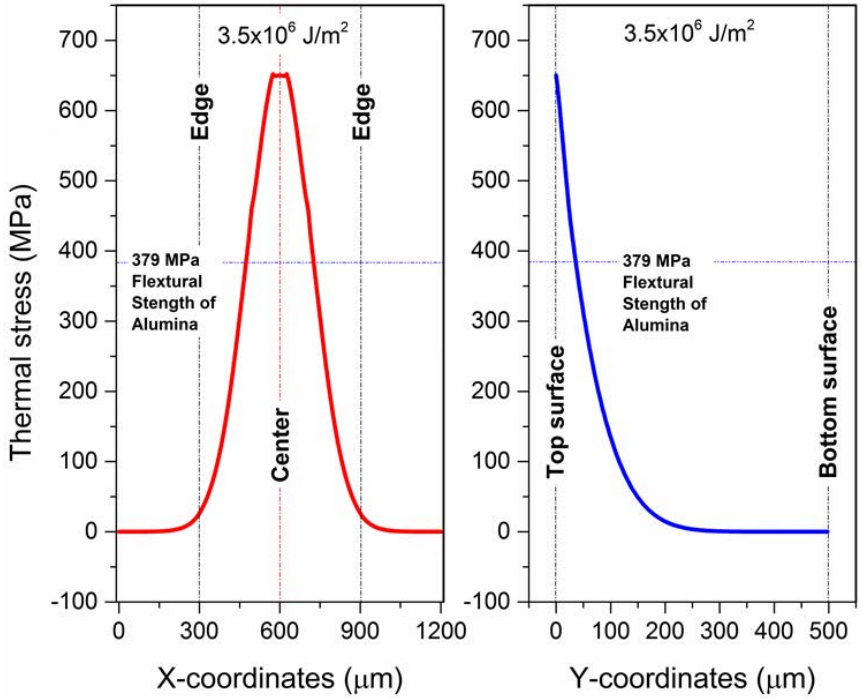

Figure 4.29 Predicted thermal stresses of alumina at the end of the laser pulse (0.5ms) during various 2D (moving laser, lateral overlap) laser machining conditions

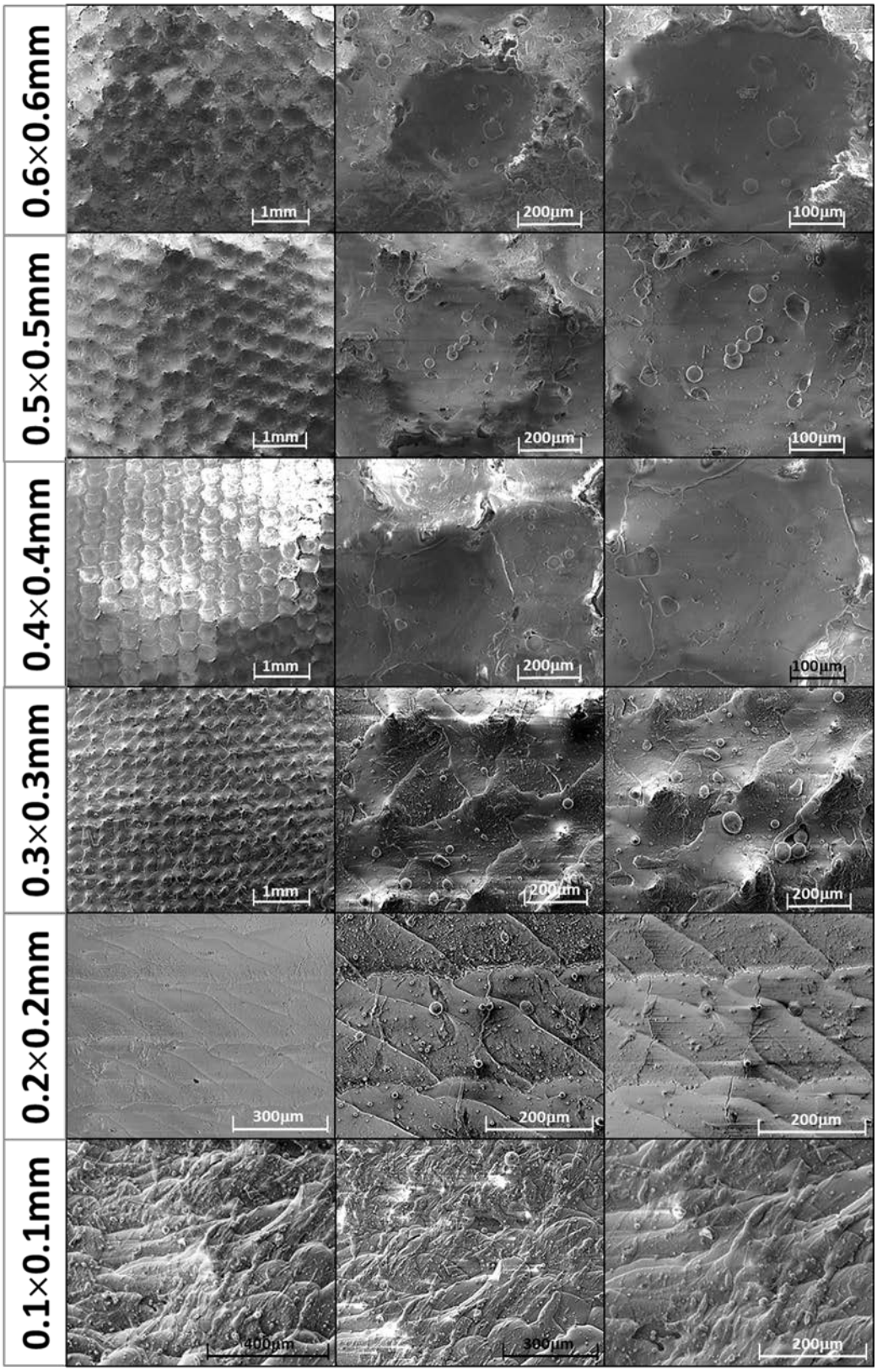

Figure 4.30 SEM micrograph of the top surface of machined alumina using various 3D laser machining conditions

CHAPTER 5

CONCLUSION[5]

5.1 One-dimensional (1D) Laser Machining - Single Laser Pulse

A computational model using multiphysics was developed to understand the influence of single-pulse one-dimensional laser machining on the surface finish of alumina under various laser energy densities. Results indicated that the material loss due to ablation increased the crater depth, while the strong velocity gradient created by the recoil pressure increased the liquid pile-up. Both of these effects increased the overall surface roughness. In this study, less material removal with a better surface finish was predicted with the help of computational model which was validated by the experimental results. A close agreement and a similar trend were observed between the computational and the experimental results. The thermal stresses produced during the 1D (single pulse) laser machining conditions exceeds the flexural strength of the alumina that likely to nucleate micro-cracks and SEM micrograph evidently shows very few cracks inside the machined crater. The present efforts for single-pulse one-dimensional laser machining indicated the feasibility of extension of the computational model for prediction of surface roughness in two- and three-dimensional laser machining.

5.2 One-dimensional (1D) Laser Machining - Multiple Laser Pulses

A computational model was designed and developed to understand the influence of multiple laser pulses on the surface finish of alumina for various laser energy density machining conditions. Results indicate that the material lost due to evaporation causes an increase in crater

[5] Parts of this chapter have been previously published, either in part or in full, from (1) Hitesh D. Vora, Soundarapandian Santhanakrishnan, Sandip P. Harimkar, Sandra K.S. Boetcher, Narendra B. Dahotre, *Journal of European Ceramic Society* 2012, 32 (16), 4205–4218 with permission from Elsevier, and (2) Hitesh D. Vora, Soundarapandian Santhanakrishnan, Sandip P. Harimkar, Sandra K.S. Boetcher, Narendra B. Dahotre, *International Journal of Advanced Manufacturing Technology* 2013, 68(1), 69-83 with permission from Springer

depth; whereas liquid expulsion created by the recoil pressure increase the pile-up height. However, after a critical crater depth (~260 μm), the magnitude of the recoil pressure was insufficient to eject the significant amount of liquid material out of the crater and hence the liquid material solidified inside the crater wall leading to formation of typical tear drop shape topography. In this study, it was found that the surface roughness increased with increasing pulse rate (10, 20, 30, 40, and 50) or the increase in average laser energy density. A close agreement and a similar trend were observed between the predicted roughness values of computational model with experimental observations. During the 1D (multiple laser pulses) laser machining conditions, computationally predicted thermal stresses crosses the flexural strength limit of structural alumina that is sufficient enough to nucleate the micro-cracks within surface and sub-surface regions. SEM micrograph confirmed this finding but the numbers of micro-cracks observed are very few and predominately found inside the machined crater.

5.3 Two-dimensional (2D) Laser Machining

A computational model was designed and developed to understand the influence of PM moving laser beam (with lateral overlap of 0, 17, 33, 50, 67, and 83%) on the surface roughness of structural alumina for various laser energy density machining conditions (Dist = 0.6, 0.5, 0.4, 0.3, 0.2, and 0.1mm). Both computational and experimental results showed that with the decreased in distance between two pulses (from 0.6 to 0.1mm) or the increase in lateral overlap (0, 17, 33, 50, 67, and 83%), the re-solidification occurred on the previously created crater and pile that in turn causes the increase in surface roughness parameter (Sz) as well as decrease in (Sp/Sv) ratio. It was also evidently found that the variation in crater depth (Sv) is more significant than the pile up height (Sp) for such reduction in the (Sp/Sv) ratio. A close agreement

and a similar trend were observed between the predicted roughness values of computational model with experimental observations. The magnitude of thermal stresses obtained from the computational model was higher than the flexural strength of alumina that indicated that the alumina likely to produced micro-cracks during 2D laser machining. The computational model further shows that the intensity of the thermal stresses is higher at the center of the laser beam which was confirmed with SEM micrographs. The present efforts of the computational model to evaluate the surface roughness for PM moving laser beam (lateral overlap) can be feasible to extend for the three-dimensional laser machining (lateral as well as transverse overlap).

5.4 Three-dimensional (3D) Laser Machining

A computational model was designed and developed to simulate the 3D laser machining conditions and also facilitates to understand the influence of PM moving laser beam (with lateral and transverse overlap of 0, 17, 33, 50, 67, and 83%) on the surface roughness of structural alumina for various laser energy density machining conditions (Dist × O_T = 0.6, 0.5, 0.4, 0.3, 0.2, and 0.1mm). It was observed that the surface roughness initially increased from 113 to 128μm (for 0.6×0.6 to 0.5×0.5mm), then decreased from 128μm to 40μm (for 0.5×0.5 to 0.2×0.2mm), and then rapidly increased to 273μm (for 0.1×0.1mm). The higher material removal rates ($25mm^3$) was found for the 0.1×0.1mm laser machining conditions whereas good surface finish (40μm) was obtained for 0.2×0.2mm laser machining conditions. A close agreement and a similar trend were observed between the predicted roughness values of computational model with experimental observations. The computationally predicted thermal stresses are higher than the flexural limit of structural alumina and indicated the occurrence of thermal cracks inside the machined crater, which was further confirmed by the SEM micrographs. However, since the

material momentarily experiences this higher thermal stresses that can nucleates the thermal cracks but the magnitude of thermal stresses are not sufficient to grow the cracks throughout the alumina samples. The present model can also be utilized to predict the surface topography for any other structural ceramics subjected to various laser processing conditions.

REFERENCES

[1] A.N. Samant, N.B. Dahotre, Laser machining of structural ceramics—A review, Journal of the European Ceramic Society. 29 (2009) 969-993. doi:10.1016/j.jeurceramsoc.2008.11.010.

[2] A.N. Samant, Laser Machining of Structural Ceramics: Computational and Experimental Analysis, PhD Dissertation, University of Tennessee. (2009).

[3] I.P. Tuersley, A. Jawaid, I.R. Pashby, Review: Various methods of machining advanced ceramic materials, J. Mater. Process. Technol. 42 (1994) 377-390. doi:10.1016/0924-0136(94)90144-9.

[4] V.V. Vikulin, I.Y. Kelina, A.S. Shatalin, L.N. Rusanova, Advanced ceramic structural materials, Refractories and Industrial Ceramics. 45 (2004) 383-386. doi:10.1007/s11148-005-0017-2.

[5] N.B. Dahotre, A.N. Samant, Laser Machining of Advanced Materials, CRC Press/Balkema, London, UK; Boca Raton, Fla., 2011.

[6] J.Y. Shen, C.B. Luo, W.M. Zeng, X.P. Xu, Y.S. Gao, Ceramics grinding under the condition of constant pressure, J. Mater. Process. Technol. 129 (2002) 176-181. doi:10.1016/S0924-0136(02)00636-2.

[7] W. König, A. Wagemann, Machining of ceramic components - process-technological potentials, National Institute of Standards and Technology -NIST-: Machining of Advanced Materials. Proceedings: MD-Vol. 45, PED-Vol. 66. (Special Publications - United States Department of Commerce). 45 (1993) 3-16.

[8] G. Chryssolouris, N. Anifantis, S. Karagiannis, Laser assisted machining: An overview, Journal of Manufacturing Science and Engineering, Transactions of the ASME. 119 (1997) 766-769.

[9] E. Kacar, M. Mutlu, E. Akman, A. Demir, L. Candan, T. Canel, V. Gunay, T. Sınmazcelik, Characterization of the drilling alumina ceramic using Nd:YAG pulsed laser, J. Mater. Process. Technol. 209 (2009) 2008-2014. doi:10.1016/j.jmatprotec.2008.04.049.

[10] S.P. Harimkar, N.B. Dahotre, Effect of laser fluence on surface microstructure of alumina ceramic, Advances in Applied Ceramics. 105 (2006) 304-308.

[11] D. Triantafyllidis, L. Li, F.H. Stott, Surface treatment of alumina-based ceramics using combined laser sources, Appl. Surf. Sci. 186 (2002) 140-144. doi:10.1016/S0169-4332(01)00639-0.

[12] B.G. Koepke, R.J. Stokes, A study of grinding damage in magnesium oxide single crystals, Journal of Materials Science. 5 (1970) 240-247. doi:10.1007/BF00551000.

[13] H.P. Kirchner, Damage Penetration at Elongated Machining Grooves in Hot-Pressed Si3N4, J Am Ceram Soc. 67 (1984) 127-132. doi:10.1111/j.1151-2916.1984.tb09629.x.

[14] J.C. Conway, H.P. Kirchner, Crack Branching as a Mechanism of Crushing During Grinding, J Am Ceram Soc. 69 (1986) 603-607. doi:10.1111/j.1151-2916.1986.tb04815.x.

[15] N.B. Dahotre, S.P. Harimkar, Laser Fabrication and Machining of Materials, Springer, New York, N.Y., 2008.

[16] E. Kannatey-Asibu, Principles of Laser Materials Processing, Wiley, Hoboken, N.J., 2009.

[17] G. Chryssolouris, Laser Machining : Theory and Practice, Springer-Verlag, New York, 1991.

[18] H.H. Xu, S. Jahanmir, Microfracture and material removal in scratching of alumina, J. Mater. Sci. 30 (1995) 2235-2247.

[19] B. Zhang, Precision grinding regime of advanced ceramics, Proceedings of the Annual Meeting of the American Society of Precision Engineering. (1993) 225-229.

[20] B. Zhang, T.D. Howes, Material-removal mechanisms in grinding ceramics, CIRP Annals-Manufacturing Technology. 43 (1994) 305-308.

[21] B. Zhang, X. Zheng, H. Tokura, M. Yoshikawa, Grinding induced damage in ceramics, J. Mater. Process. Technol. 132 (2003) 353-364.

[22] K. Salonitis, P. Stavropoulos, A. Stournaras, G. Chryssolouris, CO_2 Laser cutting of aluminium, Proceeding of the 5th Laser Assisted Net Shape Engineering. (2007) 825-835.

[23] P. Stavropoulos, K. Salonitis, A. Stournaras, K. Euthimiou, G. Chryssolouris, Molecular dynamics simulation of laser ablation of iron, Proceedings of the 10th CIRP International Workshop on Modeling of Machining Operations. (2007) 549-553.

[24] A. Stournaras, K. Salonitis, P. Stavropoulos, G. Chryssolouris, Finite element thermal analysis of pulsed laser drilling process, Proceedings of the 10th CIRP International Workshop on Modeling of Machining Operations. (2007) 563-570.

[25] A.K. Dubey, V. Yadava, Laser beam machining—A review, Int. J. Mach. Tools Manuf. 48 (2008) 609-628. doi:10.1016/j.ijmachtools.2007.10.017.

[26] A.N. Samant, N.B. Dahotre, Differences in physical phenomena governing laser machining of structural ceramics, Ceram. Int. 35 (2009) 2093-2097. doi:10.1016/j.ceramint.2008.11.013.

[27] A.N. Samant, B. Du, N.B. Dahotre, In-situ surface absorptivity prediction during 1.06 um wavelength laser low aspect ratio machining of structural ceramics, physica status solidi (a). 206 (2009) 1433-1439. doi:10.1002/pssa.200925108.

[28] A.N. Samant, N.B. Dahotre, Differences in physical phenomena governing laser machining of structural ceramics, Ceram. Int. 35 (2009) 2093-2097. doi:10.1016/j.ceramint.2008.11.013.

[29] A.N. Samant, B. Du, S.R. Paital, S. Kumar, N.B. Dahotre, Pulsed laser surface treatment of magnesium alloy: Correlation between thermal model and experimental observations, J. Mater. Process. Technol. 209 (2009) 5060-5067. doi:10.1016/j.jmatprotec.2009.02.004.

[30] A.N. Samant, N.B. Dahotre, Computational predictions in single-dimensional laser machining of alumina, Int. J. Mach. Tools Manuf. 48 (2008) 1345-1353. doi:10.1016/j.ijmachtools.2008.05.004.

[31] D. Bäuerle, Laser Processing and Chemistry, Springer Berlin, 2000.

[32] S. LEI, Y.C. Shin, F.P. Incropera, Experimental investigation of thermo-mechanical characteristics in laser-assisted machining of silicon nitride ceramics, Journal of manufacturing science and engineering. 123 (2001) 639-646.

[33] J.C. Rozzi, F.E. Pfefferkorn, F.P. Incropera, Y.C. Shin, Transient, three-dimensional heat transfer model for the laser assisted machining of silicon nitride: I. Comparison of predictions with measured surface temperature histories, Int. J. Heat Mass Transfer. 43 (2000) 1409-1424.

[34] J.C. Rozzi, F.P. Incropera, Y.C. Shin, Transient, three-dimensional heat transfer model for the laser assisted machining of silicon nitride: II. Assessment of parametric effects, Int. J. Heat Mass Transfer. 43 (2000) 1425-1437.

[35] J.C. ROZZI, F.E. Pfefferkorn, F.P. Incropera, Y.C. Shin, Transient thermal response of a rotating cylindrical silicon nitride workpiece subjected to a translating laser heat source, Part I: Comparison of surface temperature measurements with theoretical results, Journal of heat transfer. 120 (1998) 899-906.

[36] J.C. ROZZI, F.E. Pfefferkorn, F.P. Incropera, Y.C. Shin, Transient Thermal Response of a Rotating Cylindrical Silicon Nitride Workpiece Subjected to a Translating Laser Heat Source, Part II: Parametric Effects and Assessment of a Simplified Model, J. Heat Transfer. 120 (1998) 907-915.

[37] S. Lei, Y.C. Shin, F.P. Incropera, Deformation mechanisms and constitutive modeling for silicon nitride undergoing laser-assisted machining, Int. J. Mach. Tools Manuf. 40 (2000) 2213-2233.

[38] C.Y. Yeo, S.C. Tam, S. Jana, M.W.S. Lau, A technical review of the laser drilling of aerospace materials, J. Mater. Process. Technol. 42 (1994) 15-49. doi:10.1016/0924-0136(94)90073-6.

[39] A. Corcoran, L. Sexton, B. Seaman, P. Ryan, G. Byrne, The laser drilling of multi-layer aerospace material systems, J. Mater. Process. Technol. 123 (2002) 100-106. doi:10.1016/S0924-0136(01)01123-2.

[40] L. Li, C. Diver, J. Atkinson, R. Giedl-Wagner, H.J. Helml, Sequential Laser and EDM Micro-drilling for Next Generation Fuel Injection Nozzle Manufacture, CIRP Ann. Manuf. Technol. 55 (2006) 179-182. doi:10.1016/S0007-8506(07)60393-X.

[41] J. Lawrence, D.K.Y. Low, J. Pou, E. Toyserkani, Advances in Laser Materials Processing Technology, Woodhead Publishing Ltd, Cambridge, 2010.

[42] M.M. Hanon, E. Akman, B. Genc Oztoprak, M. Gunes, Z.A. Taha, K.I. Hajim, E. Kacar, O. Gundogdu, A. Demir, Experimental and theoretical investigation of the drilling of alumina ceramic using Nd:YAG pulsed laser, Optics & Laser Technology. 44 (2012) 913-922. doi:10.1016/j.optlastec.2011.11.010.

[43] S.P. Harimkar, A.N. Samant, N.B. Dahotre, Temporally evolved recoil pressure driven melt infiltration during laser surface modifications of porous alumina ceramic, Journal of Applied Physics. 101 (2007) 054911-054911-7.

[44] S. Sun, Y. Durandet, M. Brandt, Parametric investigation of pulsed Nd: YAG laser cladding of stellite 6 on stainless steel, Surface and Coatings Technology. 194 (2005) 225-231. doi:10.1016/j.surfcoat.2004.03.058.

[45] M.U. Islama, G. Campbella, Laser machining of ceramics: a review, - Materials and Manufacturing Processes. 8 (1993) 611-630. doi:10.1080/10426919308934870.

[46] S.I. Anisimov, Vaporization of Metal Absorbing Laser Radiation, Soviet Physics, Journal of Experimental and Theoretical Physics. 27 (1968) 182.

[47] V. Semak, A. Matsunawa, The role of recoil pressure in energy balance during laser materials processing, Journal of Physics D: Applied Physics. 30 (1997) 2541-2552.

[48] F. Quintero, F. Varas, J. Pou, F. Lusquiños, M. Boutinguiza, R. Soto, M. Pérez-Amor, Theoretical analysis of material removal mechanisms in pulsed laser fusion cutting of ceramics, Journal of Physics D: Applied Physics. 38 (2005) 655-666.

[49] W.H. Gitzen, Alumina as a Ceramic Material. American Ceramic Society, Columbus, Ohio, 1970.

[50] P. Paradis, T. Ishikawa, Surface tension and viscosity measurement of liquid and undercooled alumina by contactless techniques, Japanese Journal of Applied Physics. 44 (2005) 5082-5085.

[51] COMSOL, Users guide, COMSOL Multiphysics model library. V 4.2a (2011).

[52] COMSOL, Continuous casting model, COMSOL Multiphysics model library. V 4.2a (2011).

[53] M. Sussman, P. Smereka, S. Osher, A Level Set Approach for Computing Solutions to Incompressible Two-Phase Flow, Journal of Computational Physics. 114 (1994) 146-159. doi:10.1006/jcph.1994.1155.

[54] COMSOL, Marangoni convection model, COMSOL Multiphysics model library. V 4.2a (2011).

[55] N. Pierron, P. Sallamand, S. Matteï, Numerical Modeling of Molten Pool Formation During an Interaction of a Pulse Laser (ND:YAG) with an Aluminum Sheet, (2005) 1-5. doi:http://www.comsol.com/papers/1124/.

[56] N.I. Kolev, Multiphase Flow Dynamics 5. Nuclear Thermal Hydraulics, Springer, Berlin; Heidelberg; New York; Barcelona; Hong Kong; London; Milan; Paris; Tokyo, 2011.

[57] T. Gross, S. Hening, D. Watt, Crack formation during laser cutting of silicon, J. Appl. Phys. 69 (1991) 983-989.

[58] N. Sumi, R.B. Hetnarski, N. Noda, Transient thermal stresses due to a local source of heat moving over the surface of an infinite elastic slab, Journal of Thermal Stresses. 10 (1987) 83-96.

[59] B. Yilbas, C. Karatas, A. Arif, B. Abdul Aleem, Laser control melting of alumina surfaces and thermal stress analysis, Optics & Laser Technology. 43 (2011) 858-865.

[60] B.S. Yilbas, S. Akhtar, C. Karatas, Laser straight cutting of alumina tiles: thermal stress analysis, The International Journal of Advanced Manufacturing Technology. 58 (2012) 1019-1030.

[61] http://www.advaluetech.com/alumina99_technical_info.html, 2013 (2013).